Technical University Munich
Department of Physics

**Abschlussarbeit im Masterstudiengang**
**Kern-, Teilchen- und Astrophysik**

# Measurement of the 1-jettiness Event Shape Observable in Deep-inelastic Electron-Proton Scattering

Johannes Hessler

November 25, 2021

Erstgutachter (Themensteller): PD Dr. S. Kluth

**Abstract**

The 1-jettiness event shape observable $\tau_1^b$ is measured for the first time in neutral-current deep-inelastic scattering (DIS) [1]. For the measurement, the equivalence of $\tau_1^b$ to the DIS thrust $\tau_Q$ in the Breit frame is utilised. The data were taken at the HERA $ep$ collider with the H1 experiment in the years 2003 to 2007. The centre of mass energy amounts to 319 GeV and only events with high virtuality $Q^2 > 150$ GeV$^2$ are analysed. The data are easily accessible thanks to the efforts of the Data Preservation in High Energy Physics (DPHEP) project. A feasibility study for the measurement of the 1-jettiness is performed and different methods for the reconstruction of the event kinematics are compared. Corrections for detector effects and electron QED radiation are derived and applied to the data. In the next step, the systematical uncertainties are evaluated. They are small over the entire kinematic range. The analysis framework is then benchmarked against previous H1 event shape measurements. Finally, the 1-jettiness cross sections are presented as a function of $\tau_1^b$ for the kinematic range in the inelasticity $0.2 < y < 0.7$ and the virtuality $150 < Q^2 < 20\,000\,\text{GeV}^2$, as well as for adjacent regions in $y$ and $Q^2$. The data are compared to selected predictions including the recent Monte Carlo models Pythia 8.3 and Herwig 7.2, as well as fixed order calculations obtained from NNLOJET. None of the predictions provide a fully satisfactory description of the data over the entire phase space.

**Kurzfassung**

In dieser Masterarbeit wird die erste Messung der 1-jettiness Event Shape Observable $\tau_1^b$ in neutraler tiefen-inelastischer Streuung präsentiert. Für die Messung wird die Übereinstimmung der 1-jettiness mit dem DIS Thrust im Breit-Referenzsystem ausgenutzt. Die Daten wurden in den Jahren 2003 bis 2007 mit dem H1 Experiment am HERA Beschleuniger genommen. Für die Analyse werden nur Events mit hoher Virtualität $Q^2 > 150$ GeV$^2$ verwendet. Die Schwerpunktsenergie beträgt $\sqrt{s} = 319$ GeV. Die analysierten Daten sind dank des Projekts zur Erhaltung von Daten in der Hochenergiephysik leicht zugänglich. Eine Machbarkeitsstudie zur Messung der 1-jettiness wird durchgeführt. Dabei wird gezeigt, dass die 1-jettiness in einem großen Phasenraum in der Inelastizität $y$ und der Virtualität $Q^2$ gemessen werden kann. Im Anschluss werden verschiedene Methoden zur Rekonstruktion einzelner Events verglichen. Die Daten werden für Detektor- und QED-Effekte korrigiert und die systematischen Unsicherheiten werden ausgewertet. Diese sind im gesamten Phasenraum klein. Um die einzelnen Arbeitsschritte der Analyse zu validieren, werden Event Shape Messungen, die zuvor von der H1 Kollaboration durchgeführt wurden, reproduziert. Schließlich werden die Wirkungsquerschnitte als Funktion von $\tau_1^b$ sowohl für $0.2 < y < 0.7$ und $150 < Q^2 < 20\,000\,\text{GeV}^2$, als auch in einzelnen $y$ und $Q^2$ Bereichen präsentiert. Die Daten werden mit den modernen Monte-Carlo-Modellen Pythia 8.3 und Herwig 7.2 verglichen, sowie mit NNLO Vorhersagen von NNLOJET. Keine der Vorhersagen beschreibt die Daten im gesamten Phasenraum zur vollen Zufriedenheit.

# Contents

# Chapter 1

# Introduction

The HERA collider was the only high energy electron proton collider that has been constructed so far. The high center of mass energy of $\sqrt{s} = 319$ GeV enables an extension of the phase space to regions that were not accessible with previous fixed target deep-inelastic scattering (DIS) experiments. The produced data set is unique. The collision of point-like leptons with the constituents of the proton provides excellent conditions to study the structure of the proton. Other areas of high energy physics, such as jet or heavy quark production can also be examined with the HERA data set. Of particular interest is the strong coupling constant $\alpha_s$, being the only free parameter of Quantum Chromodynamics (QCD). A set of observables was constructed to be sensitive to $\alpha_s$, the so-called event shape observables. An event shape observable classifies one event (denoting one $ep$ collision) according to the topology of its hadronic final state.
The planned EIC (Electron Ion Collider) [2] in the US and the two proposed colliders LHeC (Large Hadron electron Collider) [3, 4] at CERN and EicC (Electron-ion collider in China) [5] lead to an increasing interest in the HERA data in the last years. In addition there has been progress on the theoretical frontier. Advanced theoretical concepts and increasing computing power motivate a revisit of event shape obervables. Due to the successful data preservation project in high energy physics (DPHEP), the H1 data are easily accessible.
Of particular interest for this analysis is the 1-jettiness observable. An expression for the 1-jettiness can be derived in the Breit frame which coincides with the DIS thrust. One can make use of this equivalence to measure the 1-jettiness for the first time ever.
The theoretical framework is presented in chapter 2 with a focus on neutral-current deep-inelastic scattering and event shape observables. Chapter 3 gives an overview over the experimental setup, including the HERA accelerator, the H1 experiment and the utilised Monte Carlo Models for event simulation. The preservation of the H1 data and analysis framework is discussed before introducing different methods for the reconstruction of the event kinematics. The feasability of a 1-jettiness measurement at H1 is investigated in chapter 4. The cross section and the necessary corrections to obtain the cross sections from the data are defined in chapter 5. In chapter 6, the analysis framework is benchmarked by reproducing a previous H1 event shape measurement. The results of the single and triple differential cross section measurement are finally presented in chapter 7.

# Chapter 2

# Theoretical framework

This chapter gives a brief introduction on Quantum Chromodynamics and the neutral current deep inelastic scattering process followed by a section on event shape observables.

## 2.1 Quantum Chromodynamics

Quantum Chromodynamics (QCD) is the theory of the strong interaction. The charge of the strong interaction is the so-called colour charge. The colour charge can take three "values", red, green and blue. It was introduced after the discovery of the $\Delta^{++}$ baryon. The baryon consists of three up quarks and has the spin 3/2. As a fermion (particle with half-integer spin), the $\Delta^{++}$ has to fulfill the Pauli principle which dictates a completely anti-symmetric wave function. This condition can only be fulfilled, when an additional degree of freedom is introduced, the colour charge.
This section presents a short introduction to QCD [6–9]. A more detailed and thorough approach can be found e.g. in [10, 11].
QCD is a quantum field theory, described by the $\mathrm{SU}(3)_c$ gauge group, where the index $c$ stands for colour. The eight generators of the symmetry can be expressed as the Gell-Mann matrices. They obey the non-trivial commutation relations [11]

$$[\lambda_i \ , \ \lambda_j] = i f^{ijk} \lambda_k \tag{2.1}$$

where the completely anti-symmetric structure functions $f^{ijk}$ were introduced. They are the main difference to the well established Quantum Electrodynamics (QED). The commutation relations give rise to self-interactions between the quanta of the gauge field, the gluons.
A key feature of any quantum field theory is renormalisability [12]. It takes care of the so-called ultra violet (UV) divergences. The divergences result from loop integrals correcting for higher order effects. The momenta in those integrals can get arbitrarily large. By introducing a renormalisation scale $\mu_R$ this problem can be solved. Any measurable physical quantity $\Gamma$ has to be independent of the scale. This requirement is expressed in the Renormalisation Group Equation

$$\left( \mu_R^2 \frac{\partial}{\partial \mu_R^2} + \mu_R^2 \frac{\partial \alpha_\mathrm{s}}{\partial \mu_R^2} \frac{\partial}{\partial \alpha_\mathrm{s}} \right) \Gamma = 0 \tag{2.2}$$

where the $\beta$ function can be introduced

$$\beta(\alpha_s) = \mu_R^2 \frac{\partial \alpha_s(\mu_R^2)}{\partial \mu_R^2} = -\alpha_s \sum_i \beta_n \left(\frac{\alpha_s}{4\pi}\right)^{(i+1)}. \tag{2.3}$$

The first two coefficients of the expansion in $\alpha_s$, $\beta_0$ [6,7] and $\beta_1$ [13], are given by

$$\beta_0 = 11 - \frac{2}{3}n_f \quad \text{and} \quad \beta_1 = 102 - \frac{38}{3}n_f,$$

where $n_f$ denotes the number of quark flavours. For $n_f = 6$, $\beta_0$ is positive. In most cases, only $n_f = 5$ is considered, due to the high mass of the top quark. This result is different to QED, where $\beta_0^{QED}$ is negative [10]. The positive sign in $\beta_0$ stemming from the gluon self interactions implies a property known as asymptotic freedom [6,7]. In contrast to QED, where those self interaction terms are absent, the interaction strength decreases with increasing scale or decreasing distance. As a direct consequence, partons can be treated as quasi-free particles at high scales. Another important property of QCD is the so-called confinement [14,15]. It states that objects with free colour charge can not be observed.
The $\beta$ function implies an energy dependence of $\alpha_s$. The exact analytical solution to equation (2.3) is so far only known to $\beta_0$ order. It yields [16]

$$\alpha_s(Q^2) = \frac{4\pi}{\beta_0 \ln(Q^2/\Lambda^2)} \tag{2.4}$$

where the QCD scale parameter $\Lambda$ was introduced. The energy dependence or "running" of $\alpha_s$ is of particular interest to particle physicists. It has to be extracted from experiments. Compared to other coupling constants, $\alpha_s$ possesses the largest associated uncertainty. The running of $\alpha_s$ is shown in figure 2.1.

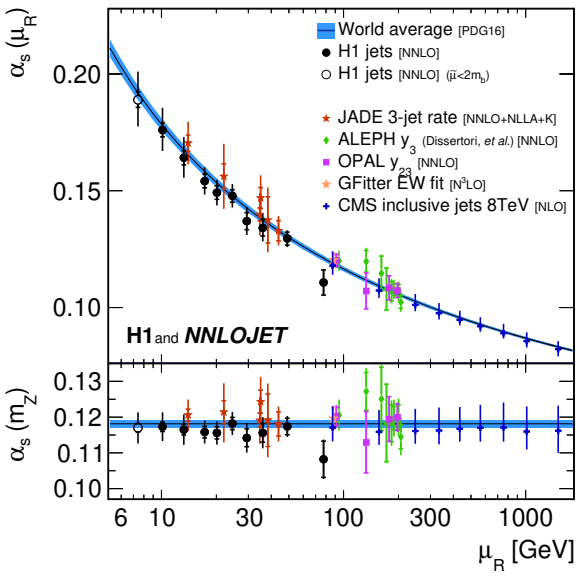


Figure 2.1: Results for $\alpha_s(m_Z)$ and $\alpha_s$ $(\mu_R)$ for fits to data points arranged in groups of similar $\mu_R$. The results of different experiments are compared. Figure taken from [17].

## 2.2 Neutral-current deep-inelastic scattering

Neutral-current deep-inelastic scattering (NC DIS) describes the scattering process of an electron with a proton at very high energies. The electron can penetrate the proton and scatters on a parton, a constituent of the proton. For this analysis only neutral-current scattering is considered. The interaction is mediated by a photon $\gamma$, by a neutral $Z$-boson or their interference. In all cases, the electron is scattered and can be reconstructed in the detector. In this section the kinematics of the scattering process are explained..

### 2.2.1 Kinematics

A Feynman diagram of the leading-order NC DIS process is depicted in figure 2.2. One parton from the proton with four-momentum $p$ collides with an electron with four-momentum $k$. The parton carries the fraction $x$ of the total proton four-momentum $P$. The right diagram depicts the scattering process in the Breit frame, see sec. 2.2.4.

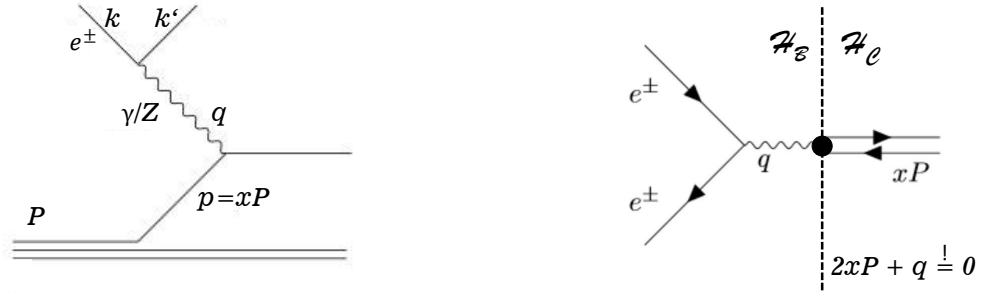


Figure 2.2: Feynman diagram of $e^{\pm}p$ neutral-current deep-inelastic scattering (NC DIS). The right diagram shows the process in the Breit frame including the condition for the boost vector. Space is separated into the beam hemisphere $\mathcal{H}_{\mathcal{B}}$ and the current hemisphere $\mathcal{H}_{\mathcal{C}}$.

In the laboratory frame, the electron collides head-on with one parton. The scatted electron has momentum $k'$. The hadronic final state (HFS) $X$ includes all final state particles apart from the scattered electron. Its four-vector is denoted with $p_X$. The four-vector of the exchanged virtual boson $q$ can be calculated from the initial and final state electron four-momenta [18]

$$q = k - k'. \tag{2.5}$$

Since the boson is space-like, one defines the (positive definite) virtuality of the exchanged boson

$$Q^2 = -q^2. \tag{2.6}$$

The virtuality corresponds to the transfer of momentum from the electron to the parton. The dimensionless, Lorentz-invariant inelasticity

$$y = \frac{P \cdot q}{P \cdot k} \tag{2.7}$$

measures the energy loss of the electron in the target rest frame. The inelasticity is in the range

$0 < y < 1$. The Bjorken scaling variable $x$ is defined by $Q^2$, $y$ and the centre of mass energy $\sqrt{s}$

$$x = \frac{Q^2}{ys}\,, \tag{2.8}$$

where $s$ is given by

$$s = (k + P)^2 \approx 4E_e E_P. \tag{2.9}$$

In the last term the electron and proton masses were neglected. $x$ is Lorentz-invariant and ranges from 0 to 1. The three observables $x$, $y$ and $Q^2$ define the kinematics of the scattering process. Another useful quantity is the pseudorapidity $\eta$ which is defined as

$$\eta = -\ln\tan(\vartheta/2). \tag{2.10}$$

The polar angle $\vartheta$ is defined with respect to the $z$-axis, which is usually chosen along the proton direction in DIS.

### 2.2.2 The inclusive neutral current DIS cross section

The inclusive NC DIS cross section for unpolarised electron proton scattering as a function of $x$ and $Q^2$ is given by [18]

$$\frac{d^2\sigma}{dxdQ^2} = \frac{2\pi\alpha_{\text{em}}}{xQ^4}\left[Y_+F_2(x,Q^2) - y^2F_L(x,Q^2) \mp Y_-xF_3(x,Q^2)\right] \tag{2.11}$$

with $Y_\pm = 1 \pm (1-y^2)$ and the structure functions $F_L, F_2$ and $F_3$. The longitudinal structure function $F_L$ is related to $F_1$ and $F_2$ via $F_L = F_2 - 2xF_1$. The structure functions have to be measured experimentally. The structure functions were introduced by Feynman in the Naive Quark Parton Model (QPM) in an attempt to explain the scaling behaviour of $F_L$ . The scaling behaviour was predicted by Bjorken [19] and later confirmed by experiments at the Stanford Linear Accelerator Center [20]. It describes the $x$ dependency of $F_L$ at high $Q^2$. Feynman proposed partons as a solution to the observation. They pose as point-like constituents of the proton. They were later identified with the quarks. $F_2$ can be expressed in terms of the distribution functions of the partons (PDFs) $f_i(x)$

$$F_2(x,Q^2) = \sum_i e_i^2 x f_i(x). \tag{2.12}$$

The sum runs over all quarks and antiquarks with flavour $i$ and charge $e_i$. $xf_i(x)$ gives the probabilty to find a parton $i$ with momentum fraction $x$ in the proton. The Callan-Gross relation $F_2 = 2xF_1$ follows directly from the QPM, since it predicts $F_L = 0$. An improved parton model taking higer order corrections into account is described by the DGLAP formalism [21–23].
The factorisation theorem states that the cross section can be written as a convolution of the hard partonic cross section $\hat{\sigma}_i$ with the parton distribution functions $f_i$ of parton $i$ in the proton [24]

$$\sigma(x,Q^2) = \sum_{i=q,\bar{q},g}\int_x^1 \frac{d\zeta}{\zeta} f_i(\zeta,\mu_F^2,\alpha_{\text{s}}(\mu_R))\hat{\sigma}_i\left(\frac{x}{\zeta},\mu_R^2,\mu_F^2,\alpha_{\text{s}}(\mu_R)\right). \tag{2.13}$$

The sum runs over all partons in the proton. The renormalisation scale $\mu_R$ was introduced, which can be interpreted as a cut-off of UV divergences. In DIS one usually identifies $\mu_R$ with

$Q$. In leading order, the $f_i$ are independent of $\alpha_s$ and $\mu_R$. They give the probability to find a parton $i$ with momentum fraction betwenn $\zeta$ and $\zeta + d\zeta$ in the proton. The PDF absorbs the long-range behaviour of QCD and thus $\hat{\sigma}_i$ can be calculated in perturbative QCD. The factorisation property of QCD can be proven to all orders in perturbation theory [24].
The $\mu_F$-dependence of the PDFs is described by the DGLAP evolution equations. It can be expressed as a convolution of the PDFs with the spitting functions $\mathcal{P}_{ij}(x/\zeta, \alpha_s(\mu_F))$. The splitting functions $\mathcal{P}_{ab}$ are related to the parton splitting process $a \to bc$, where the type of the third parton $c$ is fixed by $a$ and $b$. At leading order the dependence of the PDF on $\mu_F$ reads [10]

$$\frac{\partial}{\partial \log Q^2} \begin{pmatrix} f_q(x,Q^2) \\ f_g(x,Q^2) \end{pmatrix} = \frac{\alpha_s(Q^2)}{2\pi} \int_x^1 \frac{d\zeta}{\zeta} \begin{pmatrix} \mathcal{P}_{qq}(\frac{x}{\zeta}) & \mathcal{P}_{qg}(\frac{x}{\zeta}) \\ \mathcal{P}_{gq}(\frac{x}{\zeta}) & \mathcal{P}_{gg}(\frac{x}{\zeta}) \end{pmatrix} \begin{pmatrix} f_q(\zeta,Q^2) \\ f_g(\zeta,Q^2) \end{pmatrix} \tag{2.14}$$

where the factorisation scale was identified with $\mu_F = Q$. $f_q$ is a $2n_f$-dimensional vector of the quark and anti-quark densities. The sum over all $2n_f$ flavours and anti-flavours is implicit.

### 2.2.3 Parton showers and hadronisation

The transition from the scattering process calculable in perturbation theory according to the Feynman rules to physical (colour-less) particles is usually done in two steps. The (perturbative) parton shower simulates a cascade of coloured partons. The parton shower prescription can be directly attached to the LO matrix elements. Each parton undergoes a subsequent emission of additional partons, starting from the partons of the hard scattering process. The showering process is stopped when the evolution variable reaches some hadonisation scale $Q_0$.
An alternative approach to this DGLAP type parton shower is the colour dipole model [25]. One or two colour partners are assigned to each (anti-) quark or gluon, respectively. The colour partners then form a dipole. Every gluon radiation forms a new dipole. The splitting cascade terminates, when some stopping criterion is reached, e.g. a minimum transverse momentum.
After the parton shower, observable hadrons are formed from the coloured mutli-parton final state. This step is required due to the confinement property of QCD. It is called hadronisation. The characteristic scale of hadronisation is of the order of the hadron masses. It is usually set to $Q_0 = 1$ GeV in event generators. The scale determines when the parton cascade is stopped and the hadronisation model is applied.
The Lund string fragmentation model [26] assumes a string between two coloured objects. The potential is increasing linearly with the distance. This approach is based on observations from lattice QCD. A new quark - antiquark pair is produced with a certain probability when the potential energy gets similar to the hadron masses. The remaining quarks and antiquarks are combined into hadrons when the available energy is used up.
The cluster hadronisation [27] is based on the so-called preconfinement property of QCD [28]. It states that partons in a shower are custered in colour-less groups when the evolution scale is much smaller than the hard scale. They can be identified as proto-hadrons decaying into the observed final state hadrons.
Monte Carlo (MC) event generators make use of the parton shower and hadronisation models for a detailed simulation of scattering processes (cf. section 2.4).

### 2.2.4 The Breit frame

Since $x$, $y$ and $Q^2$ are defined as products of four-vectors, all three quantities are Lorentz-invariant. Therefore, a Lorentz transformation to a different reference frame is straight-forward.

The Breit frame separates space into two hemispheres with positive or negative rapidity. The scattering process in the Breit frame is illustrated on the right in figure 2.2. Every reference frame is defined by a boost vector which has to vanish in the dedicated reference frame. In the Breit frame the boost vector is given by

$$2xP + q = 0. \tag{2.15}$$

The boson is completely space-like and collides head on with the incoming parton. The $z$-axis in the Breit frame coincides with the proton-boson axis. In the QPM, the parton has momentum $Q/2$ before and after the collision. The parton is reflected back parallel to the incoming direction. This gives the Breit frame the "nickname" brick wall frame. The space is evenly divided into two hemispheres separated by the $\eta = 0$ plane. The beam hemisphere ($\eta > 0$) holds the final state lepton and the beam remnant, while the struck parton is scattered into the current hemisphere ($\eta < 0$) . However, higher order processes can distort this picture. It is then possible to obtain a current hemisphere which is empty, apart from arbitrarily soft emissions. This feature of DIS was already predicted more than 40 years ago [29].

## 2.3 Event shape observables

Event shape observables were introduced to study the shape of the hadronic final state (HFS) in the detector. An event shape observable classifies the events according to their particle topology. The observables are sensitive to the strong coupling constant $\alpha_s$ and to PDFs. In the case of Quark-Parton-Model-like events the configurations of the HFS is 'pencil-like' and the event shape observables tend to zero. Higher order hard QCD effects, or soft QCD effects like hadronisation give rise to non-trivial event shape distributions. Large values for the observable indicate the presence of hard QCD radiations. These can result in multiple jets in the detector.

### 2.3.1 Event shape observables in electron-positron scattering

Electron positron annihilation provides a clean environment for the study of the HFS and therefore for event shape observables [30]. A review on event shape observables in $e^x e^-$ is given in [31]. There is no interference between the initial state particles and the final state particles. One popular example for an event shape observable is the so-called thrust $\tau$. In electron positron scattering, $\tau$ is defined as

$$\tau = 1 - T = 1 - \max_{\vec{n}} \frac{\sum_i |\vec{p}_i \cdot \vec{n}|}{\sum_i |\vec{p}_i|} \tag{2.16}$$

where $\vec{p}_i$ is the 3-momentum of final state particle $i$ in an event. The thrust axis $\vec{n}$ is found in a way, such that is minimises $\tau$. In the simplest case, the HFS consists of two back-to-back jets. Most particles are parallel to $\vec{n}$. This results in a small value for $\tau$. An additional hard radiation leads to a three jet configuration. The value for $\tau$ would increase for this event topology. For a perfectly spherical event one would obtain $\tau = 1/2$. From the value of $\tau$, it is possible to classify the distribution of final state particles in the detector.

### 2.3.2 Event shape observables in electron-proton scattering

DIS is the t-channel analogous to the s-channel process $e^+e^- \to q\bar{q}$. The event shape observables defined for $e^+e^-$ scattering can be transferred to DIS. Several measurements of event shape

observables have been conducted at H1 [32–34] and ZEUS [35,36]. The definition of the thrust in $e^+e^-$ collisions has an equivalent in DIS scattering denoted with $\tau_c$ in [34]. It calculates the thrust with respect to the direction $\vec{n}$. The axis maximises the sum of the longitudinal momenta. The observable is defined in the Breit frame which was introduced in section 2.2.4. The sum extends over all particles in the current hemisphere ($\eta^{Breit} < 0$), while particles in the beam hemisphere ($\eta^{Breit} > 0$) do not contribute

$$\tau_c = 1 - T = 1 - \max_{\vec{n}} \frac{\sum_{h\in\mathcal{H}_c} |\vec{p}_h \cdot \vec{n}|}{\sum_{h\in\mathcal{H}_c} |\vec{p}_h|}. \tag{2.17}$$

However, the Breit frame in DIS already provides a self-evident choice for the direction $\vec{n}$: the boson axis. Since the boson axis coincides with the $z$-axis, this choice for $\vec{n}$ corresponds to the projection of the particle momenta in the current hemisphere onto the $z$-axis. The alternative definition of the thrust is therefore given by

$$\tau_z = 1 - \frac{\sum_{h\in\mathcal{H}_c} |p_{z,h}|}{\sum_{h\in\mathcal{H}_c} |\vec{p}_h|}. \tag{2.18}$$

Further event shape observables are the jet broadening $B$, the squared jet mass $\rho$ and the $C$-parameter. The squared jet mass is independent of hadron masses and is normalised to four times the squared sum of scalar momenta in the current hemisphere

$$\rho = \frac{(\sum_{h\in\mathcal{H}_c} |p_h|)^2 - (\sum_{h\in\mathcal{H}_c} \vec{p_h})^2}{(2\sum_{h\in\mathcal{H}_c} |\vec{p}_h|)^2}. \tag{2.19}$$

The jet broadening is defined as

$$B = \frac{\sum_{h\in\mathcal{H}_c} |p_{t,h}|}{2\sum_{h\in\mathcal{H}_c} |\vec{p}_h|}. \tag{2.20}$$

It measures the scalar sum of transverse momenta with respect to the virtual boson axis in the current hemisphere. The $C$-parameter is defined as

$$C = \frac{1}{2} \cdot \frac{3\sum_{h,h'\in\mathcal{H}_c} |\vec{p_h}||\vec{p_{h'}}| \sin^2\vartheta_{hh'}}{(\sum_{h\in\mathcal{H}_c} |\vec{p}_h|)^2} \tag{2.21}$$

where $\vartheta_{hh'}$ is the angle between particle $h$ and $h'$. The factor $1/2$ takes care of double counting of the particles.
Only particles in the current hemisphere contribute to the observables defined in eq. (2.17)-(2.21). They are defined to be independent of the particle masses. This means that they are normalised to the modulus of momenta, rather than energies. As mentioned in section 2.2.4, it is possible to obtain event configurations in DIS with empty current hemisphere. To ensure infrared and collinear safety of the observables, a cut on the energy in the current hemisphere $E_c$ had to be introduced in previous measurements [32–36]

$$E_c = \sum_h E_h > \epsilon_{\text{lim}} = Q/10. \tag{2.22}$$

The exact value of the minimal energy $\epsilon_{\text{lim}}$ is not of importance [33].

### 2.3.3 The 1-jettiness

A more modern event shape observable is the 1-jettiness. It is defined as a part of a set of 1-jettiness observables [37] as

$$\tau_1^b = \frac{2}{Q^2} \cdot \sum_{i \in X} \min\{q_B \cdot p_i, q_J \cdot p_i\}, \tag{2.23}$$

where $p_i$ is the 4-momentum of particle $i$ and $q_B$ is the 4-momentum of the incoming parton

$$q_B = xP. \tag{2.24}$$

The sum runs over the entire HFS $X$. It is normalised to the virtuality of the boson $Q^2$. The 1-jettiness observables differ in the choice for the axis $q_J$. For the definition of $\tau_1^b$ the axis $q_J$ is chosen to coincide with the outgoing parton:

$$q_J = q + xP. \tag{2.25}$$

The 1-jettiness is Lorentz-invariant. Even though the observable is called 1-jettiness, there is in fact no jet finding algorithm involved. Recalling the properties of the Breit frame, one realizes that the axes $q_B$ and $q_J$ are back-to-back in the Breit frame. This can be used to derive an alternative expression for the 1-jettiness [38, 39]

$$\tau_1^b = 1 - \frac{2}{Q} \cdot \sum_{i \in \mathcal{H}_C} p_{i,z} \equiv \tau_Q. \tag{2.26}$$

The sum in equation (2.26) runs over the current hemisphere only. The beam hemisphere, holding the beam remnant, can be neglected.
From a theoretical point of view, the DIS thrust and the 1-jettiness are equivalent. However, from the experimental point of view, the DIS thrust is preferred, since only particles in the current hemisphere contribute to the sum.
In previous event shape analyses [32–36], the observables were normalised to the total momentum in the current hemisphere $\sum_i |\vec{p}_i|$. Due to higher order processes with empty current hemispheres, a cut on the total energy in the current hemisphere had to be introduced (cf. eq. (2.22)). This cut can be prevented when normalising to $Q/2$. As a consequence, a sharp $\delta$-peak is expected at $\tau_1^b = 1$. It can be understood as events with zero particles in the current hemisphere.
The kinematic constraints on the beam remnant and the jet originating from the scattered parton imply an upper limit for $\tau_1^b$ [39]

$$\tau_1^{\mathrm{b,max}} = \begin{cases} 1 & x \leq 1/2, \\ \frac{1-x}{x} & x > 1/2. \end{cases} \tag{2.27}$$

When calculating the cumulative structure functions $F_1$ and $F_L$ as a function of $\tau_1^b$, a discontinuity at $\tau_1^{\mathrm{b,max}}$ is observed. The jump is smaller than 1% for $F_1$ and can be up to several percent for $F_L$. It is reduced with increasing $x$ [37].
The 1-jettiness can be theoretically predicted with high precision. The predictions include fixed order corrections and a summation of large logarithms up to NNLL accuracy in resummed perturbation theory. The authors make use of Soft Collinear Effective Theory (SCET) to derive

factorisation theorems for the 1-jettines $\tau_1^b$ [37]. Analytical $\mathcal{O}(\alpha_s)$ predictions [39] are available, as well as NNLL+NLO ($\mathcal{O}(\alpha_s)$) predictions [40].

Theoretical predictions up to N$^3$LL precision can be calculated [41]. In figure 2.3 the conver-

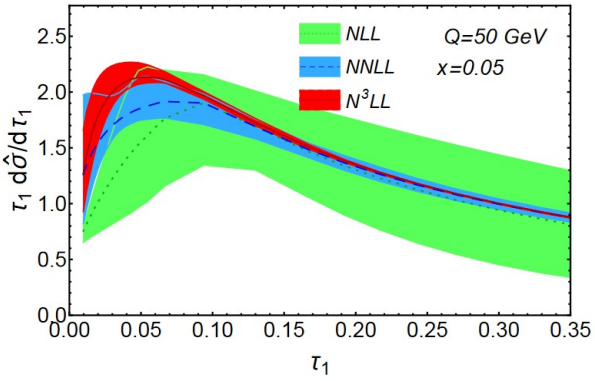


Figure 2.3: Theoretical prediction of the $\tau_1^b$ cross section, comparing calculations with NLL, NNLL and N$^3$LL precision. The convergence of the calculation can be observed as well as the decrease in the perturbative resummation uncertainty when going from NLL to N$^3$LL order. Figure taken from [41]

gence of the DIS cross section when going from NLL to NNLL and N$^3$LL can be observed. The theoretical uncertainties are reduced significantly. The cross sections are shown for representative values for $x$ and $Q^2$.

To probe the sensitivity of the observable on the strong interaction constant $\alpha_s$ a Monte

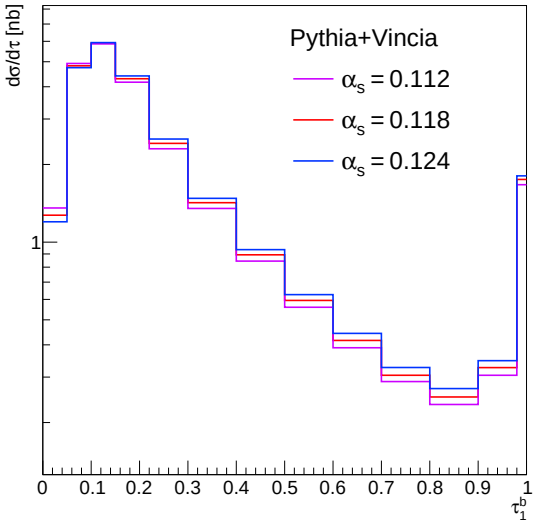


Figure 2.4: Monte Carlo study to probe the sensitivity of the 1-jettiness $\tau_1^b$ to the strong coupling constant $\alpha_s$. The value of $\alpha_s$ was fixed to three different values. More information on the Pythia MC generator and the Dire parton shower is given in section 2.4.

Carlo study is performed. The MC event generator Pythia 8.303 [42,43] is used in combination with the Vincia parton shower model [44–47]. Figure 2.4 shows the simulated differential cross section $d\sigma/d\tau_1^b$ after parton shower and hadronisation in the phase space $0.2 < y < 0.7$ and $150 < Q^2 < 20\,000\,\text{GeV}^2$. The value of $\alpha_s$ was varied by 5% for the three curves. For small

$\tau_1^b < 0.3$ no dependence on $\alpha_s$ can be observed. For larger $\tau_1^b > 0.3$ the cross section exhibits a sensitivity to $\alpha_s$.
In conclusion, the 1-jettiness is a well defined event shape observable that displays an interesting sensitvity to $\alpha_s$. Utilising the equivalence of $\tau_1^b$ and $\tau_Q$, the 1-jettiness $\tau_1^b$ can be measured as $\tau_Q$.

## 2.4 Theoretical predictions

Various MC predictions will be compared to the measured cross sections. They are briefly introduced in this section.
The DIS MC event generator Djangoh 1.4 [48] and Rapgap 3.1 [49] are also used as signal event generators, more information on them is given in section 3.3. Both models make use of the Lund string fragmentation model with the ALEPH tune [50] and the CTEQ6L PDF [51].
The MC event generator Pythia 8.303 [42, 43] is used with three different models for the parton shower. The first model is the 'default' dipole-like $p_\perp$-ordered shower. The other two models are the the $p_\perp$-ordered Vincia parton shower [44–47] at leading colour, and the Dire [52–54] parton shower. The latter is an improved dipole-shower with additional handling of collinear enhancements. For all three setings, the NNPDF3.1 PDF set [55] is used. The value of the strong coupling constant $\alpha_s$ is set consistently to 0.118.
The multi-purpose particle physics event generator Herwig 7.2 [56] is used with its default settings. The Herwig events are analysed with a Rivet routine [57].
Apart from MC event generators one can also make use of fixed order calculations. NNLOJET [58–61] with the NNPDF3.1 PDF set provides predictions in next-to-next-lo-leading order (NNLO) in perturbative QCD for the process $ep \to e + 2\text{jets} + X$. To transfer these parton-level calculations to particle level, non-perturbative correction factors need to be applied. These multiplicative factors are obtained from Pythia 8.3 and correct for hadronisation effects. The calculations are valid only in the region where the $2 \to 2$ process dominates and the hadronisation corrections are small. This corresponds to the 1-jettiness range $0.22 \lesssim \tau_1^b < 1$. The factorisation and renormalisation scales are identified with $\mu = Q$. Varying the scale by factors of 0.5 and 2 in a 7-point scale-variation provides the scale uncertainties. NLO predictions are obtained from NNLOJET as well.

# Chapter 3

# Experimental setup

This chapter discusses the experimental setup. The HERA *ep* collider and the H1 experiment are introduced. The focus is on detector components relevant for the analysis. Following are sections on the data analysis, including the utilised Monte Carlo event generators, data preservation efforts at H1 and the analysis framework. The chapter concludes with methods for the kinematic reconstruction of single events.

## 3.1 The HERA collider

The HERA accelerator (abbreviation for German Hadron Elektron Ring Anlage) was an electron proton ring collider at DESY in Hamburg. It was situated in a tunnel between 10 and 20 m below the surface and had a circumference of 6.2 km. The electrons and protons were provided by the pre-accelerator PETRA. A schematic drawing of the accelerator complex is shown in figure 3.1. The HERA accelerator was operated from 1992 to 2007. During the years 2000 through 2002 a luminosity upgrade was performed. The interruption resulted in two separate operation periods, denoted HERA-I (pre-upgrade) and HERA-II (post-upgrade). In this thesis only data taken in the HERA-II period will be analysed. The data were taken in four intervals, two periods with electron- and two periods with positron-proton scattering.

The two multi-purpose collider experiments H1 and ZEUS were installed in the experimental halls north and south, respectively. In the eastern and western experimental hall the two fixed-target experiments HERMES and HERA-B were located. HERMES used the lepton beam on a gas target to measure polarised lepton-nucleon scattering. HERA-B made use of the proton beam and a wire target to measure the production cross section of B-mesons.

During the HERA-II data taking period, the electron had an energy of $E_e = 27.6$ GeV, while the proton had an energy of $E_p = 920$ GeV. This corresponds to a centre of mass energy of

$$\sqrt{s} \approx \sqrt{4E_e E_p} = 319 \text{ GeV} \tag{3.1}$$

where the particle rest masses have been neglected. Another important quantity of a ring accelerator is its luminosity $\mathcal{L}$. For two beams colliding head-on, it is given by [63]

$$\mathcal{L} = \frac{n_e n_p f_0}{4\pi\sigma_x\sigma_y} \tag{3.2}$$

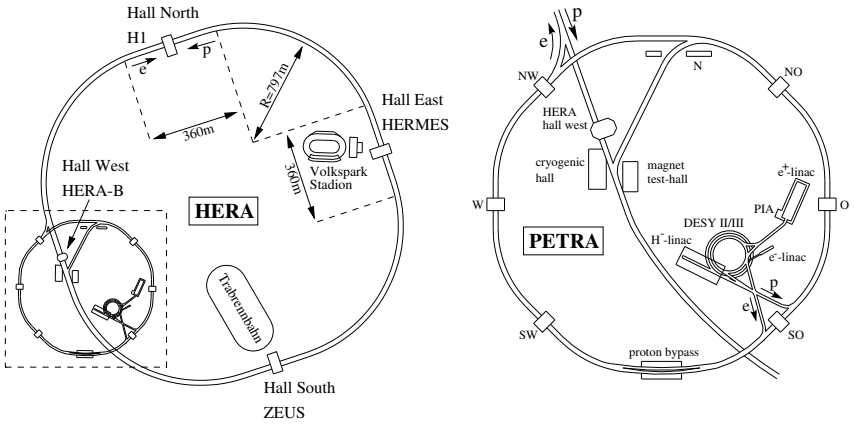


Figure 3.1: Illustration of the HERA accelerator and the location of the four experiments H1, ZEUS, HERA-B and HERMES. The right figure shows the arrangement of the pre-accelerators. Figure taken from [62].

in units of $\mathrm{cm}^{-2}\mathrm{s}^{-1}$. $f_0$ is the collision frequency and $n_p$ and $n_e$ denote the number of protons and electrons in one bunch, respectively. $\sigma_x$ and $\sigma_y$ relate to the transverse expansion of the beams. The integrated luminosity $L$ is directly proportional to the number of interactions

$$N = \sigma \cdot L = \sigma \cdot \int \mathcal{L} dt, \tag{3.3}$$

where $\sigma$ denotes the total interaction cross section. The H1 luminosity was obtained from the measurement of a theoretically well understood process, the Bethe-Heitler process $ep \to ep\gamma$. The photon is emitted from the electron with a small angle with respect to the beam axis. It is detected with dedicated detectors located at small angles. Electron synchrotron radiation and acceptance effects, caused by elements of the beam pipe separating the Bethe-Heitler photons and electrons from the circulating beam particles can result in large systematical uncertainties. Therefore, the luminosity measurement was later repeated exploiting the elastic QED Compton process $ep \to ep$ [64]. The electron and the photon were detected in the backwards calorimeter, the SpaCal. The two measurements are found to be compatible. The integrated luminosity of the analysed data set amounts to $L = 351.6\ \mathrm{pb}^{-1}$ [65].

## 3.2 The H1 detector

The H1 detector was one of two $4\pi$ multi-purpose detectors at HERA. The detector was located in the north experimental hall. Its spatial dimensions were about $12 \times 10 \times 15$ m with a weight of approximately 2800 tons. The detector consists of multiple subdetectors which are arranged around the beam pipe in several layers. A schematic drawing of the detector is shown in figure 3.2. The H1 detector consists of tracking detectors and calorimeters, comprised of a hadronic and an electromagentic part. The subdetectors were installed in a cryostat vessel. The vessel was surrounded by a superconducting solenoid providing an axial magnetic field of 1.15 T. The iron yoke of the magnet was equipped with streamer tube detectors for muon detection. Inside and outside of the iron yoke additional detectors for muon identification were mounted. In the following, only the relevant components for the event shape analysis will be discussed. A full description of the detector components can be found elsewhere [66, 67].

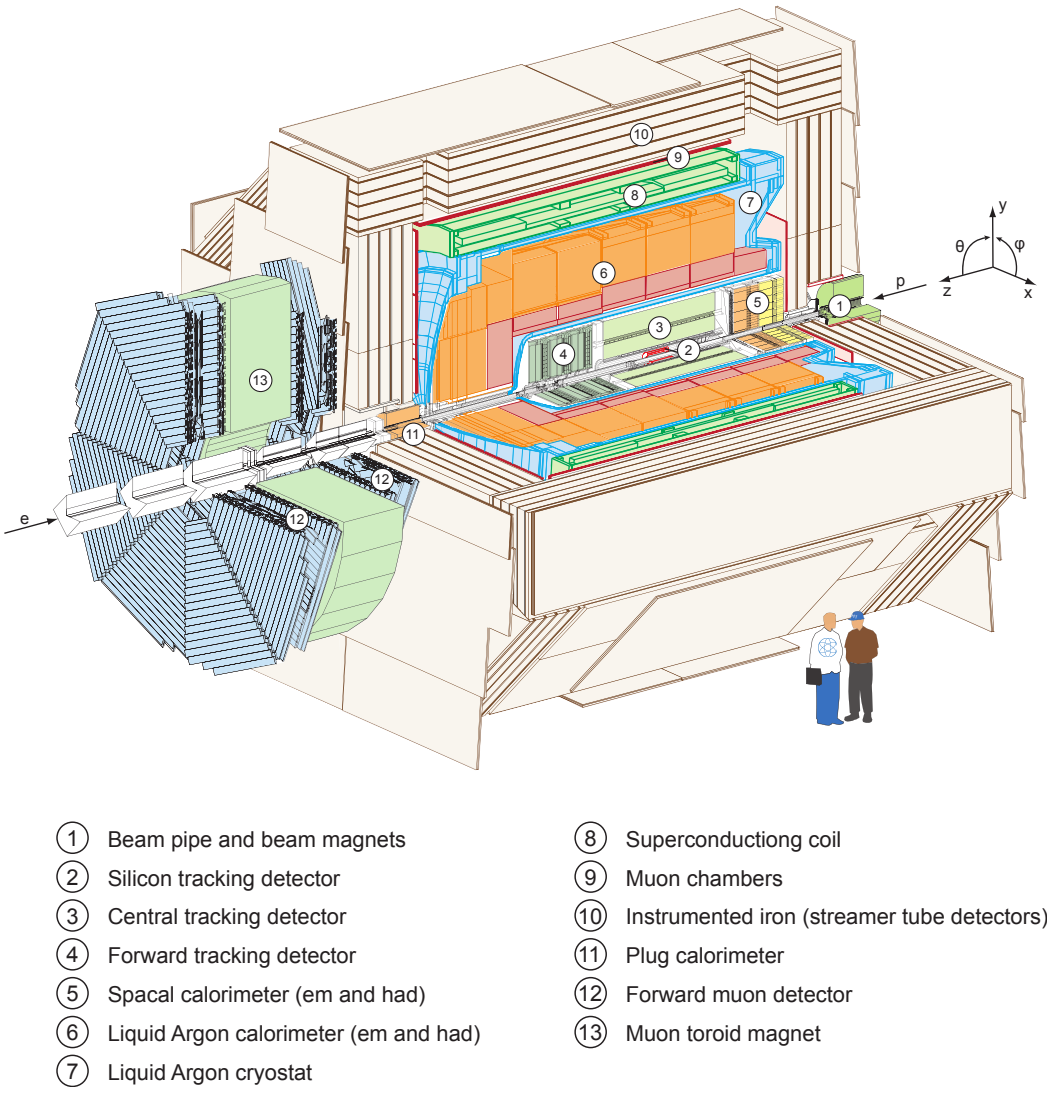


Figure 3.2: Schematic drawing of the H1 detector, based on a GEANT3 [68] detector simulation.

### 3.2.1 The H1 coordinate system

The $+z$-axis of the right-handed H1 reference frame is oriented along the proton beam direction. The $+x$-axis points to the centre of the HERA ring collider. The origin of the reference frame coincides with the nominal interaction point (IP). Instead of using Cartesian coordinates, one usually prefers a spherical coordinate system. The polar angle $\vartheta$ is defined with respect to the $z$-axis. It ranges from 0 to $\pi$, where $\vartheta = \pi$ corresponds to the direction of the electron beam. The azimuthal angle $\varphi$, ranging from 0 to $2\pi$, is defined with respect to $x$-axis in the $(x, y)$-plane.

### 3.2.2 Track detectors

A track in particle physics denotes the trajectory a charged particle leaves in the detector. From the curvature of the track in the $(x, y)$-plane and an $\eta$ measurement for the $z$-component, the particle charge and momentum can be derived. The particle may be identified when the characteristic energy loss in a medium is taken into account as well. The tracking detectors surround the beam pipe as the innermost detector layer.
The tracking system is subdivided into three parts, the Forward Tracking Detector (FTD), the Central Tracking Detector (CTD) and the Backward Proportional Chamber (BPC). The silicon tracking detector [69,70] directly surrounded the interaction region and enabled a precise vertex reconstruction. It was subdivided in the barrel like Central Silicon Track detector (CST) and two endcaps in the backward (BST) [71] and forward (FST) [72] direction.
The main component of the CTD are two concentric drift chambers, the Central Jet Chambers (CJCs) 1 and 2. They cover the full azimuthal angle and an angular range of $15^{\circ} < \vartheta < 165^{\circ}$. The employed sense wires were orientated parallel to the beam pipe. The CJC1 was encapsulated by the two thin proportional chambers optimized for triggering, the Central Inner and Outer Proportional chamber (CIP / COP). To ensure a precise measurement of the $z$-coordinate the Central Outer $z$-Chamber (COZ) was installed. It is a thin drift chamber located between CJC1 and COP.
The FTD extended the tracking coverage in the polar angle to $5^{\circ} < \vartheta < 25^{\circ}$. It consisted of three supermodules, each containing four to five drift chambers with different wire geometries.
The BPC completes the tracking system. It was located in front of the SpaCal (see sec. 3.2.3). Its main purpose was to discriminate between charged and neutral particles going in the backward direction, while also improving the position measurement of those particles.

### 3.2.3 Calorimeters

A calorimeter measures the energy of incident particles. The calorimeter system at H1 is subdivided into the Liquid Argon calorimeter (LAr) [73] and the so-called Spaghetti Calorimeter (SpaCal) [66]. Each subsystem consists of an electromagnetic and a hadronic part.
The LAr covered the angular range of $4^{\circ} < \vartheta < 154^{\circ}$ in the polar angle. It provided full coverage in the azimuthal angle. The calorimter was installed within a single cryostat filled with liquid Argon at a temperature of 90 K. The LAr enabled a reliable identification and measurement of electrons in combination with a good hadronic measurement. The calorimeter consists of active and passive parts. The passive layers were made of lead or stainless steal for the electromagnetic and hadronic part, respectively. A heavy material with high atomic number is chosen to generate and absorb particle cascades. The active layers in between generate the signal through ionisation and charge collection. The LAr is subdivided in approximately 45 000 individual calorimeter cells structured in seven layers. Neighbouring cells with energy deposits are grouped into clusters [74]. To account for the different detector responses to hadronic and electromagnetic clusters, a software compensation procedure is performed on them [73, 75].
The LAr calorimeter is of crucial importance for this analysis. It identifies and measures final state energy of the scattered electron as well as a large fraction of the hadronic final state. It is also used as a trigger for single events.
The SpaCal was installed in the backward detector region behind the BPC and covers the range $153^{\circ} < \vartheta < 178^{\circ}$ in the polar angle. It was designed for the precise measurement of electrons scattered under a large angle. This event configuration appears mainly in low-$Q^2$ events. The SpaCal consisted of an hadronic and an electromagnetic part, both were built out of lead pas-

sive layers and active layers made out of scintillating fiber. The long and thin fibres give the *Spaghetti* Calorimeter its name.

### 3.2.4 Trigger system

HERA had a bunch crossing frequency of 10.4 MHz. This rate by far exceeds the frequency at which data could be written out of about 10 Hz. A four level trigger system was used at H1 to scale the frequency down and to reject background events. The level 1 trigger consisted of 256 elements combined into 128 raw triggers. It had practically no dead time. Many of the raw triggers were tuned to selected physics processes. The second trigger level consisted of the topological trigger and the independent neural network trigger [76]. The level 2 trigger was used to validate or disprove the level 1 trigger information within 20 $\mu$s. The third level Fast Track Trigger (FTT) [77, 78] was optimised for the detection of heavy quark decays. It was commissioned in 2005 and had a latency time of about 100 $\mu$s. The fourth trigger level was used for a full event reconstruction and classification. The raw data are stored in the Production Output Tapes (POT). The reconstructed quantities from all detector components are written to the Data Summary Tapes (DST). The overall dead time amounted to 100 ms.
In this thesis the trigger element s67 was used which is a logical conjunction of three level one triggers [79]. It triggers on a compact energy deposit in the electromagnetic section of the LAr stemming either from the scattered lepton or a jet.

## 3.3 Event generators and detector simulation

Monte Carlo (MC) event generators are the standard tool in modern particle physics to simulate high energy particle collisions. The simulations are used together with a detailed simulation of the detector to correct the data for detector effects like acceptance and resolution. Perturbative QCD is used to calculate the process QCD Born level diagrams. In the next step, the parton shower is simulated. This defines the parton level. To obtain physical particles, e.g. baryons and mesons, various implementations of hadronisation models are available. However, this so-called particle level, consisting of stable particles can not be directly observed in the detector. The detector specific geometry and resolution is simulated in a separate step. The resulting four-vectors define the detector level. The utilised MC models are briefly presented in the following.

#### Rapgap

The Rapgap 3.1 event generator [49] is used for the simulation of NC DIS signal events. It combines the QPM and dijet matrix elements for $\gamma$ and $Z_0$ exchange matched with DGLAP parton showers (MEPS). The hadronisation is modelled with the Lund string fragmentation [26] as implemented in the package JETSET [80, 81]. Higher order QED effects are implemented using HERACLES [82, 83]. That includes real radiation from the lepton, vertex corrections and vacuum polarisation.

#### Djangoh

A second independent MC generator to model NC DIS events is Djangoh 1.4 [48]. It has been developed as an interface between LEPTO [84] and HERACLES [82, 83]. An implementation of the Colour Dipole Model (CDM) [25] according to ARIADNE [85] is included in current versions to simulate parton showers. In the CDM, parton radiation is modelled through gluon emission

from colour dipoles, instead of using quark and gluon splittings.

**Background processes**

The background processes are simulated with dedicated MC models. Low virtuality events $4 < Q^2 < 60$ GeV$^2$ are simulated with Djangoh. Pythia 6 [86, 87] is used for the simulation of light and heavy quark production in photoproduction. Photoproduction describes a scattering process with vanishing $Q^2 \approx 0$ GeV$^2$. Quasi-real QED Compton (QEDC) processes $ep \to e\gamma X$ are simulated with the COMPTON generator [88, 89] QEDC events are removed from Djangoh and Rapgap and are instead simulated with COMPTON to get a reliable estimation of the contribution to the background. GRAPE [90] is used to estimate the contribution from lepton pair production $ep \to el^+l^-X$, where $l$ can be an electron, a muon or a tau lepton.

**Detector simulation**

A simulation of the H1 detector is shown in figure 3.2. It was generated with the H1Sim [91] package developed by the H1 collaboration. H1Sim is based on GEANT3 [68] and includes fast shower simulations [92–95]. The detector geometry is implemented, as well as the interaction of particles with matter and the response of the detector. After the installation of the full detector, the simulation was constantly refined with $ep$ data. The simulated events are stored in the same format as the real data. Real and simulated events are treated in the same way, using the same analysis chain and the same reconstruction methods.

## 3.4 H1 data preservation

HERA, being the only high energy $ep$ collinder constructed so far, provided a unique data set. The data enables a detailed study of e.g. the proton structure, which makes it valuable also for future generations. This motivated the efforts to preserve the H1 data and the analysis framework.

The total volume of $ep$ collision data recorded by the H1 detector amounts of approximately 1 billion events, corresponding to about 75 TB in the RAW data format. The H1 core software, almost entirely written in FORTRAN 77, creates the basic format DST (Data Summary Table, $\approx$ 20 TB) from the RAW data. The MC events are produced in the same format as the data. The same reconstruction software is applied to data and simulated MC events.

The analysis framework H1oo [96] written in C++ was first developed in 2000 to improve the overall efficiency in H1 physics analyses. Three data formats are available simultaneously, HAT (H1 Analysis Tag) containing simple calibrated variables for a fast event selection, mODS (micro Object Data Structure) which provides additional information on identified particles and ODS (Object Data Store) which gives access to the full information stored on the DST Files in the ROOT format. The ODS may be accessed during an analysis event loop.

The Data Preservation in High Energy Physics (DPHEP) [97] study group was formed in 2008, one year after data taking at the H1 experiment ended. Its purpose was to systematically evaluate all organisational and technical aspects to preserve high energy physics data for the long term use. The total volume of the preserved H1 data amounts to about 0.5 PB [98, 99]. It includes all software and the analysis level data formats, as well as the RAW data. This corresponds to a DPHEP level 4 preservation model [100].

In 2020, the H1oo analysis framework was migrated to ROOT6 [101] and C++17. This enabled the use of modern analysis tools and provided and up-to-date and instructive environment for H1 newcomers. The full functionality of H1oo is now also available with PYTHON, thanks to

ROOT's automatised PYTHON-C++ bindings. As a side effect, the maintenance costs were reduced [99].

## 3.5 Analysis framework

For the purpose of this analysis, the 1-jettiness analysis framework interfacing the H1oo software package was developed. Starting from a basic main routine, most of the framework was developed within this thesis. As an input, pre-selected DST files are used. Steering files were put together to process the HERA II data set. Monte Carlo samples had to be reproduced and validated. The code uses features from C++20. It is separated in functions processing detector level quantities, generator level quantities and dedicated functions to calculate the cross sections. The procedure to correct for detector effects (cf. section 5.2) and electron QED radiative effects (cf. section 5.3) was developed. A way to obtain the systematical uncertainties was implemented. All plotting scripts had to be written. The analysis code is accessible for H1 members via the DESY–IT central Git repository hosting service Bitbucket [102]. Several ongoing analyses are based on the developed code.

## 3.6 Kinematic reconstruction of one event

For a precise measurement of the 1-jettiness an exact reconstruction of the kinematic variables $x$, $y$ and $Q^2$ has to be ensured. There are different possibilities to reconstruct $x$, $y$ and $Q^2$ from the scattered electron and the hadronic final state. Various reconstruction methods will be discussed in this chapter. A detailed overview on reconstruction methods in DIS is also given in [103].
The electron method uses the energy $E_{e'}$ and polar angle $\vartheta_{e'}$ of the scattered electron for the reconstruction. It enables an experimentally simple and precise reconstruction in the high $y(> 0.2)$ region. At low $y$ ($\lesssim 0.2$), however, the resolution decreases, due to the $1/y$ term in the error propagation of $y_e$ [104].
The hadron method gives a rather poor $Q^2$ resolution, due to hadron losses in the beam pipe. $y$ can be measured precisely in the low and medium $y$ range. At high $y$ the measurement degrades [104]. It makes use of two quantities calculated from the hadronic final state, its total transverse momentum

$$T = \sum_h \sqrt{p_{x,h}^2 + p_{y,h}^2} \tag{3.4}$$

and $\Sigma$ defined as the sum of $E - p_z$ of each particle

$$\Sigma = \sum_h (E_h - p_{z,h}). \tag{3.5}$$

From momentum conservation one obtains the relation

$$\Delta \equiv \Sigma + E_{e'}(1 - \cos\vartheta) = 2 \cdot E_e \tag{3.6}$$

where $E_e$ denotes the energy of the beam electron. Equation (3.6) will come back in section 4.1 as a condition for the events selection. To obtain a reconstruction method accurate over the entire $y$ region the $\Sigma$ method is introduced. Using the definition of $\Sigma$, the inelasticity can be

expressed as

$$y_\Sigma = \frac{\Sigma}{\Sigma + E_{e'}(1 - \cos\vartheta_{e'})}. \tag{3.7}$$

Using $\Sigma$, $E_{e'}$, $\vartheta_{e'}$ and $s$ one can also find expressions for $Q^2$ and $x$ (cf. table 3.1). In early H1 event shape analyses the electron method was used together with the hadron method [32, 33]. Later, a combination of electron and $\Sigma$-method, the so-called e$\Sigma$-method was preferred [34]. This mixed method makes use of the precise measurement of $Q^2$ with the electron method and reconstructs $x$ according to the $\Sigma$ prescription. Another possibility is to eliminate $s$, and hence the beam electron, in the calculation of $x$. For the resulting I$\Sigma$ method, smaller distortions from QED electron radiative effects in the reconstruction are expected. The formulae for $x$, $y$ and $Q^2$ for all discussed reconstruction methods are summarised in table 3.1.

| Method | $y$ | $Q^2$ | $x$ |
|---|---|---|---|
| $e$ | $1 - \frac{E_{e'}}{E_e}\sin^2(\vartheta_{e'}/2)$ | $4E_eE_{e'}\cos^2(\vartheta_{e'}/2)$ | $Q^2/ys$ |
| $h$ | $\frac{\Sigma}{2E_e}$ | $\frac{T^2}{1-y_h}$ | $Q^2/ys$ |
| $\Sigma$ | $\frac{\Sigma}{\Sigma+E_{e'}\cdot(1-\cos(\vartheta_{e'}))}$ | $\frac{E_{e'}^2\sin^2(\vartheta_{e'})}{1-y_\Sigma}$ | $Q^2/ys$ |
| I$\Sigma$ | $y_\Sigma$ | $Q^2_\Sigma$ | $\frac{E_{e'}}{E_p}\frac{\cos^2(\vartheta_{e'}/2)}{y_\Sigma}$ |
| $e\Sigma$ | $\frac{2E_e\Sigma}{(\Sigma+E_{e'}(1-\cos\vartheta_{e'}))^2}$ | $Q^2_e$ | $x_\Sigma$ |

Table 3.1: Formulae for the reconstruction of $x$, $y$ and $Q^2$ using different reconstruction methods [104,105]

# Chapter 4

# On the feasibility of a measurement of the 1-jettiness

The 1-jettiness has never been measured in DIS before. According to equation (2.26), all particles in the current hemisphere contribute to the observable, independent of their position in the detector. To ensure that the 1-jettiness can indeed be measured at H1, a set of control plots and detector level studies will be presented in this chapter.

## 4.1 Event selection

For the 1-jettiness analysis, only neutral-current high-$Q^2$ events are considered. To meet these requirements and to ensure that only well measured events are selected, several cuts on detector level have to be passed.
The events are triggered by a highly energetic cluster resulting from a jet or the scattered electron in the electromagnetic part of the LAr calorimeter. The highest isolated transverse momentum cluster with a track associated to it identifies the scattered electron. Its energy $E_{e'}$ needs to exceed 11 GeV. Additional information on the isolation criteria and the electron finding algorithm can be found in [106]. In the central detector region $30^{\circ} < \vartheta'_e < 153^{\circ}$, the associated track has to be measured by the CTD and matched to the primary interaction vertex. The requirement of an associated track reduces the probability to wrongly identify the scattered leptons to below 0.3 % [79]. The overall trigger efficiency is above 99.5 % [107].
Figure 4.1 shows the detector level distribution of the polar angle $\vartheta_{e'}$ and energy $E_{e'}$ of the final state electron. In the upper panel the data is compared to the MC models Rapgap and Djangoh. The background contribution is shown in a stacked style. The largest contributions are photoproduction and low-$Q^2$ ($< 60\,\mathrm{GeV}^2$) NC DIS events. The other contributions, such as QED Compton events and lepton pair production are included in the Low-$Q^2$ NC DIS curve for better readability. The overall background contribution in the selected phase space is small. The lower panel shows the ratio of the MC models to the data. The background was added to the simulations for a better comparison. The $\vartheta_{e'}$ distribution exhibits a tail at low values and increases towards $\vartheta_{e'} = 153^{\circ}$. After crossing this value the distribution is falling steeply, since the electron is required to be reconstructed in the LAr. In the right panel the energy distribution is displayed. The requirement on the energy of the final state electron $E_{e'} > 11$ GeV can be observed. The distribution peaks at $E_{e'} = 27.6$ GeV which is the energy of the initial beam elec-

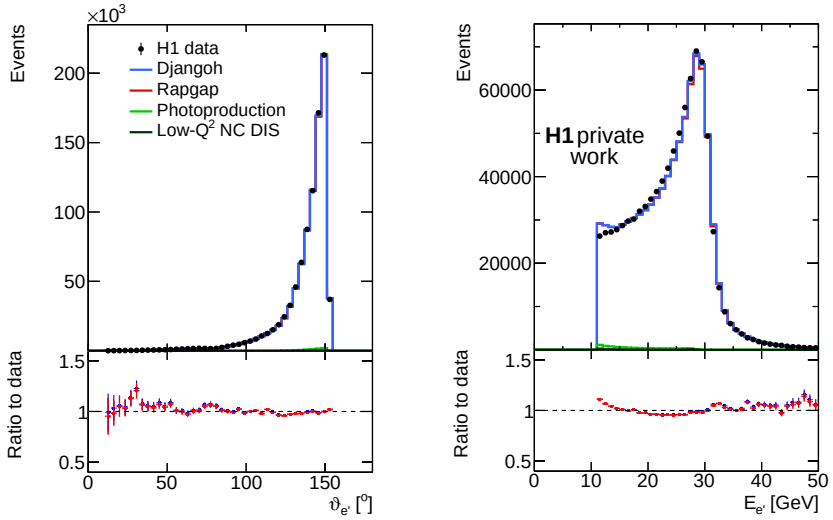


Figure 4.1: Detector level distribution of the energy $E_{e'}$ and the polar angle $\vartheta_{e'}$ of the scattered electron. The data is shown alongside the MC event generators Djangoh and Rapgap. Background processes simulated with dedicated programs are added to both models. The most relevant background processes are low-$Q^2$ NC DIS ($Q^2 < 60\,\mathrm{GeV}^2$) and photoproduction, displayed in a stacked style. Other processes are found to be negligible. The photoproduction represents the sum of all background processes. The lower panel schows the ratio of the MC models to the data. The legend for both plots is given in the left panel.

tron. Both, the electron energy and the polar angle distribution are well described by Rapgap and Djangoh.

The proton and the electron bunch have a longitudinal beam size of $\sigma_z^p \approx 13$ cm and $\sigma_z^e \approx 2$ cm, respectively. Since only events at high $Q^2$ will be analysed, the transverse extent can be neglected. The $z$-coordinate of the primary vertex is required to be within 35 cm of the nominal position of the interaction point. This corresponds to approximately three standard deviations, assuming the distribution of the $z$-vertex is Gaussian. The central inner and outer proportional chamber are used for a fast vertex reconstruction. The reconstruction is later validated with a vertex fitted electron track. A nuclear interaction finder reduces the fraction of events where an electron is not fitted to the primary vertex to about 0.3% [108]. Those events are well modelled and can also be used in the analysis. To simulate the $z$-vertex distribution, it is measured for each run period. Run-dependent weights can then be derived and applied to the simulated events to correct for shifts with respect to the data [108,109]. The distribution of the reweighted $z$-vertex position is shown on the left panel in figure 4.2. After applying the reweighting, an excellent agreement between the data and both signal MC models is observed.

The right plot in figure 4.2 displays the detector level distribution of the total $E - p_z$ of the event. This quantity was introduced as $\Delta$ in equation (3.6). Momentum conservation dictates $\Delta = 2E_e = 55.2$ GeV. This condition can be used to introduce the cut $45 < \Delta < 65$ GeV. Consequently, events with hard initial state electron QED radiation or badly measured events can be excluded.

The cuts that were introduced in this section so far define the pre-selection. Only events fulfilling all requirements will be considered in the following.

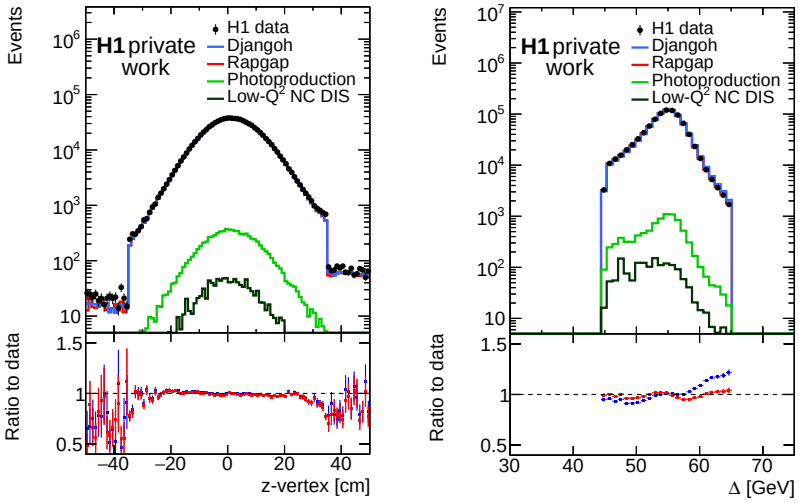


Figure 4.2: Detector level distributions of the $z$-position of the reweighted primary interaction vertex (left) and of $\Delta = E - p_z$ (right). The data are compared to simulated events using the MC signal generators Djangoh and Rapgap.

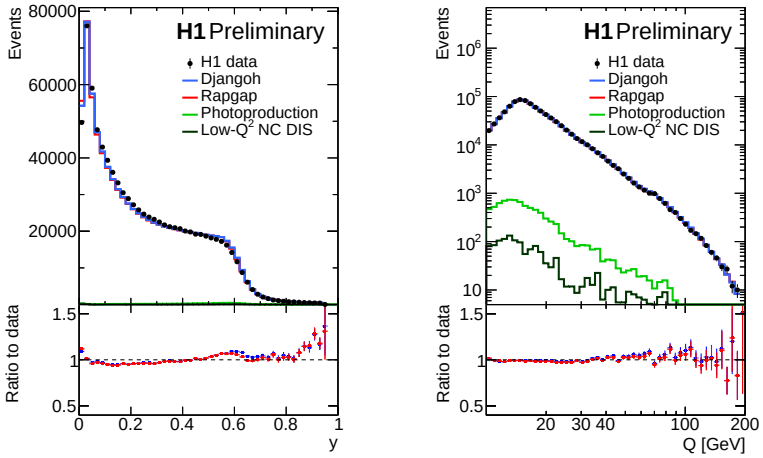


Figure 4.3: Detector level distributions of $y$ (left) and $Q$ (right) of all pre-selected data. The kinematic observables are defined with the IΣ method according to table 3.1.

Figure 4.3 shows the detector level distribution of $y$ (left) and $Q$ (right) for all prior selected events. Both observables are reconstructed with the IΣ method, according to section 3.6.
The $y$ distribution presented in figure 4.3 peaks at $y \approx 0.05$. The hadronic final state of events with small $y$ is collimated in the very forward direction which limits the measurement due to sizable acceptance and resolution effects. Hence, the analysis is restricted to $y > 0.2$ for the single-differential cross section measurement. The drop in the distribution at $y \approx 0.7$ is caused by the requirement on the electron energy of $E_e > 11\,\text{GeV}$. As a consequence, an additional cut on high-$y$ is imposed. For the single-differential measurement it is at $y < 0.7$. For the triple differential measurement it is possible to extend the $y$-range down to $y > 0.1$ at low $Q^2$ and up

to $y < 0.9$ at high $Q^2$.
The turnover in the $Q$ distribution at about $Q \approx 15\,\text{GeV}$. can be traced back to the requirement, that the scattered electron had to be reconstructed in the LAr. At high $Q$ the statistics are limited. Both effects combined result in the condition $12.2 \lesssim Q \lesssim 141.4$ GeV. Both MC models describe the kinematic variables with high accuracy.

## 4.2 Particle reconstruction in the current hemisphere

To ensure that all detector effects, such as imperfect resolution and detection efficiency are under control, a single particle study is performed. Particles in the current hemisphere of the Breit frame ($\eta^{\text{Breit}} < 0$) contribute to the observable. Only those particles will be considered in the following.
The DIS thrust measures the sum of longitudinal momenta in the current hemisphere. The distribution of longitudinal momenta of the single particle candidates (denoted as particles) are shown in figure 4.4.

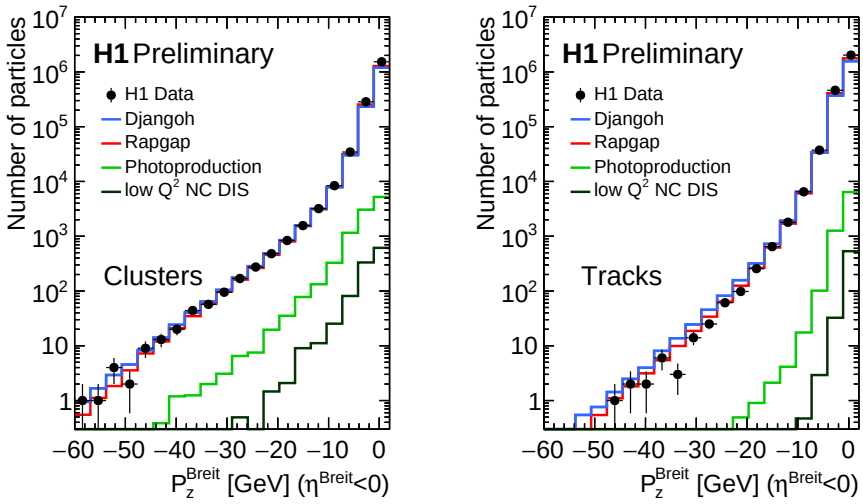


Figure 4.4: The longitudinal momentum $P_z^{\text{Breit}}$ in the Breit frame of reconstructed particles. Particles in the beam hemisphere are not displayed since they do not contribute to the observable. The $P_z^{\text{Breit}}$ distribution for clusters and tracks are shown on the left and right, respectively.

The left plot shows the distribution of neutral particles denoted as clusters. The right plot shows the distribution of charged particles. They are reconstructed from tracks in the detector. The single particles are reconstructed with a particle flow algorithm [110–112] which takes cluster and track information into account. However, at the end each particle is classified as either a cluster or a track. This avoids double counting of particles. The signal MC models Rapgap and Djangoh describe the single particle distributions accurately. The contribution from background processes is small.
The DIS thrust is a "$4\pi$ observable". This means that all particles in the current hemisphere contribute to the sum, independent of their position in the detector. However, particles in the

very forward and backward region can not be reconstructed as precisely as particles in the central detector region. To study the contribution of different detector regions to the observable, the sum in the $\tau_Q$ definition is split into six parts

$$\tau_Q = 1 - \frac{2}{Q} \cdot \sum_{i \in \mathcal{H}_C} p_{i,z} = 1 - \frac{2}{Q} \cdot \sum_{j=1}^{6} \sum_{i \in \mathcal{H}_C,} p^j_{i,z}.$$

$j$ runs over cluster and track contributions each subdivided in the forward ($\vartheta > 153^o$), central ($25^o < \vartheta < 153^o$) and backward ($\vartheta < 25^o$) detector region. The regions are defined according to $\vartheta$-ranges, where different components of the H1 detector are relevant for particle reconstruction [66, 67, 69, 113].

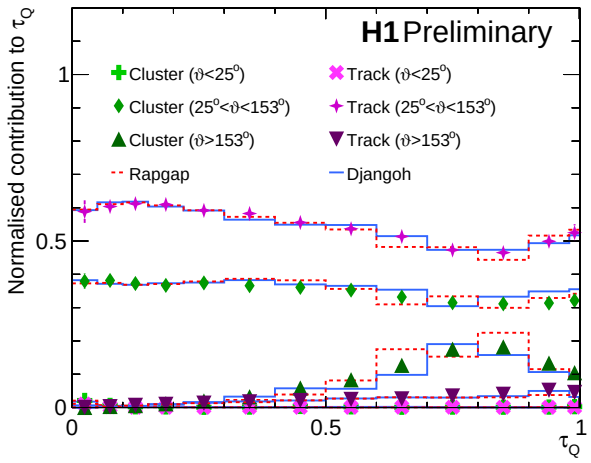


Figure 4.5: The normalised contribution to $\tau_Q$ for differently reconstructed particle candidates (tracks or clusters) in three distinct $\vartheta$ regions. More information on the plot is given in the text.

The single contributions are plotted in figure 4.5. For every event and every contribution the weight $w = \sum_{\text{contrib}} P_z^{\text{Breit}} / \sum_{\text{all}} P_z^{\text{Breit}}$ is calculated. It defines the relative contribution to the observable. The resulting curves are normalised to add up to one.
Studying the contributions of particles in different detector regions shows, that mainly particles in the central detector contribute to the observable. Only at high $\tau_Q$ one can observe an effect from clusters in the forward detector region. The data are compared to the signal MC models Djangoh and Rapgap. A good agreement between the simulation and the data can be observed.
The procedure is repeated for different intervals of single particle energies. The resulting plot is shown in figure 4.6. Most contributing particles have an energy larger than 1 GeV. This changes only in the last two bins. In the second to last bin $0.90 < \tau_Q \leq 0.98$ also particles with medium energy $0.3 < E < 1.0$ GeV contribute. The last bin $0.98 < \tau_Q \leq 1.0$ is not meaningful in this study. It is filled with events with almost empty current hemisphere. In this bin only very few particles contribute at all.
From the two plots it can be concluded, that mainly particles in the central detector with high energy contribute to the observable. Those particles can be measured with high precision.

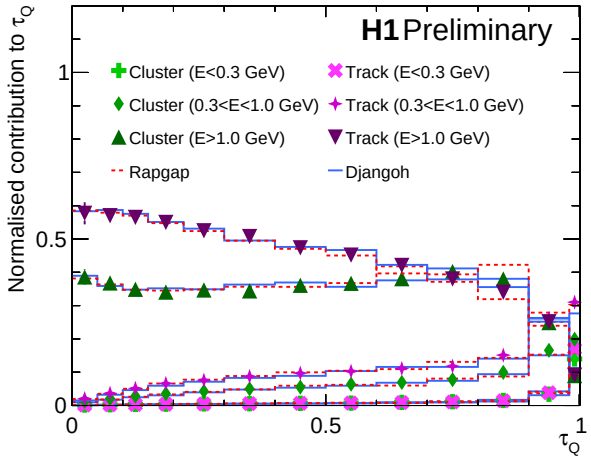


Figure 4.6: The normalised contribution to $\tau_Q$ for different ranges of single particle energies $E$. Clusters and tracks are treated separately.

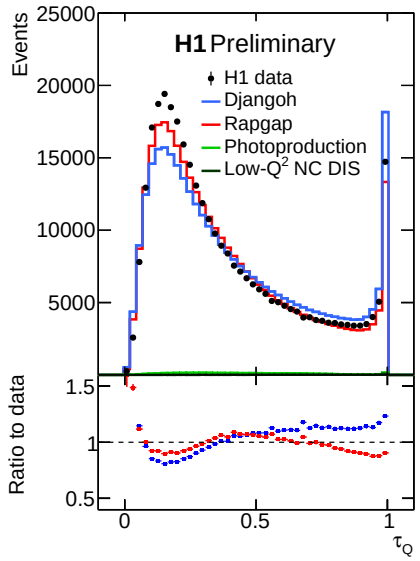


Figure 4.7: Detector-level distribution of $\tau_Q$ of the pre-selected data and in the phase space $150 < Q^2 < 20\,000\,\mathrm{GeV}^2$ and $0.2 < y < 0.7$. The data are compared to simulated data using Djangoh or Rapgap. Both models provide a satisfactory description of the data and mainly bracket the data.

After defining the detector level cuts and confining the phase space, the detector level $\tau_Q$ distribution can be studied. It is presented in figure 4.7. The background contribution is negligible and can not be seen on a linear scale. One can observe a two peak structure in the distribution. The region $\tau_Q \approx 0.2$ consists of events with a 1-jet topology. This region will be denoted as peak region in the following. Events with two or more jets contribute to the tail region $\tau_Q > 0.3$. The last bin is filled with events with empty current hemisphere. The lower panel

shows again the ratio of the two MC models Djangoh and Rapgap to the data. The description is reasonable, however discrepancies between Djangoh and Rapgap can be observed. Rapgap describes the peak region well, while underestimating the tail region. Djangoh on the other hand overestimates the tail region and the $\delta$-peak in the last bin. This behaviour matches with the experiences from previous analyses. Djangoh has a 'harder spectrum', e.g. more dijet events than Rapgap [114]. The shape in the ratio is explained by the different physics implementations in the models. It is not caused by detector effects.

## 4.3 Acceptance and purity

For the measurement one has to define the binning in the three observables $y$, $Q^2$ and $\tau_Q$. The $Q^2$-binning was adapted from a previous analysis [79], however always two bins were combined into one. To define the binning in $y$ and $\tau_Q$ one can study acceptance $A$ and purity $P$ distributions. The two quantities are defined as

$$A = \frac{N_{rec}}{N_{gen}} \tag{4.1}$$

$$P = \frac{N_{stay}}{N_{rec}} \tag{4.2}$$

where $N_{rec}$ and $N_{gen}$ denote events in one bin on detector and generator level, respectively. The number of events which were generated and reconstructed in the same bin is denoted $N_{stay}$. The final binning for the analysis is given in table 4.1

| $\tau_Q$ | 0.0 | 0.05 | 0.1 | 0.15 | 0.22 | 0.3 | 0.4 | 0.5 | 0.6 | 0.7 | 0.8 | 0.9 | 0.98 | 1.0 |
|---|---|---|---|---|---|---|---|---|---|---|---|---|---|---|
| $Q^2$ [GeV$^2$] | 150 | 200 | 282 | 447 | 708 | 1120 | 1780 | 3550 | 10000 | 20000 | | | | |
| $y$ | 0.1 | 0.2 | 0.7 | 0.9 | | | | | | | | | | |

Table 4.1: This table defines the binning in $\tau_Q$, $Q^2$ and $y$ for the triple differential measurement. The table gives the boarders of each bin.

$A$ can get larger than 1 when events migrate into the bin from different phase space regions. The purity is defined to be strictly $P \leq 1$. Purity and acceptance depend on the binning and on the reconstruction method. The goal is to find the best trade-off between an acceptance close to one, a high purity and a large number of bins. The acceptance distribution for the I$\Sigma$ method for the binning in $y$, $Q^2$ and $\tau_Q$ is presented in figure 4.8. At the lowest $Q^2$ values, the acceptance drops to $\approx$ 50 %. At higher $Q^2$, $A$ is increased and even surpasses one at highest $Q^2$. This can happen when events generated at medium $Q^2$ are reconstructed at high $Q^2$. The second feature one can observe is a slight slope in the distribution. The slope is caused by the imperfect detector resolution. Overall, the values for the acceptance are reasonable.
In the next step, the performance of the I$\Sigma$ and e$\Sigma$ reconstruction methods is compared with regard to the obtained purities. Both reconstruction methods were introduced in chapter 3.6. The reconstruction method mainly affects the reconstruction of the boost to the Breit frame depending on $x$ and $Q^2$.

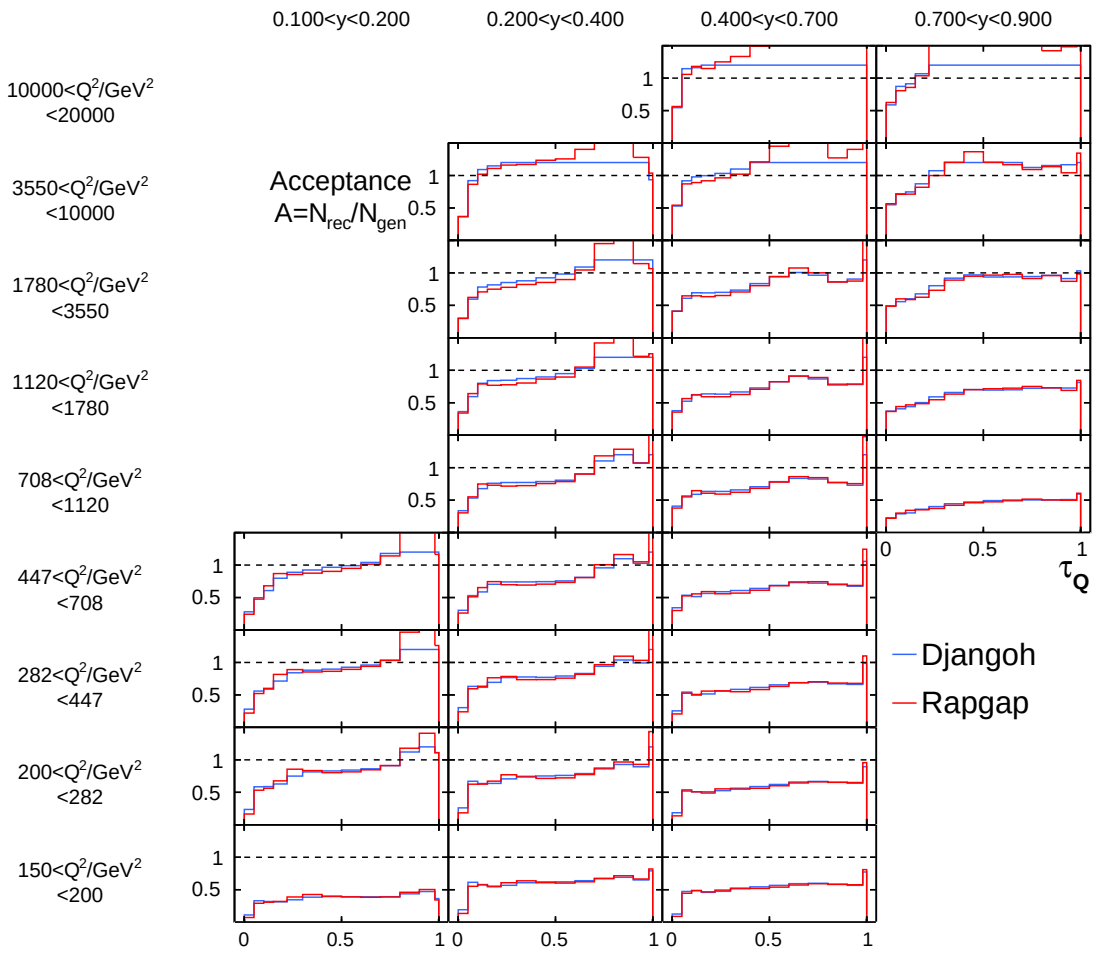


Figure 4.8: Acceptance plot for the triple differential measurement in bins of $\tau_Q$, $Q^2$ and $y$. The events are reconstructed with the IΣ method. The two MC models Rapgap and Djangoh are being compared.

The purities obtained with the IΣ and the eΣ method are shown in figures 4.9 and 4.10. The IΣ method achieves purities above 30 % (indicated by the dashed line) in almost all bins. The distribution is flat for the defined binning. Only at high $Q^2$ - medium $y$ an increasing slope in the distribution can be observed.
At low $Q^2$, the results obtained with the eΣ method are almost identical with those from the IΣ method. However, the purities are decreasing towards lower $\tau_Q$. At high $Q^2$ - medium $y$ the distribution does not exhibit the slope observed in figure 4.9. At high $Q^2$ - high $y$ figure 4.10 displays a distinct shape with purites dropping below 0.1.
The purity serves as a measure to decide which regions of the phase space can be taken into account for the analysis. Achieving high purities over the entire phase space means that a wide range in $Q^2$ and $y$ is measurable. In the case of the 1-jettiness, this is not trivial since all particles in the current hemisphere contribute to an event. One can not apply cuts on minimal $p_T$ or $\eta$ of single particles. High purities at low $y$ means that the detector resolution is sufficient

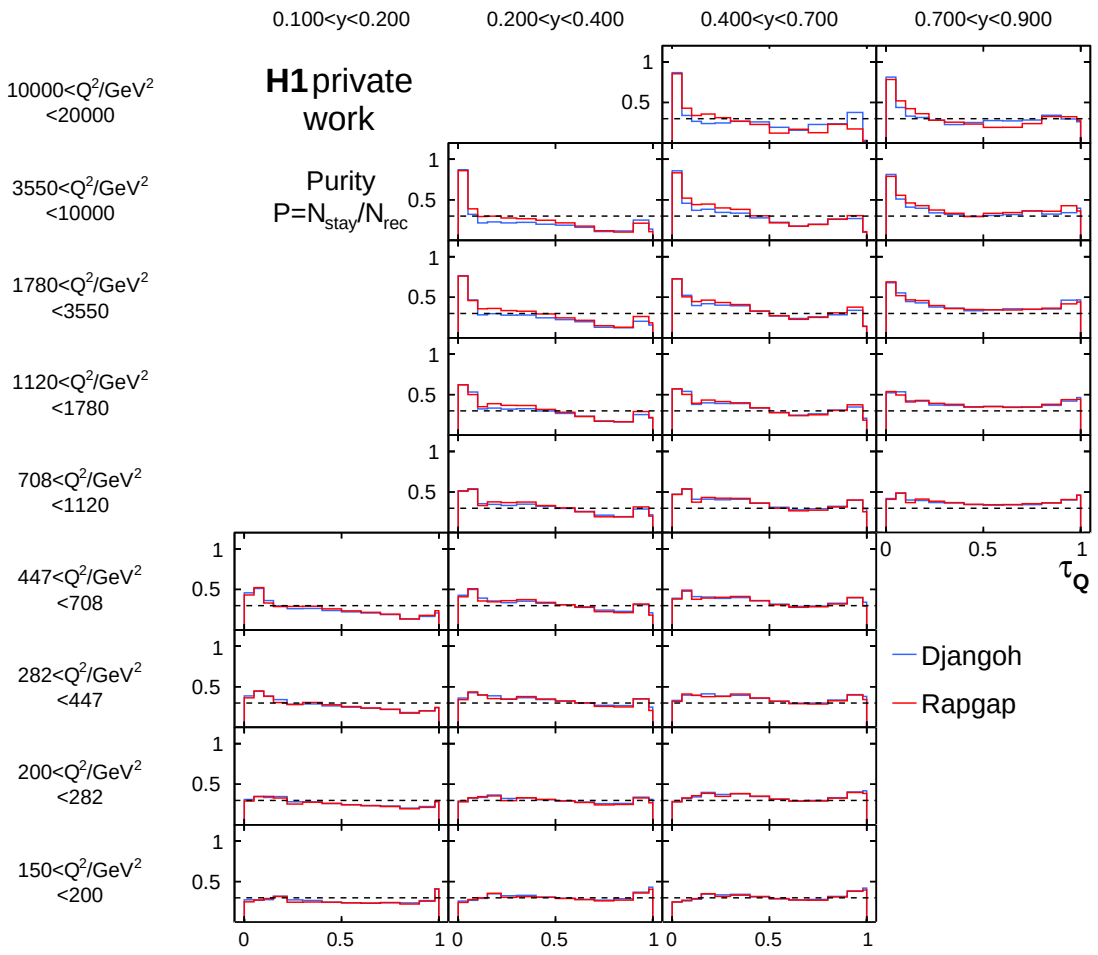


Figure 4.9: Purities for the measurement in $\tau_Q$, $Q^2$ and $y$, obtained with the IΣ reconstruction method. The purity was defined in equation (4.2). The Rapgap and Djangoh models are shown. The dashed line indicates a purity of 30%.

even when the HFS is collimated in the forward detector region. The $\tau_Q$ distribution covers a variety of event topologies in the detector, including DIS one jet events at low $\tau_Q$, multi-jet configurations at medium $\tau_Q$ and dijet events with empty current hemisphere at $\tau_Q = 1$. The entire $\tau_Q$ spectrum can be measured, independent of the position of the HFS in the detector. Overall the obtained purities are satisfactory, keeping in mind that they decrease with each binning dimension. Regarding the purities, the IΣ method outperforms the eΣ method.

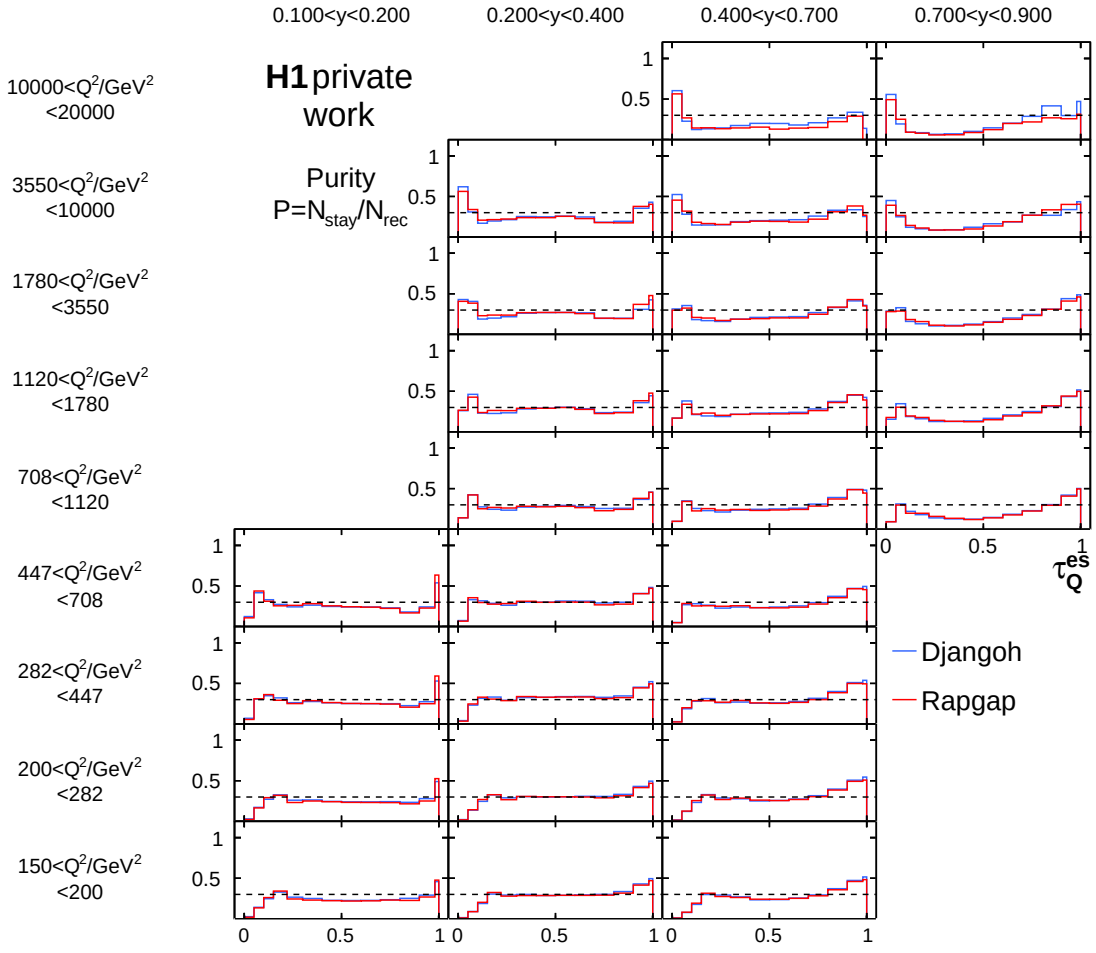


Figure 4.10: The plot is similar to figure 4.9, but the purities were obtained with the eΣ method.

# Chapter 5

# The cross section measurement

The 1-jettiness is calculated for each event individually which is then assigned to a bin according to its $\tau_Q$, $Q^2$ and $y$. The necessary steps to obtain the physical cross sections from the detector level quantities are explained in this chapter.

## 5.1 Cross section definition

The single differential particle level cross sections $d\sigma/d\tau_1^b(Q^2, y)$ in bins of $Q^2$ and $y$ are measured as

$$\sigma = \frac{N_{\text{data}} - N_{\text{Bkg}}}{L \cdot \Delta_\tau} \cdot c_{\text{unfold}} \cdot c_{\text{QED}} \,, \tag{5.1}$$

where $N_{\text{data}}$ denotes the number of data events in one bin, $N_{\text{Bkg}}$ denotes the estimated number of background events. That is events from processes other than high-$Q^2$ inclusive NC DIS. $\Delta_\tau$ denotes the bin-width in $\tau_1^b$ and the $1/\Delta_\tau$ term accounts for binning effects. The two multiplicative corrections $c_{\text{unfold}}$ and $c_{\text{QED}}$ are obtained from Monte Carlo studies with the event generators Djangoh and Rapgap. $c_{\text{unfold}}$ is the detector-correction factor, $c_{\text{QED}}$ denotes the corrections for electron QED radiative effects. The procedure to obtain the corrections is explained in the following two sections.

## 5.2 Detector corrections

For the transition from the data taken on detector level to the physical particle level the multiplicative detector corrections $c_{\text{unfold}}$ are applied to each measurement bin. This bin-by-bin correction method is denoted as unfolding. The goal of unfolding is to construct estimators for the "true" particle level distribution. This step corrects for detector specific resolution and acceptance effects. The corrections are obtained by dividing the particle level cross section $\sigma_{\text{part}}$ by the detector level cross section $\sigma_{\text{det}}$. To obtain the bin-by-bin correction factors the average of the two MC models Rapgap and Djangoh is calculated. The factors correspond to the inverse of the acceptance defined in the previous chapter

$$c_{\text{unfold}} = \frac{\sigma_{\text{part}}}{\sigma_{\text{det}}} = \frac{1}{A}. \tag{5.2}$$

This unfolding method introduces a bias which often tends to pull the estimators towards the model predictions. The systematic uncertainty arising from the bias can be roughly estimated by comparing the correction factors obtained from different MC models [115,116]. Since the two independent MC event generators Rapgap and Djangoh produce almost identical values for the acceptance (cf. figure 4.8), and therefore for $c_{\text{unfold}}$, the error is small. It will not be taken into account when deriving the systematical uncertainties in section 5.4.

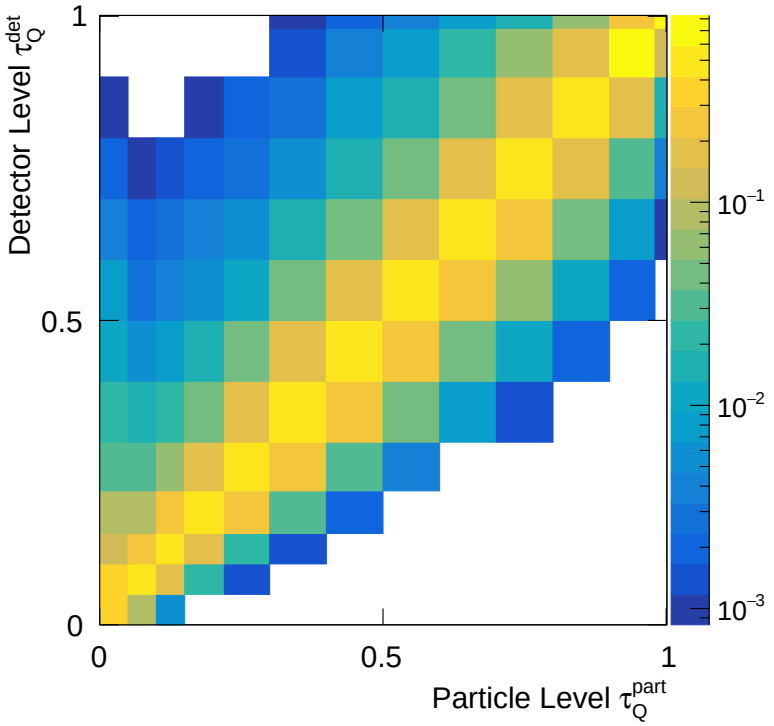


Figure 5.1: Normalised migration matrix of the DIS thrust $\tau_Q$. The matrix is shown for the Djangoh event generator. The matrix is normalised to the detector level $\tau_Q^{det}$.

The normalised migration matrix is shown in figure 5.1. The detector level thrust $\tau_Q^{\text{det}}$ is plotted against the particle level $\tau_Q^{\text{part}}$ for the Djangoh MC model. The matrix is normalised to the $\tau_Q^{\text{det}}$ distribution, so one column of the matrix adds up to one. Since the DIS thrust is defined to be strictly in the range between 0 and 1, overflow bins are not necessary. Most events are located on the diagonal of the matrix. These events are generated and, after the detector simulation, reconstructed in the same bin. The diagonal elements of the matrix correspond to the purity $P$ defined in equation (4.2). The limited resolution of the detector causes a smearing and as a consequence entries in the off-diagonal elements. They are distributed evenly around the diagonal. The second feature one can observe in the migration matrix is a shift towards higher $\tau_Q^{\text{det}}$ values. Recalling the definition of the DIS thrust as one minus the sum over all particles in the current hemisphere, it is clear that this shift is caused by missing particles in the detector. Since the diagonal elements dominate the matrix, the applied bin-by-bin unfolding method is well justified.

## 5.3 QED corrections

The cross sections are presented on non-radiative particle level. The definition of the non-radiative particle level corresponds to a pure $\gamma$, $Z$ or $\gamma/Z$ born-level cross section, with the exception that higher-order QED corrections like real or virtual corrections at the lepton vertex are excluded. For the transition from the measured data to the radiative particle level, the detector corrections were applied. To obtain non-radiative cross sections, corrections for electron QED effects need to be applied according to equation (5.1). The Feynman diagrams of the QED subprocesses that will be corrected for are depicted in figure 5.2.

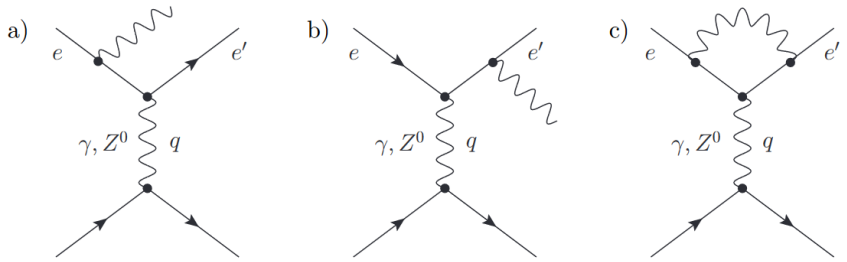


Figure 5.2: Feynman diagrams of LO QED processes. The diagrams (a), (b) and (c) will be taken into account when correction for electron QED radiative effects. Figure adapted from [108]

The corrections include real emission of photons (a,b) and vertex corrections (c). Initial state radiation (ISR) describes process (a) where a photon is emitted before the electron interacts with the parton. Process (b) is called final state radiation (FSR).
Three cases how to treat QED radiation are defined on particle level. To measure the distance between electron and photon the angular distance $R^2 = \Delta\varphi^2 + \Delta\eta^2$ is defined. If the distance between FSR photon and electron is smaller than $R = 0.15 \approx 5^{\circ}$, the particles are recombined by adding up both four-vectors. If the angular distance is larger than $R = 0.15$, the photon is treated as a particle of the hadronic final state. ISR photons are neglected entirely. They are radiated mostly along the beam axis and can not be measured in the detector. Therefore, they are not taken into account on particle level as well. This scenario with three different cases for the treatment of electron QED radiation matches with the detector level. One can now obtain the radiative corrections by dividing the non-radiative particle level cross section by the radiative particle level cross section

$$c_{\mathrm{QED}} = \frac{\sigma_{\mathrm{norad}}}{\sigma_{\mathrm{rad}}} \tag{5.3}$$

The non-radiative MC samples were produced independently of the radiative level MCs. The size of the corrections depends on the reconstruction method. It is desirable to get small corrections, which corresponds to $c_{\mathrm{QED}} \approx 1$. Similar to section 5.2, the IΣ reconstruction method will be compared to the eΣ method.
Figure 5.3 presents the QED corrections obtained with the IΣ method. Djangoh and Rapgap behave similarly over the entire phase space. According to the definition of the IΣ method in table 3.1, the kinematic reconstruction is based on quantities of the hadron final state only. The effect of QED processes on the reconstruction is therefore expected to be small.

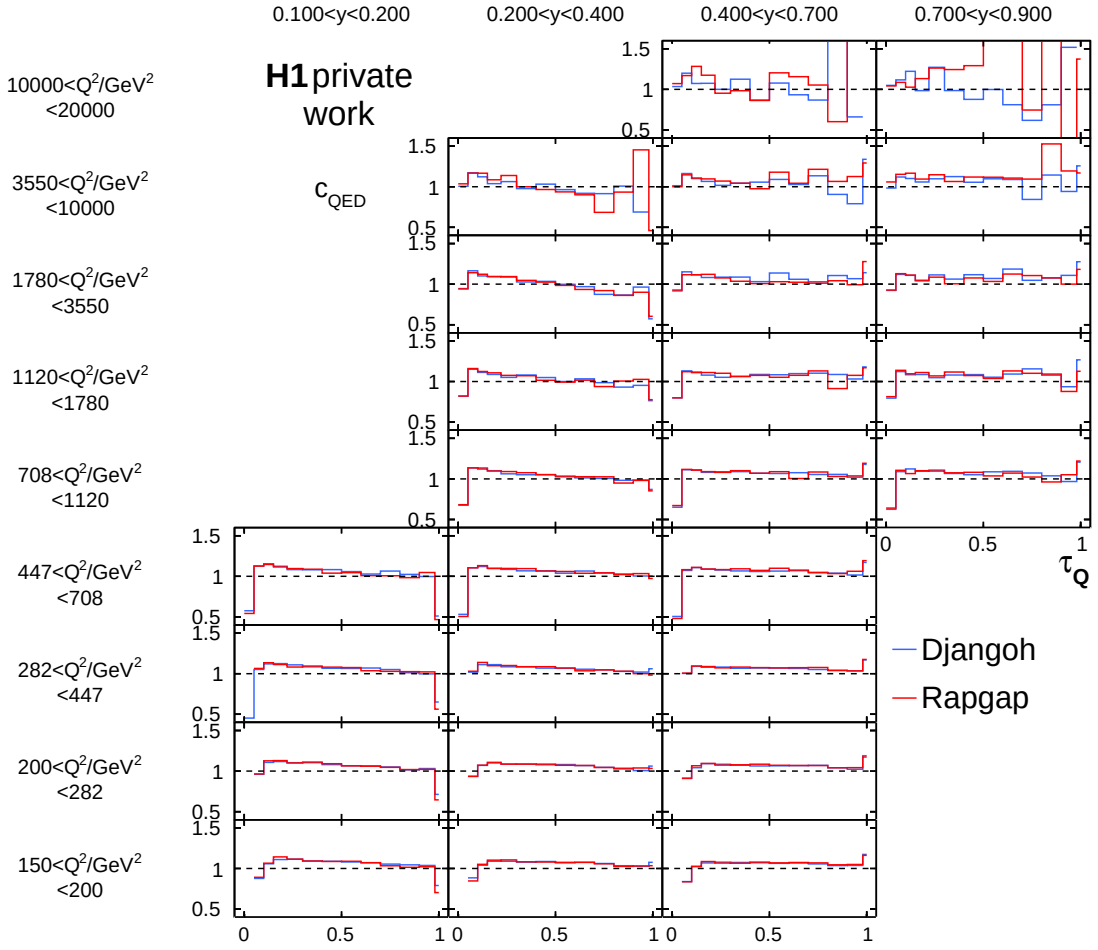


Figure 5.3: QED corrections $c_{\mathrm{QED}}$ defined in equation (5.3) are presented for Rapgap and Djangoh. The IΣ method is used for the reconstruction of the events.

The corrections in the first bins $0.0 < \tau_Q < 0.05$ are sizable and get as large as almost 50 %. In the other bins the distribution is flat with corrections around 5 %. At highest $Q^2$ the $c_{\mathrm{QED}}$ start to fluctuate due to the low statistics in those bins. The impact of those fluctuations on the measurement is negligible, since the statistics of the data is too low to measure properly, as will be seen in chapter 5.

As a comparison, the eΣ factors are displayed in figure 5.4. The IΣ and eΣ method are compared to find the reconstruction methods with the smallest QED corrections, while still achieving the highest resolution. At low $Q^2$, the $c_{\mathrm{QED}}$ are almost exactly 1. Only at $\tau_Q \to 0$ are the corrections increasing. At high $Q^2$, fluctuations start to occur similarly to the IΣ result. At high $Q^2$ - medium $y$ the corrections can be up to 40 %.

Both reconstruction methods produce small QED corrections. According to section 4.3 the IΣ method achieved higher purities. Concluding from the results of this section and section 4.3, the IΣ method will be used for correcting the data.

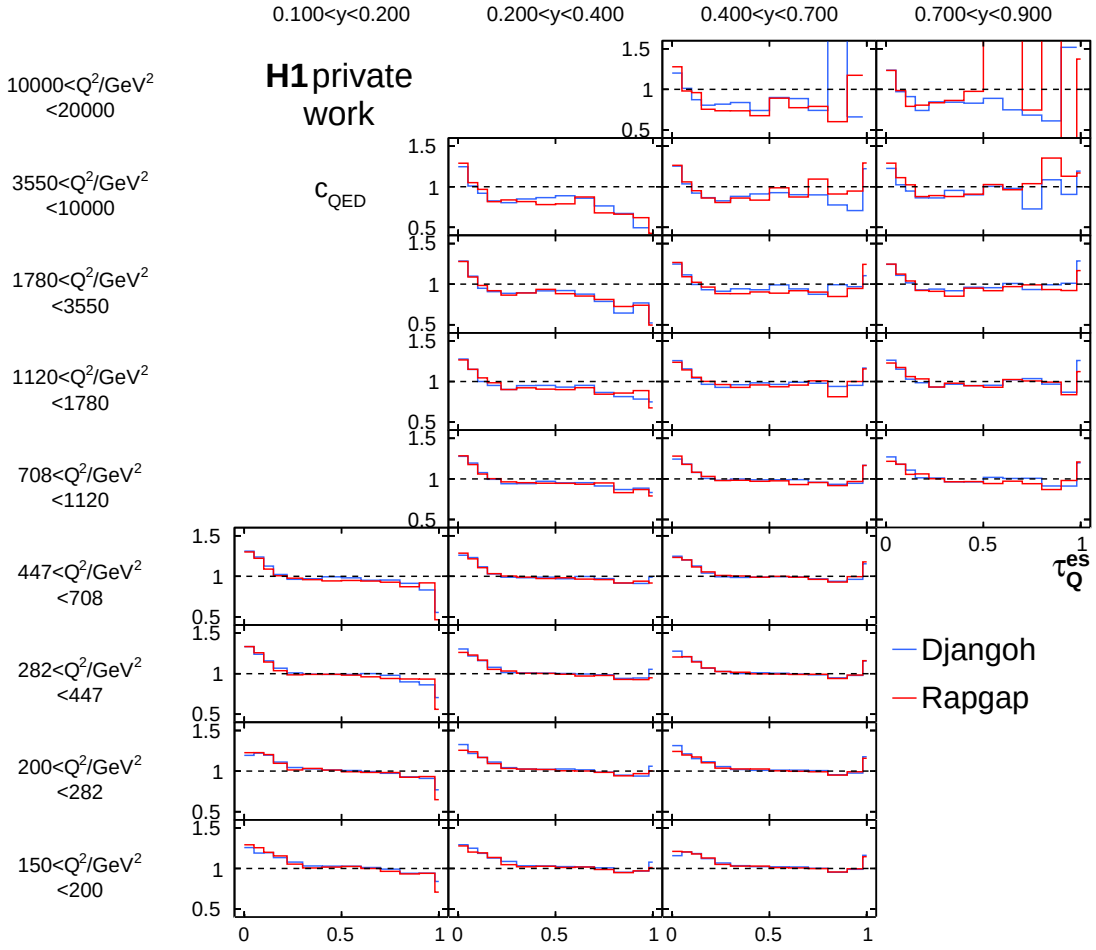


Figure 5.4: Similar to figure 5.3. The correction factors for higher-order QED effects obtained when using the eΣ reconstruction method.

## 5.4 Systematical and statistical uncertainties

Fluctuations in the data sample give rise to an uncertainty, associated with the statistical uncertainty $\delta^{\text{stat}}$. For the measurement the number of events in the single bins is counted. The distribution of the events is described by a Poisson distribution. The standard deviation of a Poisson distribution is given by the square root of the number of entries $\sqrt{N}$. The relative uncertainty due to statistical fluctuations is given by

$$\delta^{\text{stat}} = \frac{\sqrt{N}}{N} = \frac{1}{\sqrt{N}}. \tag{5.4}$$

The statistical uncertainty is found to be small in most bins. At very high $Q^2$ the uncertainty increases. Bins with less than 3 events will be disregarded. This corresponds to an uncertainty of $\delta^{\text{stat}} \approx 60$ %.
To obtain the systematical uncertainties a linear propagation of errors is assumed. By systematical variation of a single quantity measured within the experiment, the uncertainties can be estimated. The quantity is shifted upward by the systematic uncertainty for all affected particles. This shift is then included in the kinematic event reconstruction and finally propagated to the cross sections. The relative shift in the cross section $\sigma_i$ with respect to the nominal cross section $\sigma_{\text{nom}}$ corresponds to the systematical uncertainty of error source $i$

$$\delta_i^{\text{sys}} = \frac{\sigma_{\text{nom}} - \sigma_i}{\sigma_{\text{nom}}} \tag{5.5}$$

The quadratic sum of the individual components gives the systematical uncertainty. There are five major uncertainty sources which will be taken into account. They are summarised in table 5.1 The particles in the HFS are separated into particles that are clustered into jets and

| Source | JES | RCES | $E_{e'}$ | $\vartheta_{e'}$ | $\vartheta_{\text{HFS}}$ | Lumi |
|---|---|---|---|---|---|---|
| $\delta^{\text{sys}}$ | 1% | 1% | 0.5% | 1 mrad | 1 mrad | 2.7% |

Table 5.1: Error sources and associated uncertainties taken into account for the analysis.

particles that remain unclustered. These two particle classes are also distinguished in the error analysis. The differentiation follows directly from the jet-energy calibration [79, 108] which supplies all tracks and clusters with the final calibration factors. The two independent uncertainty contributions are denoted jet energy scale (JES) uncertainty and remaining cluster energy scale (RCES) uncertainty. The JES affects high-energy objects, while the RCES affects low-$p_T$ objects. Both uncertainties are obtained by varying the energy of the affected HFS objects by 1 %.
The energy resolution of the scattered lepton depends on the detector region where it is reconstructed. In the central and the backward region an uncertainty of 0.5 % is assigned. In the forward region the uncertainty is slightly larger at 1 % [117].
The LAr was installed with a precision of 1 mrad in the polar angle with respect to the central tracking detector [117]. The effect of the uncertainty component is considered separately for the scattered electron and the HFS particles.
The largest uncertainty arises from the integrated luminosity. It is associated with an uncertainty of 2.7 % [64].

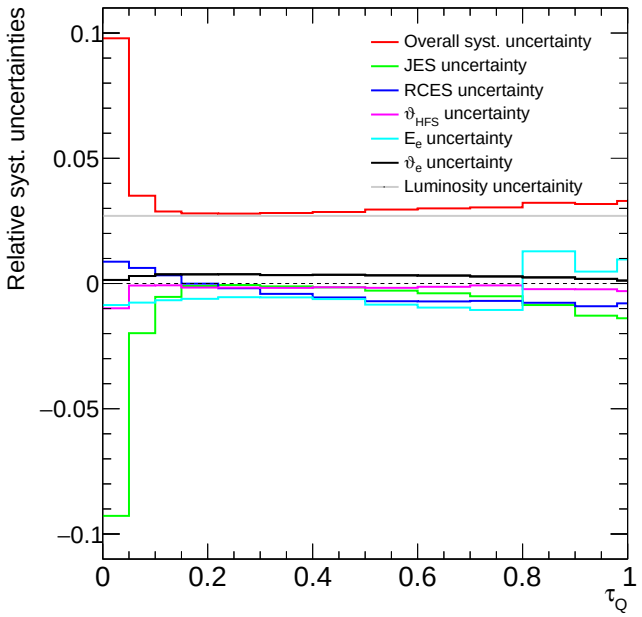


Figure 5.5: Systematical uncertainty on the cross section as a function of $\tau_Q$. The systematical uncertainty is defined as the relative change in the cross section after varying a single quantity within the measurement according to equation (5.5). The total uncertainty is given by the quadratic sum of the single components.

The systematic uncertainties for each bin of the single differential cross section measurement are displayed in figure 5.5. At smallest $\tau_Q$ the uncertainty arising from the JES is dominatig at $\delta^{\text{sys}}_{\text{JES}} \approx 9$ %. In all other bins the systematical error is dominated by the luminosity uncertainty and is around 3 %.
The total systematic uncertainties for the measurement in bins of $\tau_Q$, $Q^2$ and $y$ are shown in the plot 7.4. They are small over the entire phase space.

# Chapter 6

# Measurement of classical event shape observables

In this chapter, the results of the analysis of HERA-II data are benchmarked against previous measurements done with HERA-I data [34, 118]. The observables thrust $\tau_z$, jet mass $\rho$, jet broadening $B$ and $C$-parameter were defined in the equations (2.18)-(2.21). Only particles in the current hemisphere of the Breit frame contribute to the observables. A requirement on the minimal energy in the current hemisphere is imposed (cf. eq. (2.22)) to ensure infrared and collinear safety.

## 6.1 Event shape observable control plots

To compare the results of this analysis to the previous results, the phase space of the HERA-I analyses is adapted. It is confined by $0.1 < y < 0.7$ and $196 < Q^2 < 40000$ GeV$^2$. The detector level distributions of the four event shape observables thrust $\tau_z$, jet mass $\rho$, jet broadening $B$ and $C$-parameter are displayed in figure 6.1. The data are compared to the Rapgap and Djangoh MC models. The contribution from background processes is small.
The $\tau_z$ distribution on the top left exhibits a distinct peak at $\tau_z \approx 0.2$ and declines towards $\tau_z \to 1$. The distribution has a great similarity to the $\tau_Q$ distribution in figure 4.7. However, due to the requirement of a minimal energy in the current hemisphere the $\tau_z$ distribution does not exhibit a second peak at high values of $\tau_z$. Djangoh performs well in describing the shape of the distribution, the ratio to the data is flat but slightly too low. Rapgap describes the peak region well but underestimates the high $\tau_z$ region.
The jet mass shown on the top right possesses a similar shape as the thrust. The distribution is limited by $\rho < 0.25$. The $\rho > 0.1$ region is reasonably well described by Rapgap, while Djangoh underestimates the medium $\rho$ range.
The bottom row displays the jet broadening $B$ and the $C$-parameter plots. The first peak in the $B$ distribution at $B \approx 0.2$ is underestimated by Djangoh. The second peak at $B \approx 0.5$ on the other hand is underestimated by Rapgap. It consists of dijet events and is well described by Djangoh. The first bin of the $C$-parameter distribution is populated by events where only one particle candidate is reconstructed. The sum in the definition of $C$ vanishes and by construction $C = 0$. This effect appears only at detector level. At particle level those events are not present. The distribution is reasonably well described by Rapgap, while Djangoh displays a more distinct shape.

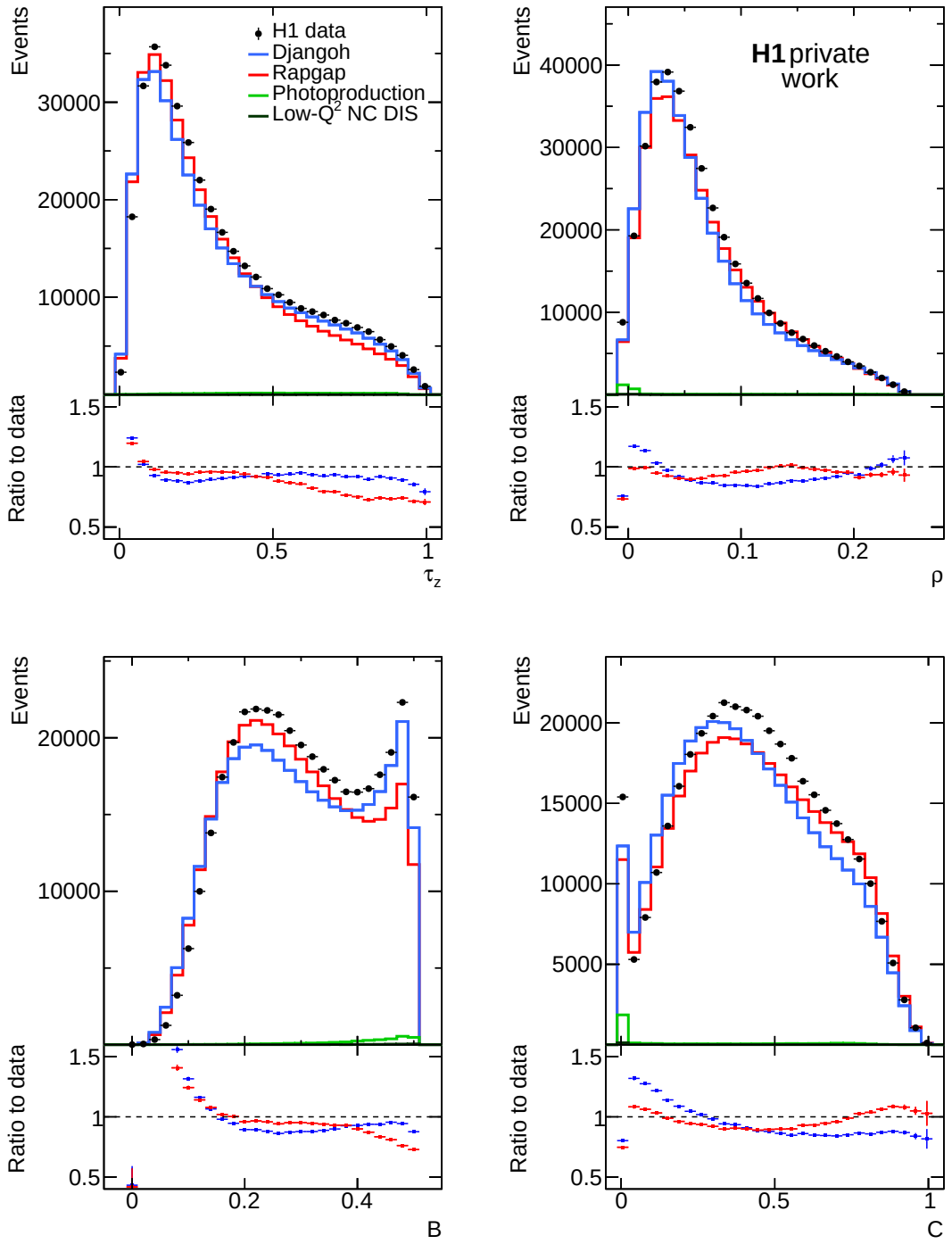


Figure 6.1: Detector level distribution of the event shape observables thrust $\tau_z$, jet mass $\rho$, jet broadening $B$ and $C$-parameter in the phase space region $0.1 < y < 0.7$ and $196 < Q^2 < 40000$ GeV$^2$. The data is compared to the Rapgap and Djangoh signal MC generators. The legend displayed in the top left panel is valid for all four plots.

## 6.2 Normalised cross sections for classical observables

In the previous event shape analyses using HERA-I data, the observables thrust $\tau_c$ and $\tau_z$, the jet mass $\rho$, the jet broadening $B$ and the $C$-parameter were measured in bins of $Q^2$ [34, 118]. The cross sections were normalised to one $Q^2$ bin to reduce the systematic uncertainties.
The measurement was repeated in this thesis to validate the analysis framework. The thrust $\tau_c$ had to be omitted in this new analysis, due to technical difficulties in the algorithm to find the thrust axis $\vec{n}$. The other observables do not make use of such an algorithm. The QED and the detector corrections were obtained from Djangoh and Rapgap with the IΣ reconstruction method. The systematical uncertainties were not evaluated. The $Q^2$ bins differ slightly between the previous and the new analysis. However, since the normalised event shape is compared, instead of absolute cross sections, the difference in the $Q^2$ binning does not have any impact. The previous analysis was conducted with data taken from 1995 to 2000 during the HERA-I period. Therefore, this study does not only validate the workflow of the new analysis, but also compares the two data sets taken in the HERA-I and HERA-II period.

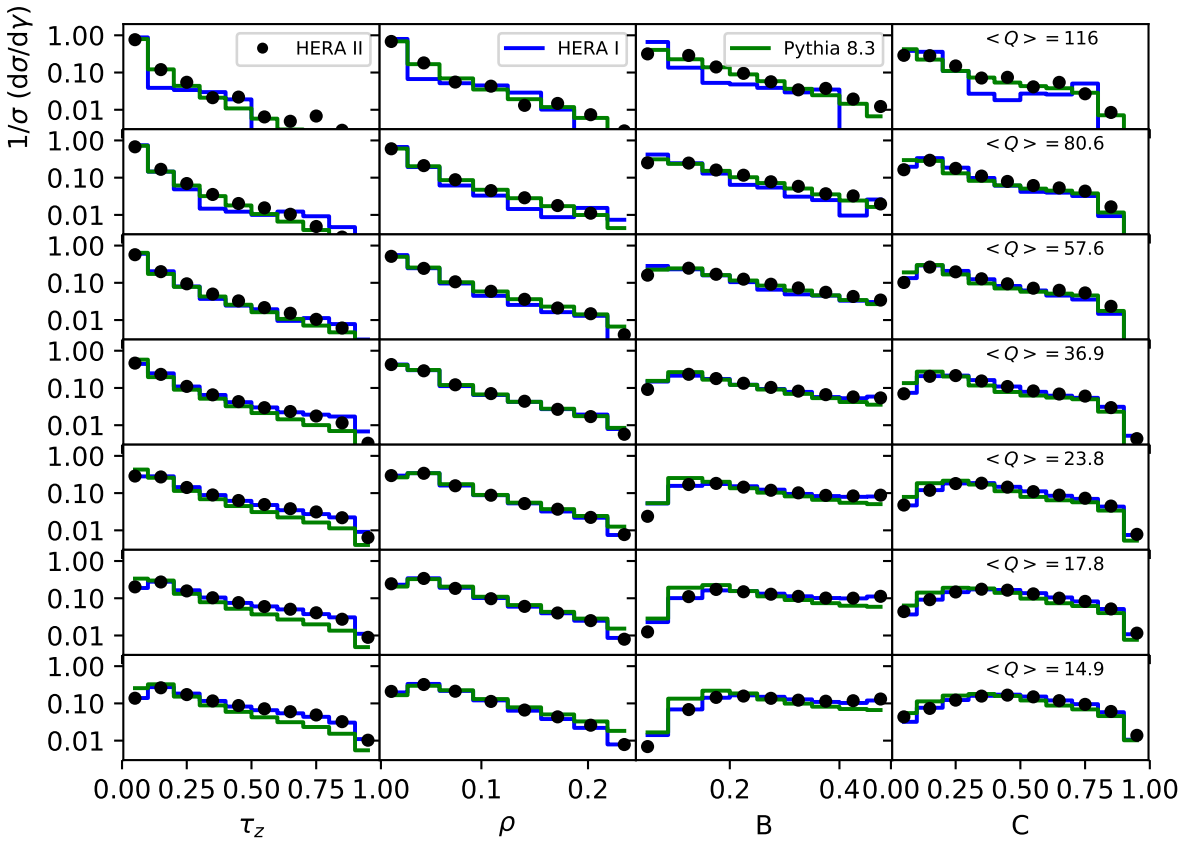


Figure 6.2: Comparison between the H1 analysis [34, 118] denoted with HERA I, the current analysis labelled HERA II and Pythia 8.3 predictions. Each column shows the normalised cross section as a function of an event shape observable $\gamma$, where $\gamma$ can be $\tau_z$, $\rho$, $B$ or $C$. The cross sections are normalised to the integrated cross section in one $Q^2$ bin. The mean $Q$ of the HERA I analysis is indicated in the right column.

The overview plot in figure 6.2 compares the HERA-II data processed in this analysis to previous H1 event shape measurements (denoted with HERA-I) and Pythia 8.3 predictions. The mean $Q$ of one bin in the previous analysis is indicated in the right column. The left column presenting the $\tau_z$ cross sections shows a good agreement between the two measurements. The low $\tau_z$ values are well described by Pythia, while the tail region ($\tau_z > 0.3$) is underestimated. The jet mass $\rho$ is well described by Pythia, HERA-I and HERA-II measurement coincide. Only at highest $Q^2$ some minor discrepancies appear. These discrepancies can be traced back to statistical fluctuations in the data. The results of both measurements match for the jet broadening $B$ and the $C$-parameter in the third and fourth column. Pythia provides a reasonable description. While the low values are slightly overestimated, the normalised cross section for high $B$ and $C$ is a few percent too low.
In appendix B, the results of the triple differential measurement of the four event shape observables is presented. This analysis was able to reproduce the H1 results published in [34, 118]. Pythia 8.3 provides a satisfactory description of the data for all observables and in all $Q^2$ bins. One can conclude, that the analysis framework is set up properly. The procedure to obtain the unfolded cross sections from the data is justified and can be used to measure the 1-jettiness $\tau_1^b$.

# Chapter 7

# The 1-jettiness cross section

In this chapter the results of the single and triple differential cross section measurement are presented [1]. The data are compared to the various theory predictions introduced in section 2.4.

## 7.1 Single differential cross sections

The results for the single differential cross section $d\sigma/d\tau_1^b$ measurement are shown in the figures 7.1 and 7.2. The measurement is conducted in the kinematic region $150 < Q^2 < 20\,000\,\mathrm{GeV}^2$ and $0.2 < y < 0.7$. The variables were reconstructed with the IΣ method. As described in chapter 5, the data are corrected for detector effects and QED radiative effects. The cross sections are presented at the non-radiative particle level. The quadratic sum of systematical and statistical uncertainties (vertical error bars) is smaller than the marker size in most bins. The systematical uncertainties are about 3%. Only in the first bin a larger uncertainty of about 9% can be observed (cf. figure 5.5).
In figure 7.1, the data is compared to the MC event generators Rapgap and Djangoh. These predictions include born-level photon and Z-exchange and the renormalised fine-structure constant, but no other higher-order electroweak effects. It can be observed that the peak region $\tau_1^b < 0.3$ is not well described by either of the models. Rapgap and Djangoh underestimate the data. In the tail region $\tau_1^b > 0.3$ the models bracket the data. Due to its harder spectrum, Django has a slightly higher cross section in that region.
Figure 7.2 compares the data with recent MC models (left) and with fixed order calculations (right). The left plot shows the comparison of Pythia 8.3 with varying parton shower models to the data. The default model [43] is used, as well as Dire [52–54] and Vincia [44–47] . Pythia+Dire and Pythia+Vincia predict too large cross sections in the peak region. In that region, a large dependence on the parton shower model can be observed. This is expected since this region is highly sensitive to resummation and hadronisation effects. In the tail region, all models behave similarly and underestimate the data. Neither model performs exceedingly well over the entire $\tau_1^b$ distribution. However, considering that the models have not been tuned to DIS, the description is still satisfactory.

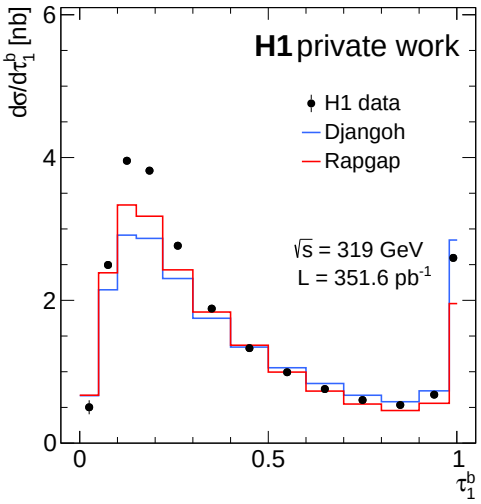


Figure 7.1: The differential cross section $d\sigma/d\tau_1^b$ in the kinematic region $150 < Q^2 < 20\,000\,\mathrm{GeV}^2$ and $0.2 < y < 0.7$. The data are compared to the MC predictions from Djangoh and Rapgap.

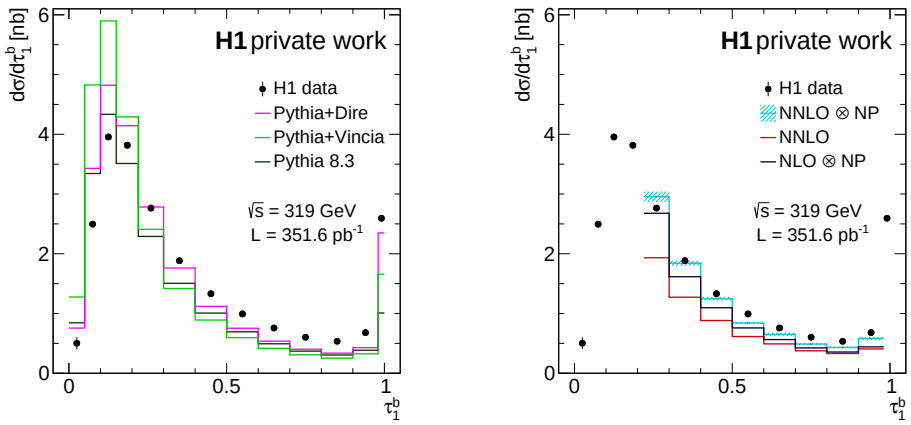


Figure 7.2: The differential cross section $d\sigma/d\tau_1^b$ in the kinematic region $150 < Q^2 < 20\,000\,\mathrm{GeV}^2$ and $0.2 < y < 0.7$. The data are compared to predictions from recent MC generators (left) and to fixed order calculations (right).

Fixed order calculations in next-to-next-to-leading order (NNLO) QCD [119] are being compared to the data in the right panel of figure 7.2. As explained in section 2.4, the fixed order calculations are valid in the tail region. Thus they are displayed for $0.22 < \tau_1^b < 0.98$ only. The shaded area indicates the scale uncertainty. Corrections for hadronisation obtained from Pythia with the default parton shower are applied. The corrections can get sizable when moving towards the peak region. The NNLO calculations are shown with and without hadronisation corrections. An uncertainty on the multiplicative corrections is not considered. The NNLO prediction does a reasonable job at describing the data in the region of validity.

## 7.2 Triple differential cross sections

The differential cross sections $d\sigma/d\tau_1^b$ in adjacent regions of $Q^2$ and $y$ are presented in this section. The cross section will be denoted as triple differential cross section. The plots 7.3, 7.5 and 7.7 display the $\tau_1^b$ distribution for the adjacent phase space regions. The ratios of the various predictions to the data are shown in figures 7.4, 7.6 and 7.8, respectively. The $Q^2$ and $y$ ranges are given on the left and at the top of the plots. Compared to the single differential cross sections, the range in $y$ is extended. Integrating over the $Q^2$ and $y$ bins produces the single differential cross sections presented in the previous section. Integrating over $\tau_1^b$ gives the DIS cross section for the dedicated $Q^2$-$y$ bin.
Figure 7.3 shows the data compared to Rapgap and Djangoh. To study the dependence on $Q^2$, one compares e.g. the nine $Q^2$ bins with $0.5 < y < 0.7$. Moving towards higher $Q^2$ shifts the peak to smaller $\tau_1^b$, while at the same time the tail is lowered. Due to the running of $\alpha_s$, the probability of event configurations with multiple jets decreases with increasing $Q^2$. The effect of hadronisation is further reduced, since the Born level DIS jet has higher momentum. Additionally, at high $Q^2$ the HFS is more collimated which also results in smaller values for $\tau_1^b$. The $\delta$-peak in the last bin ($0.98 < \tau_1^b \leq 1$) is enhanced when $y$ is increased. According to equation (2.8), high $y$ correspond to low $x$ at fixed $Q^2$ and $\sqrt{s}$. Event configurations with empty current hemisphere appear only at $x$ at least smaller than 0.5 [39].
To enable a better comparison of data and predictions, the ratio of the predictions to the data is shown in figure 7.4. The systematic uncertainties are shown as an error band alongside the statistical uncertainties represented by the vertical error bars. The systematic errors are in the order of 5 %. They are dominated by the the luminosity uncertainty. The statistical uncertainties are negligible in the main phase space. Only in the extreme regions at high $Q^2$ and high $y$ can they get sizeable. Bins in the highest $Q^2$ region had to be excluded from the measurement, due to insufficient statistics.
Djangoh and Rapgap provide a reasonable description of the data over the entire phase space. At low $Q^2$ and low $y$, Djangoh describes the tail region best, while Rapgap performs better at low $Q^2$ high $y$. The description of the data is further improved when moving towards larger $Q^2$. In the last $y$ bin ($0.7 < y < 0.9$) neither of the models provide a satisfactory description and the fluctuations increase.
In figure 7.5 the data is compared to modern MC models. That includes Pythia 8.3 with the default parton shower model, as well as the Dire and Vincia parton shower model. Herwig 7.2 predictions are also shown here. The ratio of the various models to the data is shown in figure 7.6. The tail region is simulated similarly by all Pythia implementations. The studied models underestimate the data. In the peak region one can observe larger discrepancies between the models, similar to the single differential results presented in the previous section. Herwig underestimates the peak region in all $Q^2$- $y$ bins. This indicates, that the inclusive DIS cross section is too low. Additionally, at larger $\tau_1^b$ values one can observe a strange structure, which is not understood at this point.
The data are confronted with fixed order predictions in figure 7.7 and 7.8, where the latter shows the ratio of the models to the data. The calculations only describe the tail region, as explained in section 2.4. The non-perturbative corrections accounting for hadronisation can get sizable when the boundary of validity is approached. The corrections were obtained from Pythia 8.3. The scale uncertainties indicated by the blue error band are small almost over the entire phase space. They increase only at the highest $Q^2$. The description of the data improves when moving towards higher $Q^2$.

To summarise, a large kinematic range can be probed in the triple differential cross section measurement. The experimental uncertainties are small in almost every bin. The data were confronted with various models, none of which provides a fully satisfactory description over the entire kinematic range.

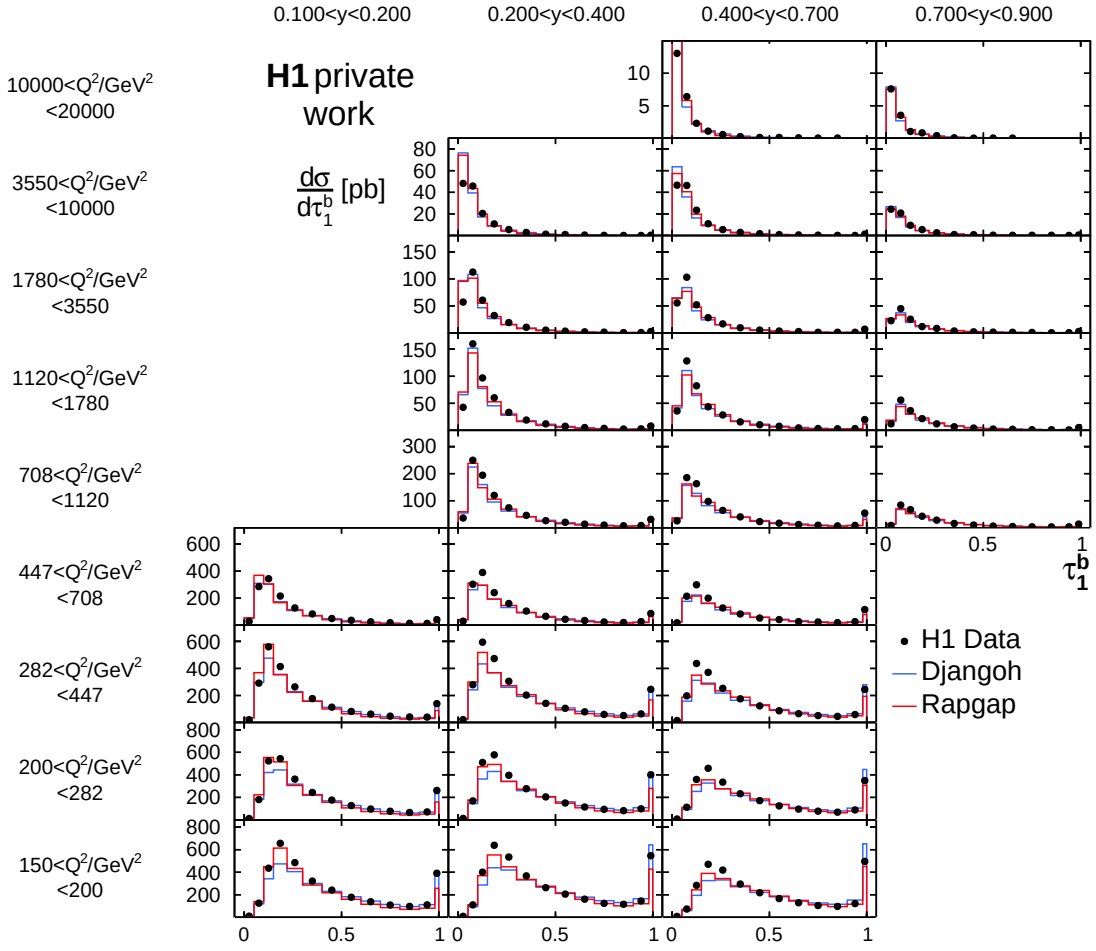


Figure 7.3: The unfolded differential cross section $d\sigma/d\tau_1^b$ for adjacent regions in $Q^2$ and $y$ (also denoted as triple-differential cross sections). Integrating over $\tau_1^b$ in one ($Q^2$,$y$) bin produces the inclusive DIS cross section in that phase space region. The $Q^2$ and $y$ intervals are indicated on the left and top, respectively. The data are compared to predictions from the Djangoh and Rapgap MC event generators.

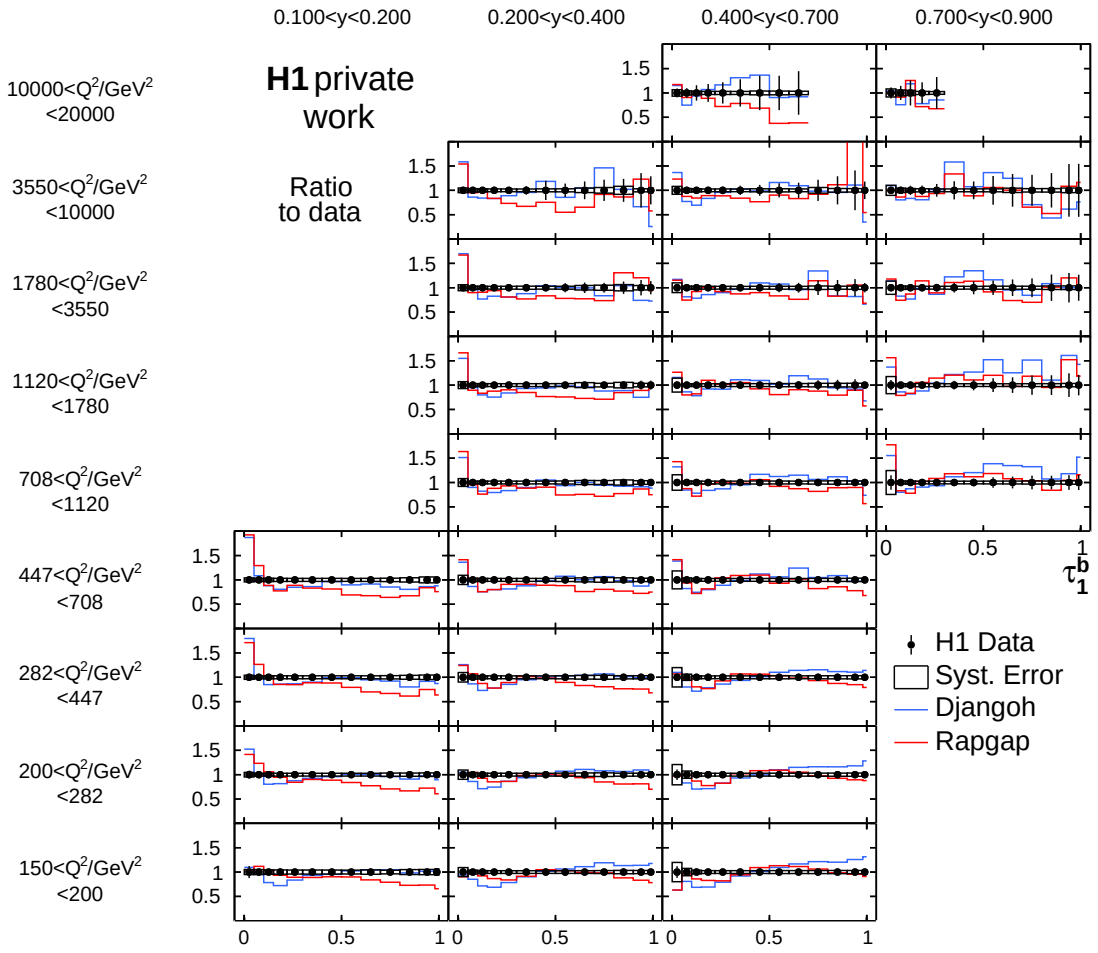


Figure 7.4: The ratio of the Rapgap and Djangoh predictions to the differential cross section $d\sigma/d\tau_1^b$ for adjacent regions in $Q^2$ and $y$ (see caption of fig. 7.3 for more details). The vertical error bars indicate the statistical uncertainties, the systematical uncertainties are represented by the black boxes.

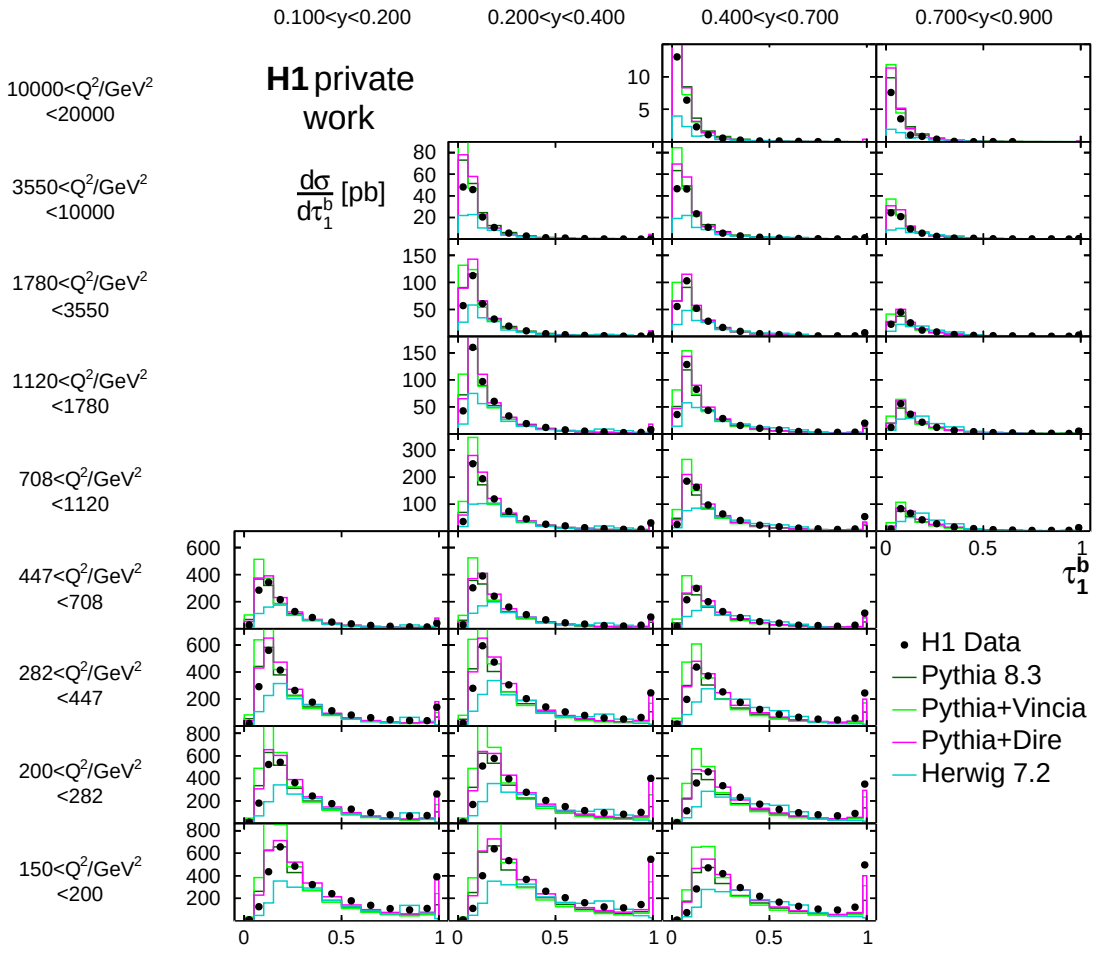


Figure 7.5: Similar as fig. 7.3, but the data are confronted with predictions from recent MC generators Pythia 8.3 and Herwig 7.2. The Pythia predictions were produced with three different settings for the parton shower, the 'default' shower (no label), Vincia or Dire.

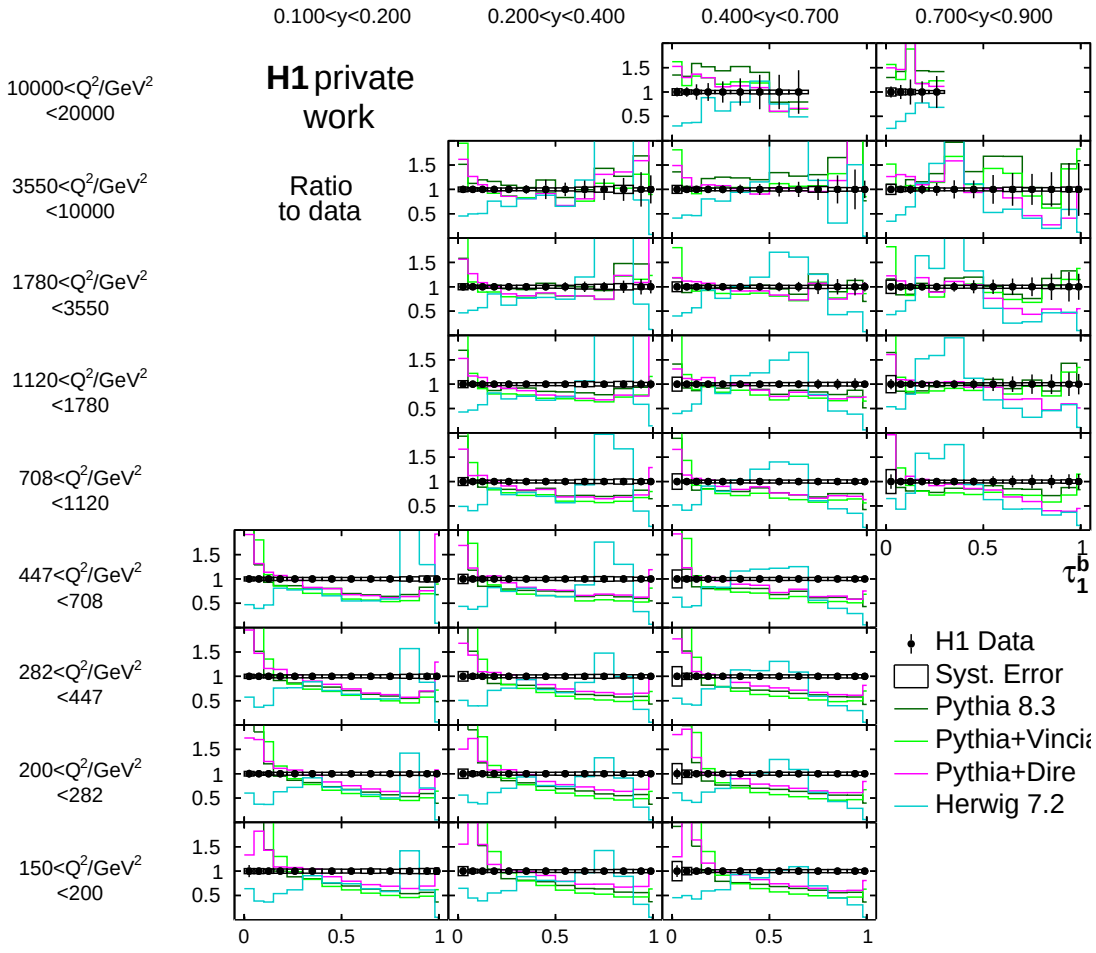


Figure 7.6: The ratio of the Pythia and Herwig predictions as displayed in fig. 7.5) to the cross sections $d\sigma/d\tau_1^b$ (c.f. caption of fig. 7.4).

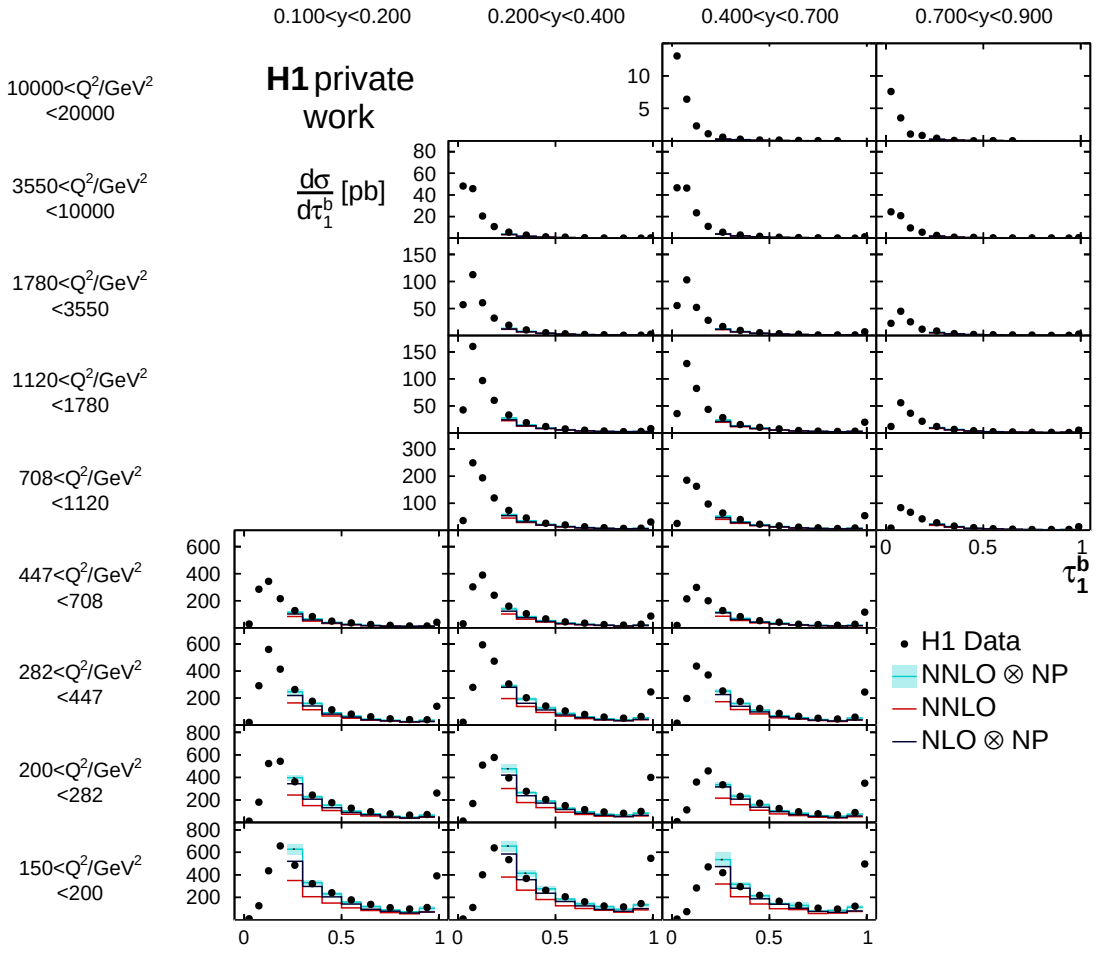


Figure 7.7: Similar as fig. 7.3, but the data are compared to predictions from a fixed order calcuation in next-to-next-to-leading order (NNLO) perturbative QCD of the process $ep \to e + 2\text{jets} + X$. The predictions are presented with and without non-perturbative (NP) corrections to account for hadronisation effects. The corrections were obtained from Pythia 8.3.

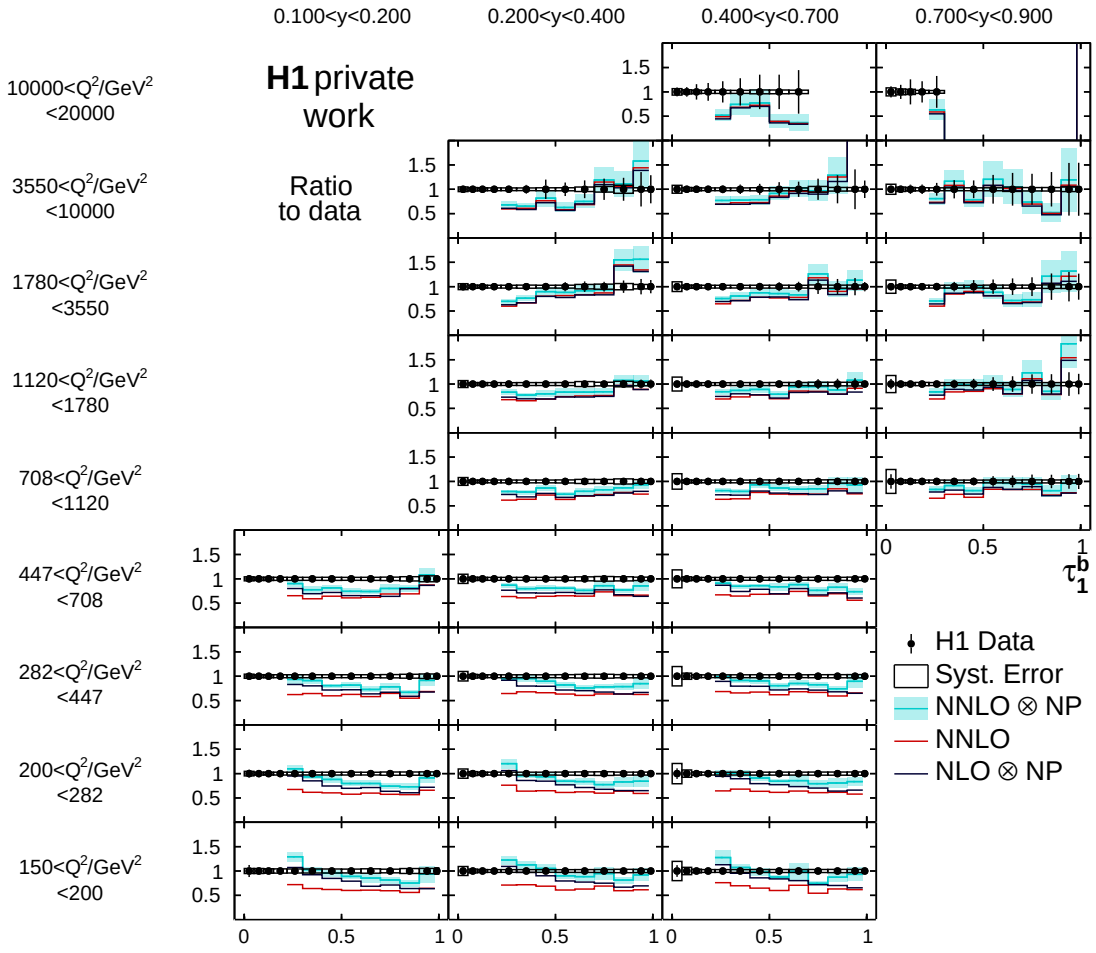


Figure 7.8: The ratio of the fixed order predictions as displayed in fig. 7.7) to the cross sections $d\sigma/d\tau_1^b$ (c.f. caption of fig. 7.4).

# Chapter 8

# Summary and outlook

In this thesis, a detailed study on the measurement of the 1-jettiness event shape observable $\tau_1^b$ in NC DIS was performed. Subsequently, a first measurement of the 1-jettiness cross section is presented [1]. The data were taken with the H1 experiment at the HERA $ep$ collider at DESY. They amount to an integrated luminosity of $L = 351.6\ \mathrm{pb}^{-1}$ at a centre of mass energy of $\sqrt{s} = 319$ GeV. The cross sections are presented as single differential cross sections as a function of $\tau_1^b$ and in a triple differential representation in adjacent regions in $Q^2$ and $y$. The analysis phase space is confined by $150 < Q^2 < 20\,000\,\mathrm{GeV}^2$ and $0.2 < y < 0.7$ or $0.1 < y < 0.9$ for the single and triple differential measurement, respectively. Large parts of the analysis framework were developed within this thesis. Dedicated studies were performed for a detailed understanding of detector acceptance and resolution effects. A focus was on the kinematic reconstruction of single events. The IΣ and eΣ reconstruction methods were compared regarding the obtained purities and QED corrections. While both reconstruction methods delivered similar QED corrections, the IΣ method achieved higher purities. It was therefore used for the event reconstruction. The analysis workflow was benchmarked by successfully reproducing results of earlier H1 event shape measurements. The 1-jettiness $\tau_1^b$ is equivalent to the DIS thrust $\tau_Q$. Therefore, $\tau_1^b$ can be measured as $\tau_Q$. The DIS thrust is preferred experimentally, since particles in the beam hemisphere of the Breit frame can be neglected.
The differential cross sections were presented as a function of the 1-jettiness $\tau_1^b$, the event virtuality $Q^2$ and the inelasticity $y$. The data were compared to selected predictions. The Djangoh and Rapgap MC event generators provided a reasonable description of the data. The Pythia 8.3 predictions were combined with three different parton shower models. The peak region which is sensitive to resummation and hadronisation effects can not be described by the models to full satisfaction. All models underestimate the tail region. Fixed order calculations obtained from NNLOJET for the process $ep \to e + 2\mathrm{jets} + X$ are also confronted with the data. In the region of validity, they provide a reasonable description of the data.
A statistically more rigorous unfolding e.g. with the TUnfold [120] package is left for subsequent analyses. The approach to apply an unbinned unfolding using the tool of neural networks can also be explored [121,122]. The measurement will become valuable for improving multi-purpose MC event generators. The sensitivity to the strong coupling constant $\alpha_\mathrm{s}$ and to the PDFs of the proton will be explored.

# Appendix A

# Cross section tables for the 1-jettiness

The measurement results of the differential cross section $d\sigma/d\tau_1^b$ in adjacent ($Q^2$,$y$) bins is presented in the tables A.1 and A.2. The $Q^2$ and $y$ range is given in the first and second column, respectively. The $\tau_1^b$ interval is indicated in the first line. For each data point the differential cross section in pb is given along with the statistical and systematical uncertainties in percent. The systematical uncertainty includes the luminosity error of 2.7%. To obtain the uncertainty $\delta^{\text{sys}}_{\text{new}}$ without the 2.7%, one can subtract it from the total uncertainty

$$\delta^{\text{sys}}_{\text{new}} = \sqrt{\delta^{\text{sys }2} - \delta^{\text{sys }2}_{\text{lumi}}}.$$

In order to obtain normalised $\tau_1^b$ cross sections, one needs to sum over the 13 $\tau_1^b$ bins in one $(Q^2, y)$ bin. This gives the inclusive DIS cross section which can be used to normalise the distribution in the bin.

| | | $\tau_1^b \in [0.0, 0.05]$ | | | $\tau_1^b \in [0.05, 0.1]$ | | | $\tau_1^b \in [0.1, 0.15]$ | | | $\tau_1^b \in [0.15, 0.22]$ | | | $\tau_1^b \in [0.22, 0.3]$ | | | $\tau_1^b \in [0.3, 0.4]$ | | | $\tau_1^b \in [0.4, 0.5]$ | | |
|---|---|---|---|---|---|---|---|---|---|---|---|---|---|---|---|---|---|---|---|---|---|---|
| $Q^2$ [GeV$^2$] | $y$ | $d\sigma/d\tau$[pb] | $\delta^{\text{stat}}$[%] | $\delta^{\text{sys}}$[%] | $d\sigma/d\tau$[pb] | $\delta^{\text{stat}}$[%] | $\delta^{\text{sys}}$[%] | $d\sigma/d\tau$[pb] | $\delta^{\text{stat}}$[%] | $\delta^{\text{sys}}$[%] | $d\sigma/d\tau$[pb] | $\delta^{\text{stat}}$[%] | $\delta^{\text{sys}}$[%] | $d\sigma/d\tau$[pb] | $\delta^{\text{stat}}$[%] | $\delta^{\text{sys}}$[%] | $d\sigma/d\tau$[pb] | $\delta^{\text{stat}}$[%] | $\delta^{\text{sys}}$[%] | $d\sigma/d\tau$[pb] | $\delta^{\text{stat}}$[%] | $\delta^{\text{sys}}$[%] |
| [10000, 20000] | [0.4, 0.7] | 13.07 | 9.14 | 6.63 | 6.408 | 9.76 | 4.29 | 2.295 | 15.81 | 3.61 | 1.086 | 18.26 | 3.12 | 0.5616 | 21.82 | 3.21 | 0.2524 | 28.01 | 3.10 | 0.1227 | 35.36 | 3.91 |
| [10000, 20000] | [0.7, 0.9] | 7.590 | 11.38 | 8.24 | 3.529 | 14.50 | 6.03 | 1.038 | 25.73 | 5.33 | 0.8262 | 21.82 | 3.18 | 0.3964 | 32.71 | 2.80 | - | | | - | | |
| [3550, 10000] | [0.2, 0.4] | 48.21 | 5.70 | 4.81 | 45.80 | 4.02 | 3.51 | 20.48 | 5.47 | 3.02 | 10.78 | 5.95 | 2.90 | 5.607 | 7.62 | 2.82 | 2.899 | 8.98 | 2.74 | 1.307 | 19.89 | 3.04 |
| [3550, 10000] | [0.4, 0.7] | 46.59 | 4.78 | 8.11 | 46.34 | 3.97 | 3.73 | 23.46 | 5.35 | 3.26 | 10.95 | 6.46 | 2.81 | 5.528 | 8.15 | 2.88 | 2.987 | 9.62 | 2.79 | 1.786 | 11.18 | 3.14 |
| [3550, 10000] | [0.7, 0.9] | 24.38 | 6.59 | 10.33 | 20.82 | 6.51 | 4.59 | 9.487 | 9.48 | 3.70 | 5.525 | 9.72 | 3.17 | 2.609 | 13.1 | 2.97 | 0.9781 | 18.71 | 2.86 | 0.8251 | 18.22 | 2.99 |
| [1780, 3550] | [0.2, 0.4] | 57.12 | 5.56 | 6.08 | 112.6 | 3.08 | 3.33 | 60.69 | 3.73 | 3.01 | 32.31 | 4.18 | 2.85 | 19.26 | 4.96 | 2.92 | 10.52 | 5.73 | 3.19 | 5.298 | 7.88 | 2.91 |
| [1780, 3550] | [0.4, 0.7] | 55.5 | 4.79 | 9.97 | 103.0 | 3.15 | 3.34 | 52.11 | 4.26 | 3.20 | 28.28 | 4.87 | 2.89 | 16.82 | 5.80 | 2.85 | 9.614 | 6.56 | 2.76 | 5.386 | 7.98 | 2.96 |
| [1780, 3550] | [0.7, 0.9] | 22.70 | 6.95 | 13.6 | 44.96 | 4.96 | 3.53 | 25.42 | 6.40 | 3.21 | 11.84 | 7.39 | 2.95 | 8.477 | 8.00 | 2.86 | 3.693 | 9.81 | 3.00 | 2.110 | 13.40 | 2.81 |
| [1120, 1780] | [0.2, 0.4] | 42.60 | 5.56 | 7.10 | 159.9 | 2.57 | 3.06 | 96.89 | 2.86 | 2.96 | 60.26 | 3.03 | 2.95 | 33.32 | 3.73 | 2.85 | 19.11 | 4.36 | 2.98 | 12.00 | 5.28 | 2.99 |
| [1120, 1780] | [0.4, 0.7] | 35.85 | 5.88 | 14.29 | 128.4 | 3.15 | 2.87 | 82.38 | 3.51 | 2.80 | 43.56 | 4.08 | 2.82 | 28.48 | 4.70 | 2.77 | 15.63 | 5.47 | 3.02 | 10.41 | 6.38 | 3.01 |
| [1120, 1780] | [0.7, 0.9] | 12.07 | 10.54 | 17.56 | 55.89 | 5.27 | 3.02 | 36.50 | 6.15 | 2.82 | 21.66 | 6.52 | 3.32 | 12.04 | 7.55 | 3.02 | 6.671 | 8.83 | 2.75 | 4.236 | 10.73 | 2.78 |
| [708, 1120] | [0.2, 0.4] | 36.13 | 5.77 | 8.00 | 249.7 | 2.18 | 2.91 | 194.2 | 2.15 | 2.93 | 119.8 | 2.23 | 2.87 | 73.90 | 2.64 | 2.87 | 45.82 | 2.97 | 2.86 | 26.25 | 3.85 | 2.86 |
| [708, 1120] | [0.4, 0.7] | 25.53 | 6.15 | 15.87 | 185.3 | 2.48 | 3.24 | 162.9 | 2.51 | 2.81 | 97.42 | 2.71 | 2.76 | 64.22 | 3.15 | 2.81 | 40.24 | 3.51 | 2.81 | 22.76 | 4.42 | 3.11 |
| [708, 1120] | [0.7, 0.9] | 8.573 | 14.85 | 24.54 | 83.94 | 5.15 | 3.10 | 66.95 | 5.47 | 3.11 | 42.56 | 5.51 | 2.76 | 28.15 | 6.10 | 2.81 | 15.87 | 6.93 | 2.74 | 10.14 | 8.23 | 2.75 |
| [447, 708] | [0.1, 0.2] | 28.00 | 6.57 | 4.15 | 284.8 | 2.14 | 3.40 | 343.3 | 1.71 | 3.38 | 215.1 | 1.59 | 3.20 | 127.3 | 1.86 | 3.12 | 82.96 | 2.02 | 3.08 | 49.10 | 2.55 | 3.19 |
| [447, 708] | [0.2, 0.4] | 29.40 | 5.97 | 9.43 | 302.4 | 1.99 | 3.52 | 389.5 | 1.62 | 3.07 | 240.4 | 1.60 | 2.99 | 160.0 | 1.89 | 2.98 | 104.0 | 2.03 | 3.04 | 65.81 | 2.52 | 2.97 |
| [447, 708] | [0.4, 0.7] | 17.58 | 7.13 | 18.40 | 213.9 | 2.33 | 4.16 | 298.4 | 2.00 | 2.80 | 199.7 | 1.97 | 2.78 | 127.1 | 2.31 | 2.82 | 82.64 | 2.54 | 2.88 | 52.52 | 3.19 | 2.88 |
| [282, 447] | [0.1, 0.2] | 20.53 | 6.85 | 4.22 | 291.4 | 1.94 | 3.12 | 560.1 | 1.38 | 3.13 | 414.0 | 1.19 | 3.06 | 263.7 | 1.30 | 3.05 | 176.8 | 1.41 | 3.03 | 113.6 | 1.76 | 2.99 |
| [282, 447] | [0.2, 0.4] | 21.46 | 6.11 | 9.75 | 279.5 | 1.84 | 3.87 | 594.0 | 1.31 | 2.99 | 473.1 | 1.14 | 2.97 | 304.9 | 1.28 | 2.93 | 202.8 | 1.42 | 3.00 | 141.7 | 1.70 | 2.93 |
| [282, 447] | [0.4, 0.7] | 14.75 | 7.66 | 19.88 | 197.4 | 2.33 | 6.33 | 436.4 | 1.69 | 3.08 | 371.0 | 1.50 | 2.83 | 253.0 | 1.67 | 2.85 | 175.5 | 1.80 | 2.91 | 123.2 | 2.10 | 3.01 |

Table A.1: Table containing the differential cross sections as a function of $\tau_1^b$, $Q^2$ and $y$. The $Q^2$ and $y$ intervals are given on the right. The columns list the cross sections of one $\tau_1^b$ bin up to $\tau_1^b < 0.5$. The column lists the cross section $d\sigma/d\tau_1^b$ in the dedicated bin in units of pb, as well as the statistical and systematical uncertainties in percent.

| | | $\tau_1^b \in [0.5, 0.6]$ | | | $\tau_1^b \in [0.6, 0.7]$ | | | $\tau_1^b \in [0.7, 0.8]$ | | | $\tau_1^b \in [0.8, 0.9]$ | | | $\tau_1^b \in [0.9, 0.98]$ | | | $\tau_1^b \in [0.98, 1.0]$ | | |
|---|---|---|---|---|---|---|---|---|---|---|---|---|---|---|---|---|---|---|---|
| $Q^2$ [GeV$^2$] | $y$ | $d\sigma/d\tau$[pb] | $\delta^{\text{stat}}$[%] | $\delta^{\text{sys}}$[%] | $d\sigma/d\tau$[pb] | $\delta^{\text{stat}}$[%] | $\delta^{\text{sys}}$[%] | $d\sigma/d\tau$[pb] | $\delta^{\text{stat}}$[%] | $\delta^{\text{sys}}$[%] | $d\sigma/d\tau$[pb] | $\delta^{\text{stat}}$[%] | $\delta^{\text{sys}}$[%] | $d\sigma/d\tau$[pb] | $\delta^{\text{stat}}$[%] | $\delta^{\text{sys}}$[%] | $d\sigma/d\tau$[pb] | $\delta^{\text{stat}}$[%] | $\delta^{\text{sys}}$[%] |
| [10000, 20000] | [0.4, 0.7] | 0.1193 | 35.36 | 3.84 | 0.06134 | 44.72 | 3.52 | - | | | - | | | - | | | - | | |
| [10000, 20000] | [0.7, 0.9] | - | | | - | | | - | | | - | | | - | | | - | | |
| [3550, 10000] | [0.2, 0.4] | 1.026 | 13.87 | 3.11 | 0.5116 | 18.26 | 4.61 | 0.2076 | 21.82 | 5.76 | 0.1441 | 23.57 | 8.25 | 0.1022 | 35.36 | 3.14 | 0.3334 | 28.87 | 5.16 |
| [3550, 10000] | [0.4, 0.7] | 0.9203 | 14.59 | 3.22 | 0.5989 | 15.63 | 2.85 | 0.3966 | 21.79 | 5.80 | 0.2269 | 28.87 | 3.73 | 0.1261 | 40.82 | 3.55 | 1.337 | 17.96 | 3.60 |
| [3550, 10000] | [0.7, 0.9] | 0.3992 | 29.51 | 3.06 | 0.2697 | 33.60 | 4.42 | 0.2942 | 31.83 | 3.47 | 0.3006 | 35.36 | 3.57 | 0.1527 | 54.09 | 4.73 | 0.5213 | 54.44 | 4.22 |
| [1780, 3550] | [0.2, 0.4] | 3.393 | 9.37 | 3.01 | 2.157 | 10.72 | 4.59 | 1.584 | 10.00 | 5.21 | 0.703 | 12.70 | 6.41 | 0.8232 | 15.81 | 4.50 | 2.732 | 13.61 | 4.07 |
| [1780, 3550] | [0.4, 0.7] | 3.597 | 9.22 | 3.00 | 2.653 | 10.03 | 2.87 | 1.234 | 14.96 | 3.57 | 1.331 | 15.81 | 3.10 | 1.298 | 17.68 | 3.29 | 7.051 | 9.54 | 3.16 |
| [1780, 3550] | [0.7, 0.9] | 1.612 | 14.74 | 3.16 | 1.301 | 16.95 | 3.12 | 0.9954 | 19.24 | 3.12 | 0.5151 | 27.11 | 3.63 | 0.5671 | 30.27 | 3.74 | 2.724 | 26.73 | 4.07 |
| [1120, 1780] | [0.2, 0.4] | 7.539 | 7.44 | 3.08 | 5.204 | 7.26 | 5.09 | 3.759 | 7.05 | 3.69 | 2.488 | 8.05 | 5.64 | 2.865 | 9.09 | 3.55 | 8.073 | 9.28 | 3.47 |
| [1120, 1780] | [0.4, 0.7] | 7.604 | 6.84 | 3.22 | 4.568 | 8.35 | 3.21 | 3.436 | 10 | 3.64 | 2.921 | 10.93 | 3.65 | 3.277 | 12.04 | 3.79 | 19.92 | 6.85 | 3.34 |
| [1120, 1780] | [0.7, 0.9] | 2.436 | 14.08 | 2.8 | 2.022 | 16.02 | 2.73 | 1.219 | 19.93 | 2.94 | 1.206 | 20.27 | 2.98 | 0.9494 | 24.28 | 3.41 | 5.214 | 21.00 | 3.33 |
| [708, 1120] | [0.2, 0.4] | 20.20 | 4.59 | 3.13 | 13.46 | 5.36 | 4.18 | 9.970 | 5.47 | 3.99 | 7.400 | 5.23 | 5.27 | 8.223 | 6.09 | 3.72 | 31.14 | 4.77 | 3.52 |
| [708, 1120] | [0.4, 0.7] | 16.88 | 4.81 | 2.98 | 12.04 | 5.32 | 2.88 | 9.426 | 6.09 | 3.23 | 6.970 | 7.37 | 3.45 | 8.789 | 7.51 | 3.27 | 54.36 | 4.80 | 3.44 |
| [708, 1120] | [0.7, 0.9] | 6.230 | 10.77 | 2.87 | 4.609 | 12.13 | 2.96 | 3.391 | 14.11 | 3.21 | 3.389 | 13.81 | 3.02 | 3.606 | 15.01 | 3.50 | 13.63 | 15.51 | 4.06 |
| [447, 708] | [0.1, 0.2] | 36.01 | 2.90 | 3.04 | 24.59 | 3.35 | 3.16 | 18.23 | 3.86 | 3.50 | 13.69 | 3.55 | 4.37 | 13.15 | 3.55 | 6.03 | 40.76 | 3.77 | 4.22 |
| [447, 708] | [0.2, 0.4] | 43.56 | 3.05 | 3.33 | 34.25 | 3.31 | 4.09 | 23.65 | 3.58 | 4.77 | 19.87 | 3.73 | 4.26 | 26.28 | 3.61 | 3.45 | 86.24 | 2.85 | 3.22 |
| [447, 708] | [0.4, 0.7] | 41.28 | 3.33 | 3.10 | 26.22 | 3.99 | 2.85 | 23.65 | 4.42 | 3.09 | 18.74 | 4.71 | 3.15 | 26.07 | 4.62 | 3.49 | 115.4 | 3.64 | 3.50 |
| [282, 447] | [0.1, 0.2] | 81.89 | 2.01 | 3.04 | 62.34 | 2.24 | 3.04 | 47.29 | 2.47 | 3.36 | 41.29 | 2.35 | 3.98 | 40.09 | 2.40 | 4.62 | 139.7 | 2.31 | 3.81 |
| [282, 447] | [0.2, 0.4] | 105.2 | 1.94 | 3.17 | 79.34 | 2.16 | 3.77 | 60.04 | 2.30 | 3.99 | 51.83 | 2.33 | 3.26 | 64.06 | 2.62 | 3.22 | 245.6 | 1.73 | 3.06 |
| [282, 447] | [0.4, 0.7] | 87.14 | 2.35 | 3.12 | 65.55 | 2.61 | 2.96 | 51.42 | 2.95 | 3.11 | 45.50 | 3.12 | 3.20 | 59.07 | 3.10 | 3.33 | 244.7 | 2.65 | 3.69 |
| [200, 282] | [0.1, 0.2] | 127.4 | 1.71 | 2.90 | 96.83 | 1.90 | 2.82 | 77.10 | 2.10 | 3.32 | 66.13 | 2.05 | 3.33 | 71.02 | 1.96 | 3.57 | 261.6 | 1.91 | 3.58 |
| [200, 282] | [0.2, 0.4] | 150.0 | 1.68 | 3.13 | 114.6 | 1.85 | 3.53 | 94.07 | 1.92 | 3.73 | 82.23 | 1.97 | 3.09 | 98.68 | 2.07 | 3.05 | 400.2 | 1.63 | 3.50 |
| [200, 282] | [0.4, 0.7] | 124.7 | 2.01 | 3.04 | 95.96 | 2.23 | 3.03 | 77.79 | 2.43 | 3.18 | 68.81 | 2.59 | 3.22 | 88.78 | 2.57 | 3.35 | 349.3 | 2.32 | 3.63 |
| [150, 200] | [0.1, 0.2] | 178.0 | 2.09 | 3.92 | 138.1 | 2.38 | 4.51 | 108.9 | 2.64 | 3.74 | 97.07 | 2.58 | 5.04 | 110.3 | 2.48 | 5.33 | 391.0 | 2.84 | 6.46 |
| [150, 200] | [0.2, 0.4] | 205.6 | 1.56 | 2.75 | 161.0 | 1.75 | 2.86 | 123.9 | 1.91 | 3.03 | 115.7 | 1.88 | 3.43 | 145.0 | 1.94 | 3.25 | 546.5 | 1.82 | 4.16 |
| [150, 200] | [0.4, 0.7] | 166.2 | 1.82 | 3.06 | 129.3 | 2.04 | 3.01 | 104.7 | 2.24 | 3.12 | 96.49 | 2.33 | 3.27 | 121.8 | 2.36 | 3.21 | 496.5 | 2.08 | 3.64 |

Table A.2: Same as table A.1 but for the 1-jettiness range $0.5 < \tau_1^b < 1.0$.

# Appendix B

# Classical event shape cross sections

The triple differential cross section measurement of the classical event shape observables thrust $\tau_z$, jet mass $\rho$, jet broadening $B$ and $C$-parameter are presented in the figures B.1 to B.8. The plots show the differential cross sections or the ratio of the predictions to the data in bins of $Q^2$ and $y$. The data are confronted with predictions from the MC models Djangoh 1.4, Rapgap 3.1 and Pythia 8.3. To obtain the normalised cross sections presented in figure 6.2, one needs to integrate over the $y$ range $0.1 < y < 0.7$ and normalise to the total cross section of the dedicated $Q^2$ bin. Since the $Q^2$ binning of the previous analysis does not coincide with the new analysis, the $Q^2$ bins $150 < Q^2 < 200$ GeV$^2$ and $708 < Q^2 < 1120$ GeV$^2$ were omitted for the comparison in figure 6.2.

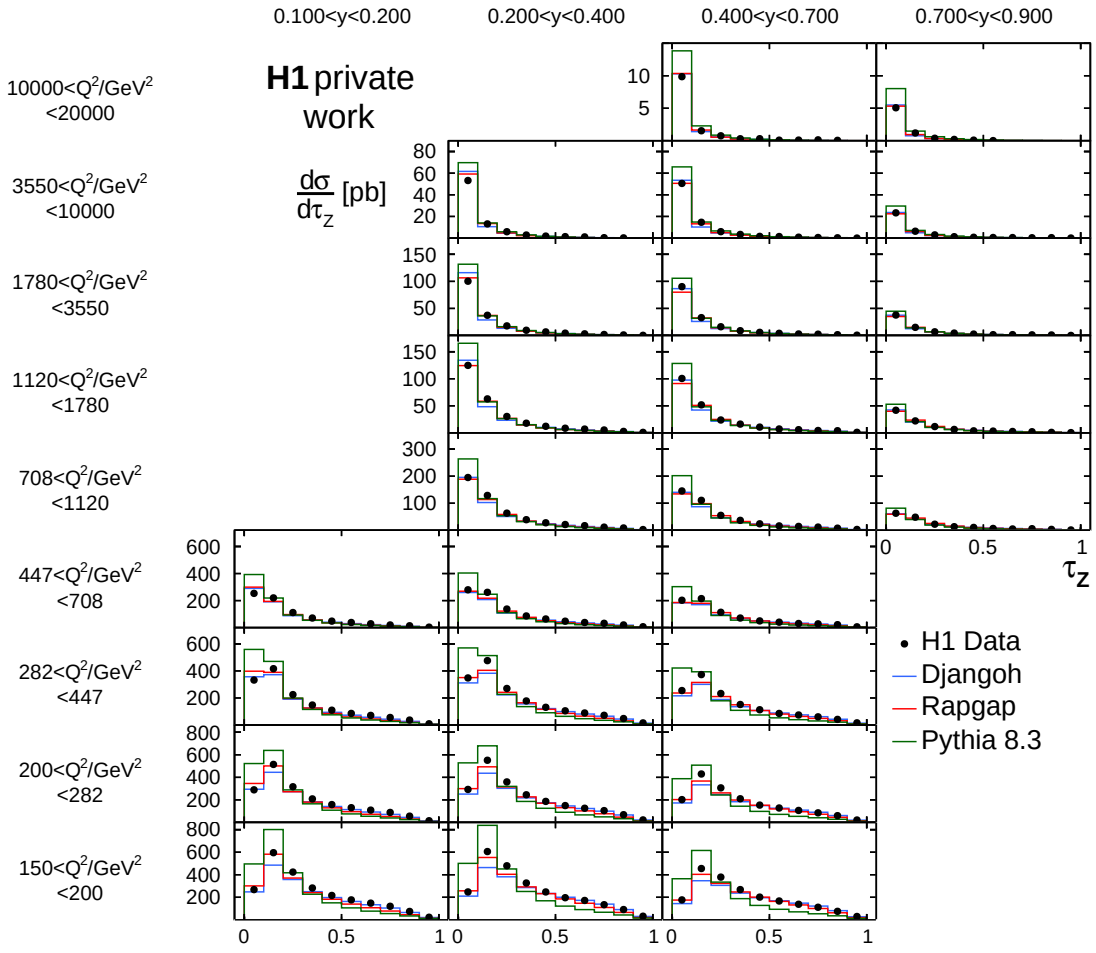


Figure B.1: Differential cross section $d\sigma/d\tau_z$ in bins of $Q^2$ and $y$. The thrust observable $\tau_z$ was defined in eq. (2.18). The data are compared to the Ragpag and Djangoh MC, as well as to Pythia 8.3 predictions.

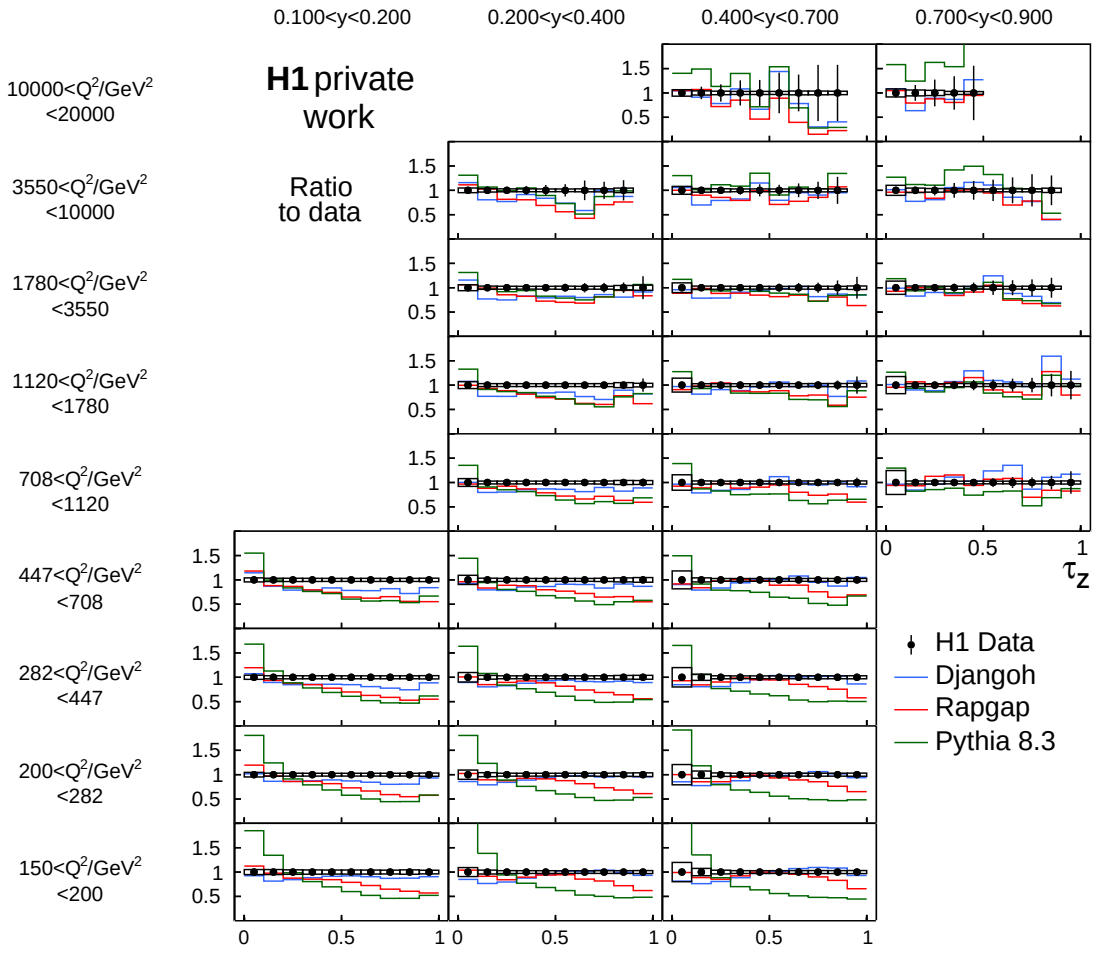


Figure B.2: Ratio of the MC models as in figure B.1 to the measured cross section.

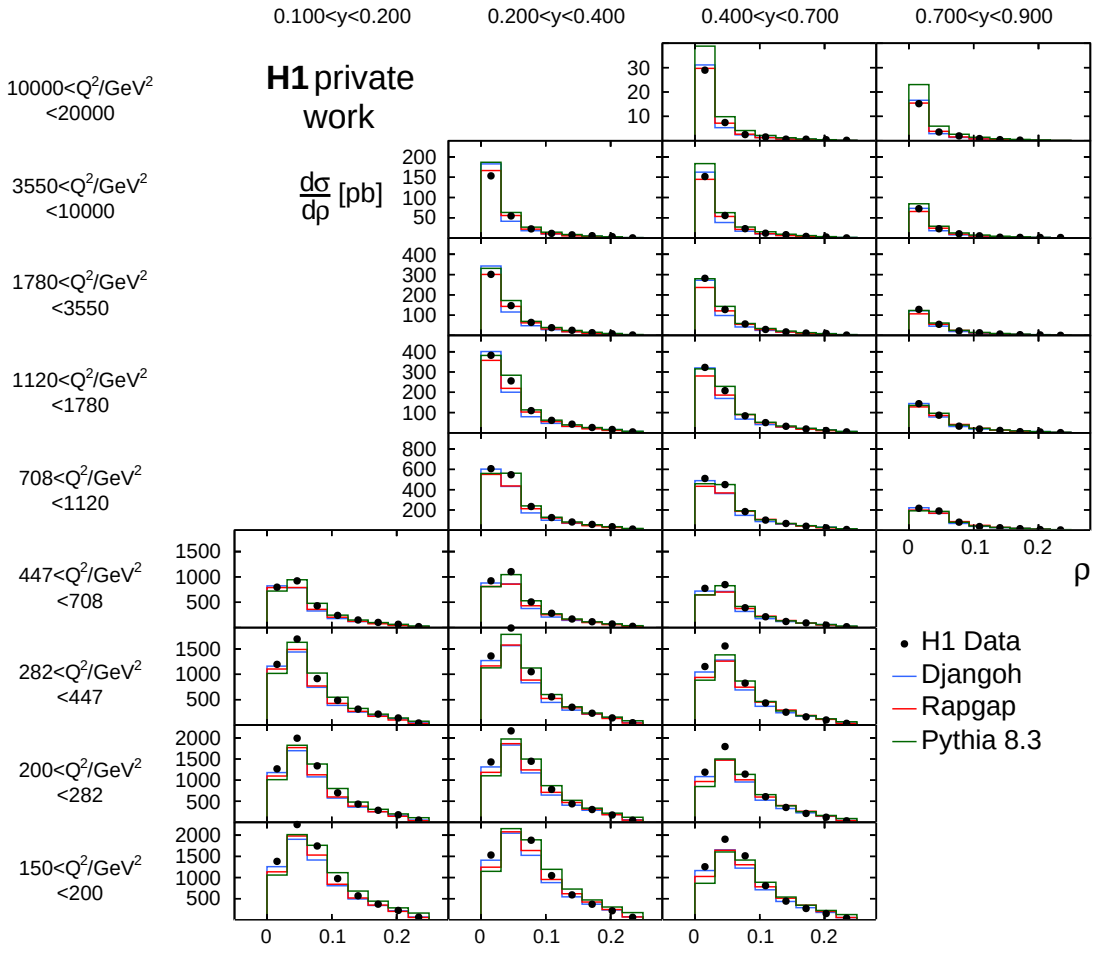


Figure B.3: Differential cross section $d\sigma/d\rho$ in bins of $Q^2$ and $y$. The jet mass $\rho$ was defined in eq. (2.19). The data are compared to the Ragpag and Djangoh MC, as well as to Pythia 8.3 predictions.

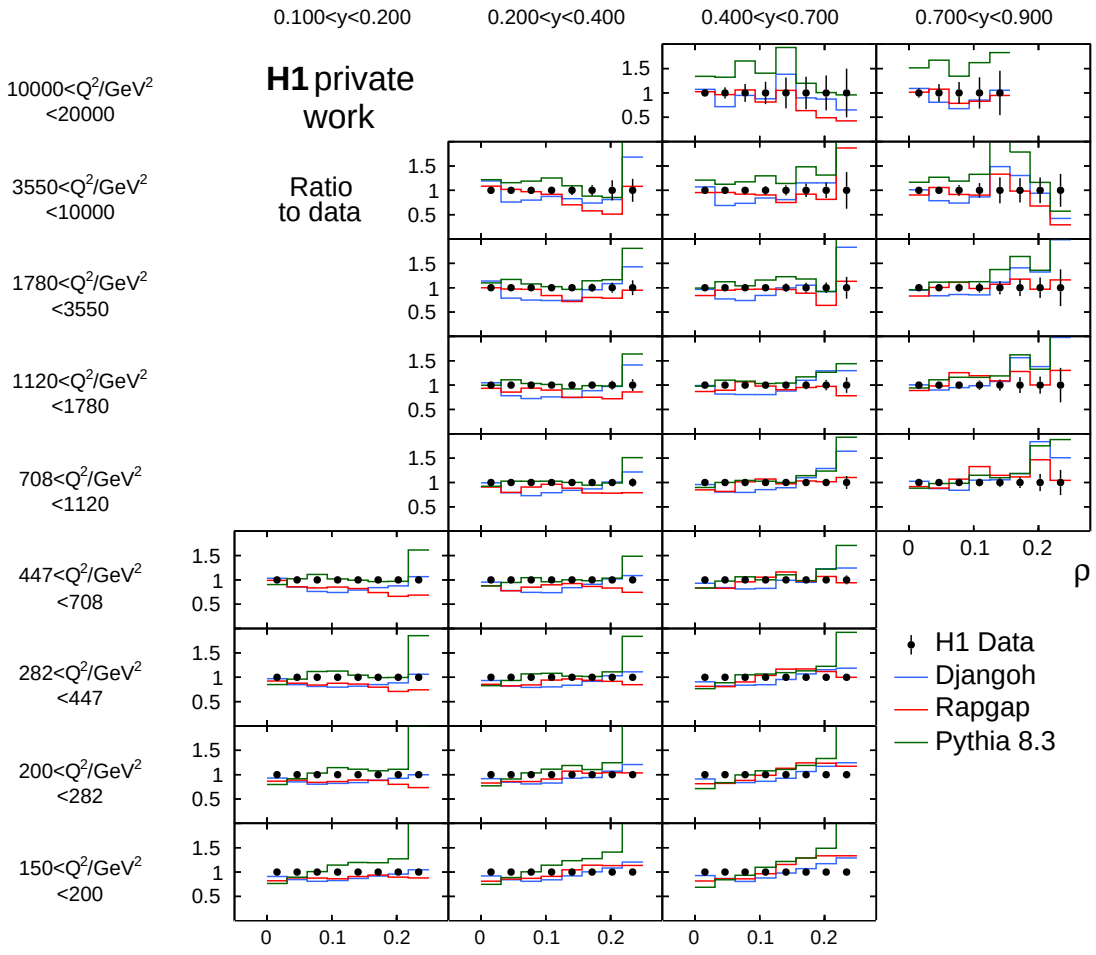


Figure B.4: Ratio of the MC models as in figure B.3 to the measured cross sections.

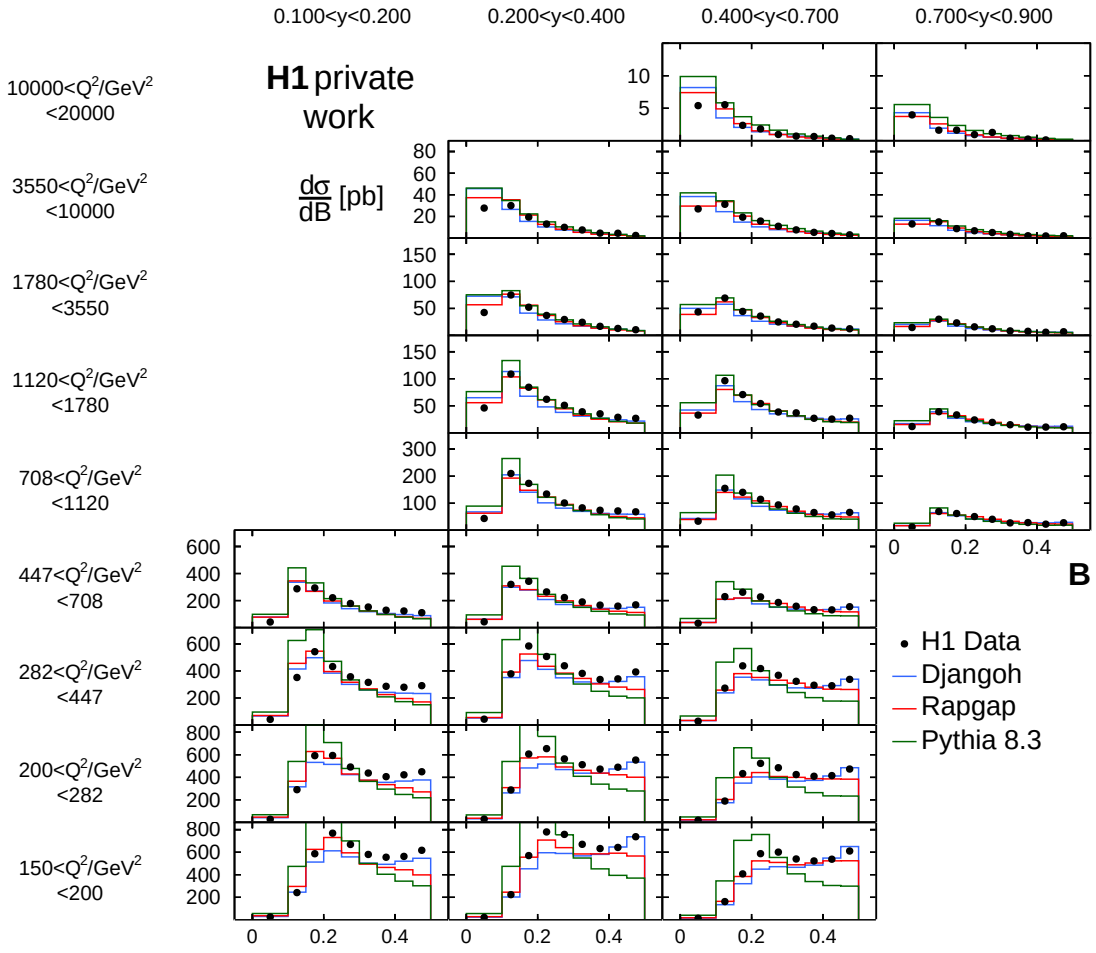


Figure B.5: Differential cross section $d\sigma/dB$ in bins of $Q^2$ and $y$. The jet broadening $B$ was defined in eq. (2.20). The data are compared to the Ragpag and Djangoh MC, as well as to Pythia 8.3 predictions.

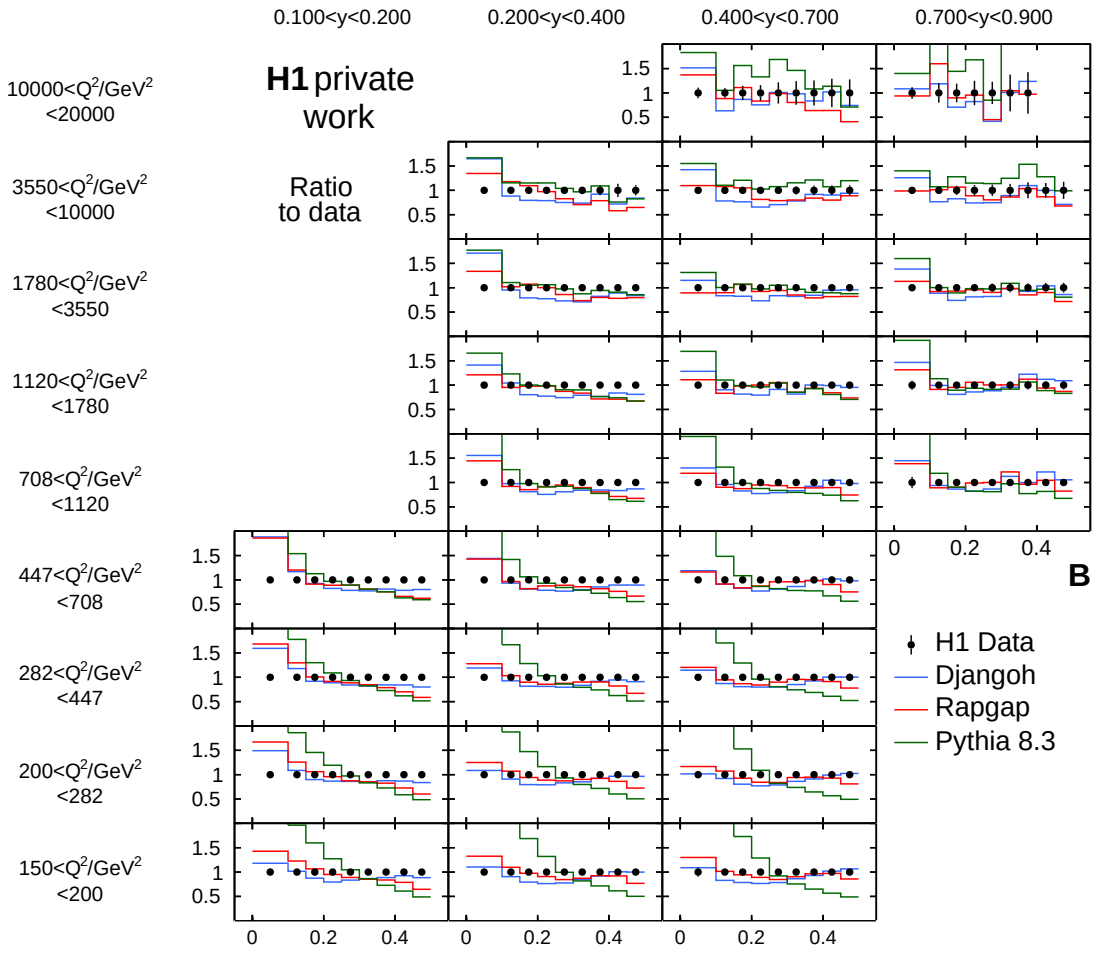


Figure B.6: Ratio of the MC models as in figure B.5 to the measured cross section.

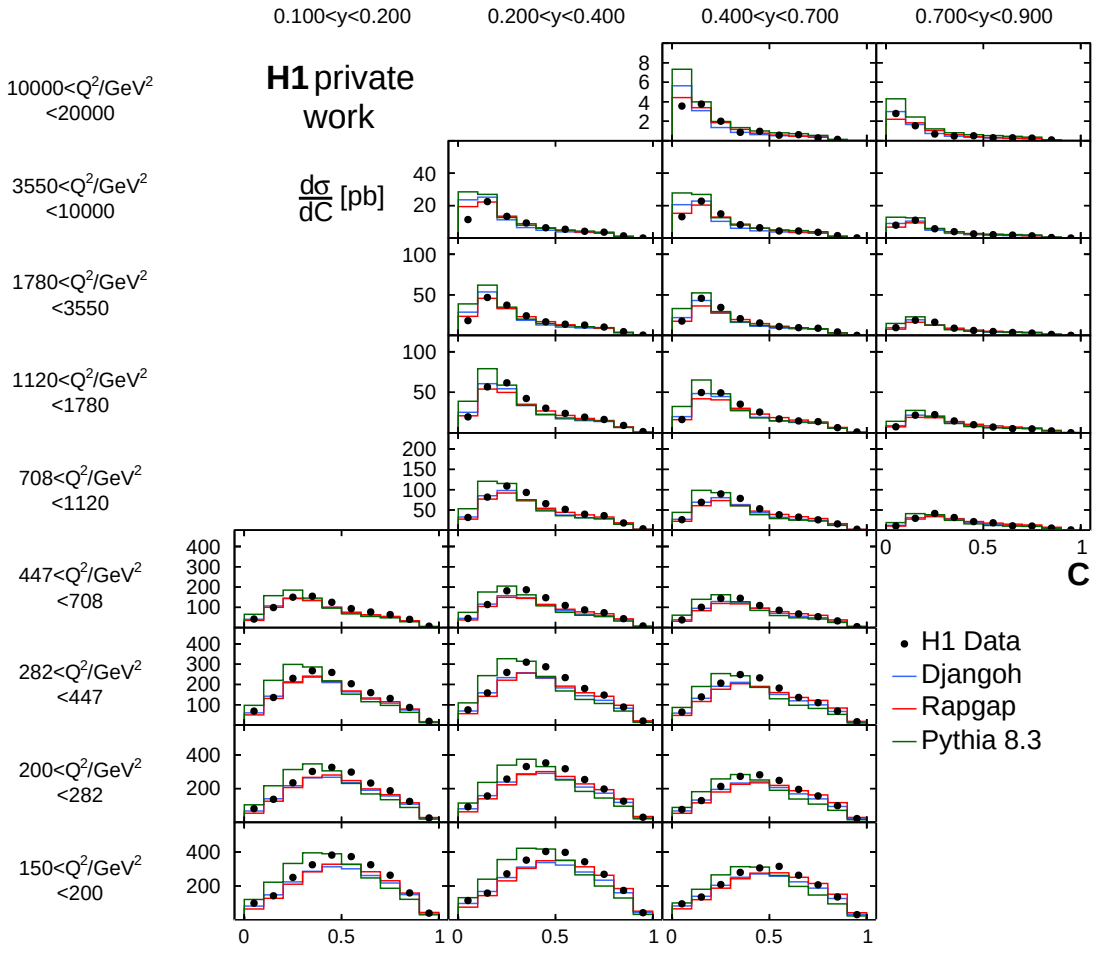


Figure B.7: Differential cross section $d\sigma/dC$ in bins of $Q^2$ and $y$. The $C$-parameter was defined in eq. (2.21). The data are compared to the Ragpag and Djangoh MC, as well as to Pythia 8.3 predictions.

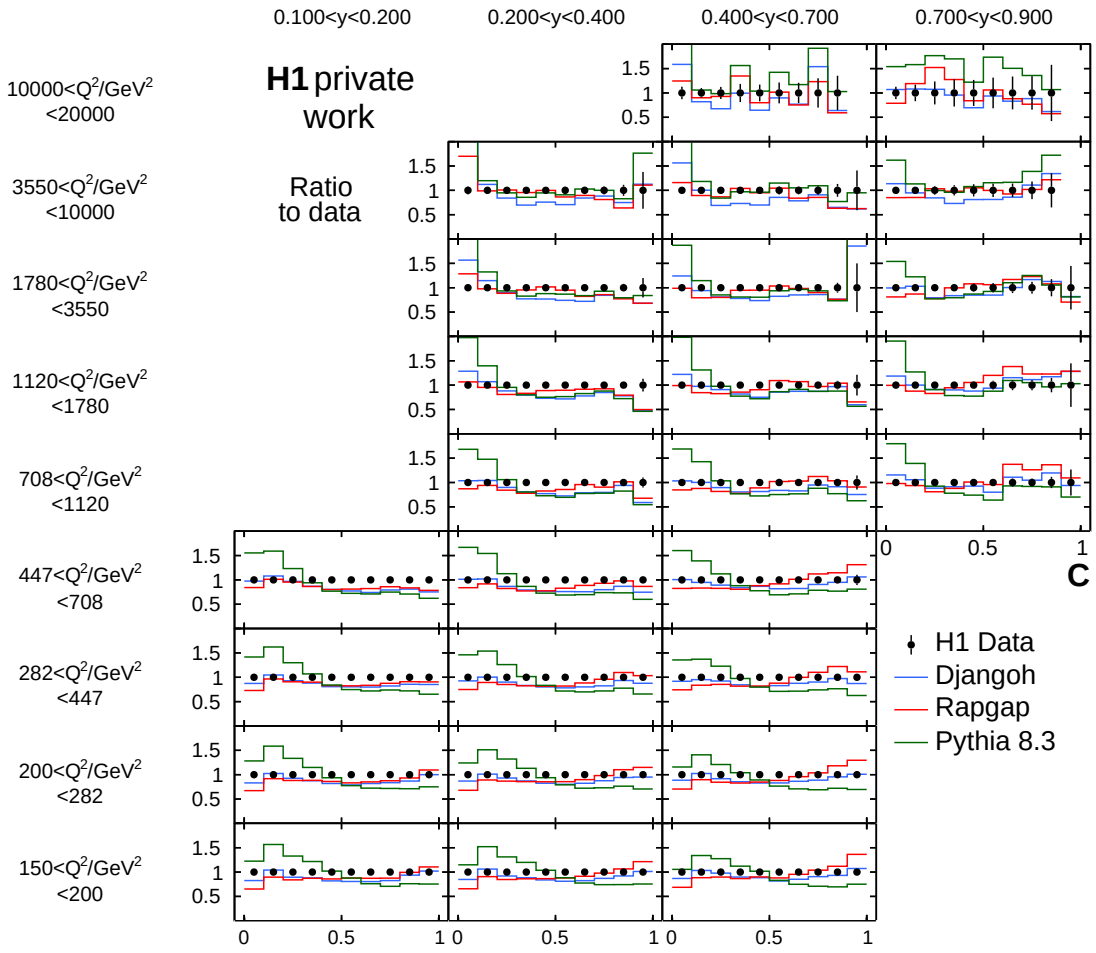


Figure B.8: Ratio of the MC models as in figure B.7 to the measured cross section.

# Bibliography


[1] J. Hessler, "Measurement of the 1-jettiness in deep-inelastic scattering at HERA,", arXiv:2111.11364.

[2] A. Accardi *et al.*, "Electron-Ion Collider: The next QCD frontier,", *The European Physical Journal A* 52 (2016) 268.

[3] P. Agostini *et al.*, "The Large Hadron-Electron Collider at the HL-LHC,", arXiv:2007.14491.

[4] LHeC Study Group Collaboration, J. L. Abelleira Fernandez *et al.*, "A Large Hadron Electron Collider at CERN: Report on the Physics and Design Concepts for Machine and Detector,", *J. Phys. G* 39 (2012) 075001, arXiv:1206.2913.

[5] D. P. Anderle *et al.*, "Electron-ion collider in China,", arXiv:2102.09222.

[6] D. J. Gross and F. Wilczek, "Ultraviolet behavior of non-abelian gauge theories,", *Phys. Rev. Lett.* 30 (Jun, 1973) 1343–1346.

[7] H. D. Politzer, "Reliable perturbative results for strong interactions?,", *Phys. Rev. Lett.* 30 (Jun, 1973) 1346–1349.

[8] M. Gell-Mann, "A schematic model of baryons and mesons,", *Physics Letters* 8 (1964) 214–215.

[9] H. Fritzsch, "Producing Heavy Quark Flavors in Hadronic Collisions: A Test of Quantum Chromodynamics,", *Phys. Lett. B* 67 (1977) 217–221.

[10] J. Campbell, J. Huston and F. Krauss, *The Black Book of Quantum Chromo Dynamics*, vol. 1. Oxford University Press, 2018.

[11] R. K. Ellis, W. J. Stirling and B. R. Webber, *QCD and Collider Physics*. Cambridge Monographs on Particle Physics, Nuclear Physics and Cosmology. Cambridge University Press, 1996.

[12] G. 't Hooft and M. Veltman, "Regularization and renormalization of gauge fields,", *Nuclear Physics B* 44 (1972) 189–213.

[13] W. E. Caswell, "Asymptotic behavior of non-abelian gauge theories to two-loop order,", *Phys. Rev. Lett.* 33 (Jul, 1974) 244–246.

[14] K. G. Wilson, "Confinement of quarks,", *Phys. Rev. D* 10 (Oct, 1974) 2445–2459.

[15] G. Sterman *et al.*, "Handbook of perturbative qcd,", *Rev. Mod. Phys.* 67 (1995) 157–248.

[16] A. Deur, S. J. Brodsky and G. F. de Téramond, "The QCD running coupling,", *Progress in Particle and Nuclear Physics* 90 (2016) 1–74. http://dx.doi.org/10.1016/j.ppnp.2016.04.003.

[17] H1 Collaboration, V. Andreev *et al.*, "Determination of the strong coupling constant $\alpha_s(m_Z)$ in next-to-next-to-leading order QCD using H1 jet cross section measurements,", *Eur. Phys. J. C* 77 (2017) 791, arXiv:1709.07251.

[18] J. Blümlein, "The theory of deeply inelastic scattering,", *Progress in Particle and Nuclear Physics* 69 (2013) 28–84.

[19] J. D. Bjorken, "Asymptotic sum rules at infinite momentum,", *Phys. Rev.* 179 (Mar, 1969) 1547–1553.

[20] G. Miller *et al.*, "Inelastic electron-proton scattering at large momentum transfers and the inelastic structure functions of the proton,", *Phys. Rev. D* 5 (1972) 528–544.

[21] Y. L. Dokshitzer, "Calculation of the Structure Functions for Deep Inelastic Scattering and $e^+e^-$ Annihilation by Perturbation Theory in Quantum Chromodynamics.,", *Sov. Phys. JETP* 46 (1977) 641–653.

[22] V. N. Gribov and L. N. Lipatov, "Deep inelastic *ep* scattering in perturbation theory,", *Sov. J. Nucl. Phys.* 15 (1972) 438–450.

[23] G. Altarelli and G. Parisi, "Asymptotic Freedom in Parton Language,", *Nucl. Phys. B* 126 (1977) 298–318.

[24] J. Collins, D. E. Soper and G. Sterman, "Factorization of Hard Processes in QCD,", *Adv.Ser.Direct.High Energy Phys* 5 (1988) 1–91, arXiv:hep-ph/0409313.

[25] G. Gustafson, "Dual description of a confined colour field,", *Physics Letters B* 175 (1986) 453–456.

[26] B. Andersson, G. Gustafson, G. Ingelman and T. Sjöstrand, "Parton Fragmentation and String Dynamics,", *Phys. Rept.* 97 (1983) 31–145.

[27] B. Webber, "A QCD model for jet fragmentation including soft gluon interference,", *Nuclear Physics B* 238 (1984) 492–528.

[28] D. Amati and G. Veneziano, "Preconfinement as a property of perturbative QCD,", *Phys. Lett. B* 83 (1979) 87–92. 13 p.

[29] K. H. Streng, T. F. Walsh and P. M. Zerwas, "Quark and Gluon Jets in the Breit Frame of Lepton - Nucleon Scattering,", *Z. Phys.* C2 (1979) 237.

[30] E. Farhi, "A QCD Test for Jets,", *Phys. Rev. Lett.* 39 (1977) 1587–1588.

[31] S. Kluth, "Tests of Quantum Chromo Dynamics at $e^+e^-$ Colliders,", *Rept. Prog. Phys.* 69 (2006) 1771–1846, arXiv:hep-ex/0603011.

[32] H1 Collaboration, C. Adloff *et al.*, "Measurement of event shape variables in deep inelastic *ep* scattering,", *Phys. Lett. B* 406 (1997) 256–270, arXiv:hep-ex/9706002.

[33] H1 Collaboration, C. Adloff *et al.*, "Investigation of power corrections to event shape variables measured in deep inelastic scattering,", *Eur. Phys. J. C* 14 (2000) 255–269, arXiv:hep-ex/9912052. [Erratum: Eur.Phys.J.C 18, 417–419 (2000)].

[34] H1 Collaboration, A. Aktas *et al.*, "Measurement of event shape variables in deep-inelastic scattering at HERA,", *Eur. Phys. J. C* 46 (2006) 343–356, arXiv:hep-ex/0512014.

[35] ZEUS Collaboration, S. Chekanov *et al.*, "Measurement of event shapes in deep inelastic scattering at HERA,", *Eur. Phys. J. C* 27 (2003) 531–545, arXiv:hep-ex/0211040.

[36] ZEUS Collaboration, S. Chekanov *et al.*, "Event shapes in deep inelastic scattering at HERA,", *Nucl. Phys. B* 767 (2007) 1–28, arXiv:hep-ex/0604032.

[37] D. Kang, C. Lee and I. W. Stewart, "Using 1-Jettiness to Measure 2 Jets in DIS 3 Ways,", *Phys. Rev.* D88 (2013) 054004, arXiv:1303.6952.

[38] V. Antonelli, M. Dasgupta and G. P. Salam, "Resummation of thrust distributions in DIS,", *JHEP* 02 (2000) 001, arXiv:hep-ph/9912488.

[39] D. Kang, C. Lee and I. W. Stewart, "Analytic calculation of 1-jettiness in DIS at $\mathcal{O}(\alpha_s)$,", *JHEP* 11 (2014) 132, arXiv:1407.6706.

[40] Z.-B. Kang, X. Liu and S. Mantry, "1-jettiness DIS event shape: NNLL+NLO results,", *Physical Review D* 90 (2014) 014041, arXiv:1312.0301.

[41] D. Kang, C. Lee and I. W. Stewart, "DIS Event Shape at N3LL,", *PoS* DIS2015 (2016) 142.

[42] T. Sjöstrand, S. Ask, J. R. Christiansen, R. Corke, N. Desai, P. Ilten, S. Mrenna, S. Prestel, C. O. Rasmussen and P. Z. Skands, "An introduction to PYTHIA 8.2,", *Comput. Phys. Commun.* 191 (2015) 159–177, arXiv:1410.3012.

[43] The Pythia authors, "Pythia 8.3 documentation," 2021. https://pythia.org. [accessed 21-11-12].

[44] W. T. Giele, D. A. Kosower and P. Z. Skands, "A simple shower and matching algorithm,", *Phys. Rev. D* 78 (2008) 014026, arXiv:0707.3652.

[45] W. T. Giele, D. A. Kosower and P. Z. Skands, "Higher-Order Corrections to Timelike Jets,", *Phys. Rev. D* 84 (2011) 054003, arXiv:1102.2126.

[46] W. T. Giele, L. Hartgring, D. A. Kosower, E. Laenen, A. J. Larkoski, J. J. Lopez-Villarejo, M. Ritzmann and P. Skands, "The Vincia Parton Shower,", *PoS* DIS2013 (2013) 165, arXiv:1307.1060.

[47] N. Fischer, S. Prestel, M. Ritzmann and P. Skands, "Vincia for Hadron Colliders,", *Eur. Phys. J.* C76 (2016) 589, arXiv:1605.06142.

[48] K. Charchula, G. A. Schuler and H. Spiesberger, "Combined QED and QCD radiative effects in deep inelastic lepton - proton scattering: The Monte Carlo generator DJANGO6,", *Comput. Phys. Commun.* 81 (1994) 381–402.

[49] H. Jung, "Hard diffractive scattering in high-energy *ep* collisions and the Monte Carlo generator RAPGAP,", *Comput. Phys. Commun.* 86 (1995) 147–161.

[50] ALEPH Collaboration, R. Barate *et al.*, "Studies of quantum chromodynamics with the ALEPH detector,", *Phys. Rept.* 294 (1998) 1–165.

[51] J. Pumplin, D. R. Stump, J. Huston, H. L. Lai, P. M. Nadolsky and W. K. Tung, "New generation of parton distributions with uncertainties from global QCD analysis,", *JHEP* 07 (2002) 012, arXiv:hep-ph/0201195.

[52] S. Höche and S. Prestel, "The midpoint between dipole and parton showers,", *Eur. Phys. J. C* 75 (2015) 461, arXiv:1506.05057.

[53] S. Höche and S. Prestel, "Triple collinear emissions in parton showers,", *Phys. Rev. D* 96 (2017) 074017, arXiv:1705.00742.

[54] S. Höche, F. Krauss and S. Prestel, "Implementing NLO DGLAP evolution in Parton Showers,", *JHEP* 10 (2017) 093, arXiv:1705.00982.

[55] NNPDF Collaboration, R. D. Ball *et al.*, "Parton distributions from high-precision collider data,", *Eur. Phys. J. C* 77 (2017) 663, arXiv:1706.00428.

[56] J. Bellm *et al.*, "Herwig 7.0/Herwig++ 3.0 release note,", *Eur. Phys. J. C* 76 (2016) 196, arXiv:1512.01178.

[57] C. Bierlich *et al.*, "Robust Independent Validation of Experiment and Theory: Rivet version 3,", *SciPost Phys.* 8 (2020) 026, arXiv:1912.05451.

[58] A. Gehrmann-De Ridder, T. Gehrmann, E. W. N. Glover, A. Huss and T. A. Morgan, "The NNLO QCD corrections to Z boson production at large transverse momentum,", *JHEP* 07 (2016) 133, arXiv:1605.04295.

[59] J. Currie, T. Gehrmann, A. Huss and J. Niehues, "NNLO QCD corrections to jet production in deep inelastic scattering,", *JHEP* 07 (2017) 018, arXiv:1703.05977. [Erratum: JHEP 12, 042 (2020)].

[60] J. Currie, T. Gehrmann and J. Niehues, "Precise QCD predictions for the production of dijet final states in deep inelastic scattering,", *Phys. Rev. Lett.* 117 (2016) 042001, arXiv:1606.03991.

[61] T. Gehrmann, A. Huss, J. Mo and J. Niehues, "Second-order QCD corrections to event shape distributions in deep inelastic scattering,", *Eur. Phys. J. C* 79 (2019) 1022, arXiv:1909.02760.

[62] D. Hoffmann, "HERA drawings," 2002. https://www-h1.desy.de/idet/idrawings/HERA/.

[63] Patrignani, C. et al. (Particle Data Group), "Review of Particle Physics,", *Chin. Phys.* C40 (2016) 100001.

[64] H1 Collaboration, F. D. Aaron *et al.*, "Determination of the Integrated Luminosity at HERA using Elastic QED Compton Events,", *Eur. Phys. J. C* 72 (2012) 2163, arXiv:1205.2448. [Erratum: Eur.Phys.J.C 74, 2733 (2012)].

[65] H1 Collaboration, "List of luminosity summary tables." H1 internal website, 2013. https://www-h1.desy.de/h1/www/h1det/lumi/summary_tables/.

[66] H1 Collaboration, I. Abt *et al.*, "The H1 detector at HERA,", *Nucl. Instrum. Meth.* A386 (1997) 310–347.

[67] H1 Collaboration, I. Abt *et al.*, "The Tracking, calorimeter and muon detectors of the H1 experiment at HERA,", *Nucl. Instrum. Meth.* A386 (1997) 348–396.

[68] R. Brun *et al.*, "GEANT3,", . CERN-DD-EE-84-1, 1987.

[69] D. Pitzl *et al.*, "The H1 silicon vertex detector,", *Nucl. Instrum. Meth. A* 454 (2000) 334–349, arXiv:hep-ex/0002044.

[70] B. List, "The h1 central silicon tracker,", *Nucl. Instrum. and Meth. A* 501 (2003) 49–53.

[71] H. Henschel and R. Lahman, "The backward silicon tracker of the H1 Experiment at HERA,", *Nucl. Instrum. and Meth. A* 453 (2000) 93–97.

[72] I. Glushkov, *D* Meson Production in Deep Inelastic Electron-Proton Scattering with the Forward and Backward Silicon Trackers of the H1 Experiment at HERA*. PhD thesis, Humboldt University at Berlin, 2007.

[73] [H1 Calorimeter Group] B. Andrieu et al., "Results from pion calibration runs for the H1 liquid argon calorimeter and comparisons with simulations,", *Nuc. Instrum. Meth. A* 336 (1993) 499–509.

[74] L. Goerlich and H. Wellisch, "Documentation of the LAr Clustering," 1991. H1 internal note, H1-12/91-204.

[75] H. Wellisch, J. Kubenka, H. Oberlack and P. Schacht, "Hadronic calibration of the H1 LAr calorimeter using software weighting techniques," 1994. H1 internal note, H1-02/94-346.

[76] C. Kiesling, B. B. Denby, J. Fent, G. Grindhammer and W. Haberer, "The H1 neural network trigger project," in *AIP Conf. Proc.*, vol. 583, p. 36–44. 2001.

[77] J. Naumann *et al.*, "A fast high-resolution track trigger for the H1 experiment,", *IEEE Transactions on Nuclear Science* 48 (2001) 1276–1281.

[78] A. Schöning, "The Fast Track Trigger at the H1 experiment design concepts and algorithms,", *Nucl. Instrum. Meth. A* 566 (2006) 130–132.

[79] H1 Collaboration, V. Andreev *et al.*, "Measurement of multijet production in $ep$ collisions at high $Q^2$ and determination of the strong coupling $\alpha_s$,", *Eur. Phys. J.* C75 (2015) 65, arXiv:1406.4709.

[80] T. Sjöstrand, "High-energy physics event generation with PYTHIA 5.7 and JETSET 7.4,", *Comput. Phys. Commun.* 82 (1994) 74–90.

[81] T. Sjöstrand, "PYTHIA 5.7 and JETSET 7.4: Physics and manual,", arXiv:hep-ph/9508391.

[82] A. Kwiatkowski, H. Spiesberger and H. J. Mohring, "Characteristics of radiative events in deep inelastic $ep$ scattering at HERA,", *Z. Phys. C* 50 (1991) 165–178.

[83] A. Kwiatkowski, H. Spiesberger and H. J. Mohring, "Heracles: An Event Generator for *ep* Interactions at HERA Energies Including Radiative Processes: Version 1.0,", *Comput. Phys. Commun.* 69 (1992) 155–172.

[84] G. Ingelman, A. Edin and J. Rathsman, "LEPTO 6.5 - A Monte Carlo Generator for Deep Inelastic Lepton-Nucleon Scattering,", *Comput.Phys.Commun. 101 (1997) 108-134* (1997) 108–134, arXiv:hep-ph/9605286.

[85] L. Lonnblad, "ARIADNE version 4: A Program for simulation of QCD cascades implementing the color dipole model,", *Comput. Phys. Commun.* 71 (1992) 15–31.

[86] T. Sjöstrand, L. Lönnblad and S. Mrenna, "PYTHIA 6.2: Physics and manual,", arXiv:hep-ph/0108264.

[87] T. Sjöstrand, S. Mrenna and P. Z. Skands, "PYTHIA 6.4 Physics and Manual,", *JHEP* 05 (2006) 026, arXiv:hep-ph/0603175.

[88] A. Courau and P. Kessler, "QED Compton scattering in high-energy electron - proton collisions,", *Phys. Rev.* D46 (1992) 117–124.

[89] A. Courau, S. Kermiche, T. Carli and P. Kessler, "Quasireal QED Compton Monte Carlo for HERA," in *Workshop on Physics at HERA*. 1991.

[90] T. Abe, "GRAPE dilepton (Version1.1): A Generator for dilepton production in *ep* collisions,", *Comput. Phys. Commun.* 136 (2001) 126–147, arXiv:hep-ph/0012029.

[91] J. Meyer, "Guide for the H1 simulation program H1Sim," 1989. https://www-h1.desy.de/ipublications/inotes1/sw003.txt.

[92] H. Fesefeldt, "The Simulation of Hadronic Showers: Physics and Applications,", . PITHA-85-02, 1985.

[93] G. Grindhammer and S. Peters, "The Parameterized simulation of electromagnetic showers in homogeneous and sampling calorimeters,", *Conf. Proc. C930222* (1993) 294–337, arXiv:hep-ex/0001020.

[94] A. Glazov, N. Raicevic and A. Zhokin, "Fast simulation of showers in the H1 calorimeter,", *Comput. Phys. Commun.* 181 (2010) 1008–1012.

[95] H1 Collaboration, J. Gayler, "Simulation of H1 calorimeter test data with GHEISHA and FLUKA," in *Workshop on Detector and Event Simulation in High-energy Physics (MC '91)*, pp. 312–326. 1991.

[96] M. Steder, "H1OO: A centralised analysis framework for the H1 experiment," in *18th Int. Conf. on Computing in High Energy and Nuclear Physics (CHEP 2010)*. 2010.

[97] "Data Preservation in High Energy Physics, DPHEP." https://dphep.org/. [accessed 2021-11-12].

[98] H1 Collaboration, D. M. South and M. Steder, "The H1 Data Preservation Project,", *J. Phys. Conf. Ser.* 396 (2012) 062019, arXiv:1206.5200.

[99] H1 Collaboration, D. Britzger, S. Levonian, S. Schmitt and D. South, "Preservation through modernisation: The software of the H1 experiment at HERA,", *EPJ Web Conf.* 251 (2021) 03004, arXiv:2106.11058.

[100] Akopov, Z. et al. (DPHEP Study Group), "Status Report of the DPHEP Study Group: Towards a Global Effort for Sustainable Data Preservation in High Energy Physics,", arXiv:1205.4667.

[101] ROOT Team 2021, "ROOT: analyzing petabytes of data, scientifically." https://root.cern/. [accessed 21-11-12].

[102] "DESY Bitbucket repository." https://stash.desy.de/. [accessed 2021-11-12].

[103] M. Arratia, D. Britzger, O. Long and B. Nachman, "Reconstructing the Kinematics of Deep Inelastic Scattering with Deep Learning,", arXiv:2110.05505.

[104] U. Bassler and G. Bernardi, "On the kinematic reconstruction of deep inelastic scattering at HERA: The Sigma method,", *Nucl. Instrum. Meth.* A361 (1995) 197–208, arXiv:hep-ex/9412004.

[105] U. Bassler and G. Bernardi, "Structure function measurements and kinematic reconstruction at HERA,", *Nucl. Instrum. Meth.* A426 (1999) 583–598, arXiv:hep-ex/9801017.

[106] H1 Collaboration, C. Adloff *et al.*, "Measurement and QCD analysis of neutral and charged current cross-sections at HERA,", *Eur. Phys. J.* C30 (2003) 1, arXiv:hep-ex/0304003.

[107] H1 Collaboration, F. D. Aaron *et al.*, "Inclusive Deep Inelastic Scattering at High $Q^2$ with Longitudinally Polarised Lepton Beams at HERA,", *JHEP* 1209 (2012) 061, arXiv:1206.7007.

[108] R. Kogler, *Measurement of jet production in deep-inelastic ep scattering at HERA*. PhD thesis, Hamburg U., 2011.

[109] S. Shushkevich, *Measurement of the Neutral Current Reaction at high $Q^2$ in the H1 Experiment at HERA II*. PhD thesis, Ludwig-Maximilian Univertität, 2012.

[110] M. Peez, *Search for deviations from the standard model in high transverse energy processes at the electron proton collider HERA. (Thesis, Univ. Lyon)*. PhD thesis, Université Claude Bernard, 2003.

[111] S. Hellwig, "Untersuchung der $D^*$ - $\pi$ slow Double Tagging Methode in Charmanalysen.". Diplomarbeit, Hamburg U., 2004.

[112] B. Portheault, *First measurement of charged and neutral current cross sections with the polarized positron beam at HERA II and QCD-electroweak analyses*. PhD thesis, Univ. Paris XI, 2005.

[113] H1 SPACAL Group Collaboration, R. D. Appuhn *et al.*, "The H1 lead / scintillating fiber calorimeter,", *Nucl. Instrum. Meth.* A386 (1997) 397–408.

[114] H1 Collaboration, V. Andreev *et al.*, "Measurement of Jet Production Cross Sections in Deep-inelastic ep Scattering at HERA,", *Eur. Phys. J. C* 77 (2017) 215, arXiv:1611.03421.

[115] G. Cowan, *Statistical data analysis*. Oxford Univ. Press, Oxford, 1998.

[116] G. Cowan, "A survey of unfolding methods for particle physics,", *Conf. Proc. C* 0203181 (2002) 248–257.

[117] H1 Collaboration, F. D. Aaron *et al.*, "Inclusive Deep Inelastic Scattering at High $Q^2$ with Longitudinally Polarised Lepton Beams at HERA,", *JHEP* 09 (2012) 061, arXiv:1206.7007.

[118] T. Kluge, *Measurement and QCD Analysis of Event Shape Variables in Deep-Inleastic Electron-Proton Collisions at HERA*. PhD thesis, RWTH Aachen, 2004.

[119] T. Gehrmann *et al.*, "Jet cross sections and transverse momentum distributions with NNLOJET,", *PoS* RADCOR2017 (2018) 074, arXiv:1801.06415.

[120] S. Schmitt, "TUnfold: an algorithm for correcting migration effects in high energy physics,", *JINST* 7 (2012) T10003, arXiv:1205.6201.

[121] A. Glazov, "Machine learning as an instrument for data unfolding,", arXiv:1712.01814.

[122] A. Andreassen, P. T. Komiske, E. M. Metodiev, B. Nachman and J. Thaler, "OmniFold: A Method to Simultaneously Unfold All Observables,", *Phys. Rev. Lett.* 124 (2020) 182001, arXiv:1911.09107.

# Acknowledgments

At the end of my thesis, I would like to take the opportunity to thank the people that have helped, motivated and supported me during the last year.
I am grateful to Stefan Kluth, Daniel Britzger and Andrii Verbytskyi for making this thesis possible with their guidance during the last year. I am especially grateful to Daniel, for supporting and mentoring me in my work even when meeting in person was not possible.
I would like to thank the H1 Collaboration for the opportunity to present the progress of my work on a regular basis. Thanks to your helpful comments and suggestions I had the chance to get the analysis to a preliminary state and even present the results outside of the collaboration. Thank you Daniel and Sook Hyun Lee for all your contributions in preparing the preliminary results. I would also like to thank Henry Klest and Peter Jacobs for the fruitful discussions on event shape observables, groomed or ungroomed.
Last but not least, I would like to thank my family for supporting me during my studies in all aspects.